SYNTHESIS, CHARACTERIZATION AND FUNCTIONALIZATION OF VERTICALLY ALIGNED CARBON NANOTUBE ARRAYS

A DISSERTATION SUBMITTED TO
THE MATERIALS SCIENCE AND NANOTECHNOLOGY
PROGRAM OF THE GRADUATE SCHOOL OF ENGINEERING
AND SCIENCE
OF BILKENT UNIVERSITY
IN PARTIAL FULFILLMENT OF THE REQUIREMENTS
FOR THE DEGREE OF
DOCTOR OF PHILOSOPHY

By

Gökçe Küçükayan Doğu

December 2012

I certify that I have read this thesis and that in my opinion it is fully adequate, in scope and in quality, as a thesis for the degree of Doctor of Philosophy.

Assist. Prof. Dr. Erman Bengü (Advisor)

I certify that I have read this thesis and that in my opinion it is fully adequate, in scope and in quality, as a thesis for the degree of Doctor of Philosophy.

Prof. Dr. Oğuz Gülseren

I certify that I have read this thesis and that in my opinion it is fully adequate, in scope and in quality, as a thesis for the degree of Doctor of Philosophy.

Assoc. Prof. Dr. Dönüş Tuncel

I certify that I have read this thesis and that in my opinion it is fully adequate, in scope and in quality, as a thesis for the degree of Doctor of Philosophy.

Assoc. Prof. Dr. Hilmi Volkan Demir

I certify that I have read this thesis and that in my opinion it is fully adequate, in scope and in quality, as a thesis for the degree of Doctor of Philosophy.

Assist. Prof. Dr. Göknur Cambaz Büke

Approved for the Graduate School of Engineering and Science:

Prof. Dr. Levent Onural

Director of the Graduate School

ABSTRACT

Synthesis, Characterization and Functionalization of Vertically Aligned Carbon Nanotube Arrays

Gökçe Küçükayan Doğu
Ph.D. in Materials Science and Nanotechnology Graduate Program
Advisor: Assist. Prof. Dr. Erman Bengü
December, 2012

In the last decade, there has been an increased interest on carbon nanotubes (CNTs) for various applications due to their unique structural, electronic, mechanical and chemical properties. Synthesis of CNTs is no more a challenge with the enhancements and diversity in production techniques. The remaining challenges regarding CNTs for high-volume manufacturing and commercial applications are related to the followings; firstly, gaining control over orientation and density of CNTs during growth for building two and/or three dimensional functional structures and secondly, modulating properties of these structures through a facile route. With regards to these challenges, the growth dynamics of vertically aligned carbon nanotubes (VA-CNTs) were investigated in this thesis. The first part of this thesis explains synthesis of VA-CNTs achieved through the use of a newly designed alcohol catalyzed chemical vapor deposition system in detail. Various catalyst layers were used in the experiments for understanding growth mechanism and thereby the effect of synthesis parameters. The catalyst layers were deposited on SiO_2 wafers through physical vapor deposition techniques. The configuration of these catalyst layers were engineered to tune the density and alignment of VA-CNTs by considering the competing mechanism between the subsurface diffusion and migration of catalyst particles. In addition, the annealing parameters were investigated for synthesizing taller and aligned CNTs. The characterization of catalyst layers and VA-CNTs were performed using analysis of Scanning Electron Microscopy, Raman Spectroscopy, Atomic Force Microscopy, X-ray Photoelectron Spectroscopy, Electron Energy Loss Spectroscopy, High Resolution Transmission Electron Microscopy and Raman Spectroscopy.

In the second part, effect of synthesis parameters such as growth temperature and pressure, carbon source type and concentration were examined to better understand the growth dynamics of VA-CNTs. Physical and structural transitions of CNTs were observed induced by the decomposition reaction processes of various carbon sources at a related growth temperature. Growth behavior of VA-CNTs was investigated under different carbon source concentration and pressure to find an optimum growth range.

The results indicated that while the synthesis method followed in this work is a catalytic based process where the reaction kinetics has a profound influence on the growth of VA-CNTs molecular diffusion mechanisms were found to be playing a key role in determining the growth, size, orientation and structural properties of VA-CNTs. Hence, an approach incorporating the kinetic and diffusion related processes were followed for building an empirical model for uncovering the dominant mechanisms responsible for the termination of growth of VA-CNTs.

In the following sections of the thesis, the preliminary studies regarding Li intercalation to VA-CNTs and cell growth on CNTs were performed for possible future applications of two and three-dimensional structures based on CNTs. *In situ* Li intercalation was studied during the growth of VA-CNTs which does not require post processing for the intercalation mechanism as commonly performed in the existing literature. Li intercalation in the CNTs was confirmed by using X-ray Photoelectron Spectroscopy, Electron Energy Loss Spectroscopy and Raman Spectroscopy following the changes induced by the charge transfer from Li to the carbon lattice.

In the second application case, used of VA-CNTs were examined as a scaffold for growing mesenchymal stem cells (MSCs). Surfaces covered with VA-CNTs were patterned by using elasto-capillary mechanism to create suitable ‘nests’ for MSCs to be anchored. The cell viability test was conducted on seeded MSCs on

CNT nests and indicated no toxic effect of CNT nests when they were used as scaffold. Furthermore, an aging effect of cells on adhesion was investigated.

As a conclusion, the work presented here demonstrated that control over structural and surface properties of VA-CNTs could be attained by taking advantage of a wide range of growth parameters such as temperature, pressure and carbon source type. Hence, the two case studies examined in this study demonstrated a path for aligned and denser CNTs synthesized with desired properties using the learnings attained in the first part of the thesis to be used as anode materials for Li ion batteries and as alternative scaffolds for tissue engineering applications.

Keywords: vertically aligned carbon nanotubes, lithium intercalation, scaffold, chemical vapor deposition, physical vapor deposition, growth mechanism, application

ÖZ

Dik Olarak Hizalanmış Karbon Nanotüplerin Sentezlenmesi, Karakterizasyonu ve İşlevselleştirilmesi

Gökçe Küçükayan Doğu
Ph.D. Malzeme Bilimi ve Nanoteknoloji Programı
Tez Yöneticisi: Yrd. Doç. Dr. Erman Bengü
Aralık, 2012

Son on yıllık süreçte, karbon nanotüplerin çeşitli uygulama alanlarındaki kullanımı üzerine olan ilgi nanotüplerin eşsiz yapısal, elektriksel, mekaniksel ve kimyasal özelliklerinden dolayı hızla artmıştır. Son zamanlarda çeşitlenen karbon nanotüp üretim metotlarıyla artık bu yapıları üretmek zor değildir. Önemli olan karbon nanotüplerin yüksek miktarda üretimini ve kitlesel uygulamalardaki kullanımını yaygınlaştırmaktır. Bunları gerçekleştirmek ise şunlara bağlıdır; fonksiyonel iki ve/veya üç boyutlu yapılar için yönlenmiş ve uygun yoğunlukta karbon nanotüp büyütülmesinde kontrol sağlanması ve yapısal özelliklerinin kolay bir şekilde değiştirilmesidir. Bu problemlerden yola çıkarak tezde, dik olarak hizalanmış karbon nanotüplerin (VA-CNT) büyüme dinamiği incelenmiştir. Tezin ilk kısmı VA-CNT' lerin yeni tasarlanan alkol katalizörlü kimyasal buhar kaplama tekniği ile sentezlenmesini açıklamaktadır. Büyüme mekanizmasını anlamak için yapılan deneylerde kullanılan katalizör tabakaları fiziksel buhar kaplama metodu ile kaplanmıştır. VA-CNT' lerin yoğunluklarının ve yönlenmesinin ayarlanması yüzey altı difüzyon ile katalizör parçacıklarının yüzeydeki göçü arasında rekabet eden mekanizmayı göz önüne alarak katalizör tabakalarının farklı şekilde düzenlenmesi ile sağlanmıştır. Ayrıca, katalizör tavlama parametreleri daha uzun ve daha iyi hizalanmış karbon nanotüpler üretmek için incelenmiştir. Katalizör tabakalarının ve karbon nanotüplerin karakterizasyonları taramalı Elektron Mikroskobu, Raman Spektroskopisi, Atomik Kuvvet Mikroskobu, X-ışını Fotoeletron Spektroskopisi, Elektron Enerjisi Kayıp Spektroskopisi, Yüksek Çözünürlüklü Geçirgenli Elektron Mikroskobu kullanılarak gerçekleştirilmiştir.

İkinci kısımda, VA-CNT' lerin büyüme mekanizmalarını daha iyi anlamak için sentez sıcaklığı, sentez basıncı, karbon kaynağı tipi ve konsantrasyonu gibi üretim parametrelerinin etkileri belirli değer aralıklarında incelenmiştir. İlgili sıcaklıkta karbon kaynaklarının bozulma tepkimelerinin etkisiyle karbon nanotüplerde fiziksel ve yapısal dönüşümler gözlenmiştir. Ayrıca, farklı konsantrasyonlarda ve basınçlarda kullanılan karbon kaynağı ile sentezlenen VA-CNT' lerin uzunlukları kullanılarak en verimli karbon nanotüp üretme aralığı bulunmuştur.

Tezde kullanılan sentez metodu reaksiyon kinetiğinin VA-CNT' lerin büyümesine etkisi olan katalitik temelli bir süreç olmasına rağmen moleküler difüzyon büyüme mekanizması da VA-CNT' lerin boyutlarında, yapılarında ve hizalanmalarında önemli bir rol oynamaktadır. Bundan ötürü, karbon nanotüplerin büyümesinin sonlanmasından sorumlu etkiyi bulmak için kullanılan yaklaşımdaki hesaplamalarda kinetik ve difüzyon temelli süreçler göz önüne alınmıştır.

Tezin takip eden bölümlerinde, karbon nanotüp temelli iki ve üç boyutlu yapıların olası uygulama alanı için lityumun (Li) karbon nanotüp yapısında araya ilave edilmesi ve karbon nanotüpler üzerinde hücre büyütülmesi üzerine ön çalışma yapılmıştır. Li' un karbon nanotüp yapısında araya ilave edilmesi literatürde yaygın bir biçimde büyüme basamağından sonra ek işlemler ile yapılırken, tezde Li' un yapıya ilave edilmesi karbon nanotüplerin büyümesiyle eş zamanlı olarak tek basamakta gerçekleştirilmiştir. Yapıya Li' un ilave edilmesi, X-ışını Fotoeletron Spektroskopisi, Elektron Enerjisi Kayıp Spektroskopisi ve Raman Spektroskopisi kullanılarak teyit edilmiştir.

İkinci uygulama alanında VA-CNT' ler mezenkimal kök hücrelerin büyütülmesinde yapı iskelesi olarak incelenmiştir. Karbon nanotüplerle kaplı yüzeyler "elasto-capillary" mekanizmasından faydalanarak hücrelerin tutunabileceği karbon nanotüp yuvaları oluşturmak için şekillendirilmişlerdir. Daha sonra hücrelerin yaşlanmasının yüzeylere yapışmaya olan etkisi

incelenmiştir. Ayrıca, hücre yaşayabilme testi karbon nanotüp yuvalarının üzerine ekilen hücrelerde gerçekleştirilmiş ve karbon nanotüplerin yapı iskelesi olarak kullanıldığında hücrelerde herhangi bir zehirlenme etkisi görülmemiştir.

Sonuç olarak tezde kullanılan sıcaklık, basınç ve karbon kaynağı gibi çeşitli sentez parametreleri ile VA-CNT' lerin yüzeysel ve yapısal özelliklerinin kontrol edilebileceği görülmüştür. Dolayısıyla, gerçekleştirilen iki ön çalışma yoğun ve hizalanmış karbon nanotüplerin Li iyon pillerinde anot malzemesi ve doku mühendisliği uygulamasında alternatif yapı iskelesi olarak kullanımı üzerine bir yol sunmaktadır.

Anahtar kelimeler: dik hizalanmış karbon nanotüpler, lityum katkılandırılması, yapı iskelesi, kimyasal buhar kaplama, fiziksel buhar kaplama, uygulama

Dedicated to my family and husband,

Acknowledgements

I would like to express my sincere gratitude to my supervisor, Dr. Erman Bengü, for all of his patience and endless support. He taught me how to conduct research and approach scientific problems during all these years. He also taught me how to write and talk about research. Apart from research, I have learned much from him. It has been a unique and inspiring experience.

My honest regards go to Dr. Oğuz Gülseren, Dr. Rasim Ovalı and Şener Şen from Physics Department for their theoretical calculations which lightened my studies. Without their calculations, it would not be possible to answer the challenges. I would also like to acknowledge Dr. Can Akçalı, Verda Bitirim and Damla Gözen from Molecular Biology and Genetics Department for their valuable collaboration throughout the stem cell study. Furthermore, many thanks go to Dr. Göknur Cambaz Büke for her advices and guidance in writing this dissertation.

I could never forget the assistance of my lab colleagues with whom I spent most of my time during Ph.D. Serim Ilday, Beril Baykal, Dr. Devrim Sam, Dr. Kuldeep Rana and Hüseyin Alagöz; thank you all for your golden discussions and aids. Special thanks go to Dr. Mustafa Fatih Genişel and Ethem Anber for helping me a lot during the construction of chemical vapor deposition system in Dr. Bengü's laboratory.

List of researchers outside Bilkent University helped me in this dissertation. I would like to express my thanks to Dr. Servet Turan and Dr. Hilmi Yurdakul for their collaboration in transmission electron microscope analysis at Anadolu University. I am also grateful to Dr. Raşit Turan and Dr. Mustafa Kulakçı for providing me an access to their electron beam evaporation equipment at Middle East Technical University.

I would like to acknowledge Department of Chemistry, Advanced Research Laboratory (ARL) and National Nanotechnology Research Center (UNAM) at Bilkent University for providing access to their facilities and clean rooms. I also want to thank to The Scientific and Technological Research Council of Turkey (TÜBİTAK) for granting me a graduate scholarship during my Ph.D. (2211-National Scholarship Programme for Ph.D. Students).

I would like to pay another special tribute to my mom, dad and brother for their never-ending love and encouragement. Their belief in me always brightened the way throughout my career. Last but not the least, I am thankful to my husband for being such a caring companion. His consistent support and motivation has meant everything to me. I could not image to complete this dissertation without their supports and I am feeling so lucky to have them.

Contents

Chapter 1. Introduction 1

1.1 Discovery of carbon nanotubes 1
1.2 Structure, properties and characterization of carbon nanotubes 3
1.3 Thesis objective 8

Chapter 2. Literature Review 10

2.1 Synthesis methods for carbon nanotubes 10
2.1.1 Chemical vapor deposition method 11
2.1.2 Laser ablation method 13
2.1.3 Arc discharge method 14
2.1.4 Pyrolysis 14
2.2 Growth mechanism of carbon nanotubes 15
2.3 Synthesis of vertically aligned carbon nanotubes 18
2.4 Vertically aligned carbon nanotubes as multi-functional surfaces 27
2.4.1 Anode material for lithium ion battery 27
2.4.2 Extracellular matrix for cells 30

Chapter 3. Materials and Method 32

3.1 Experimental procedure and equipment 32
3.1.1 Preparation of catalyst layers 34
3.1.1.1. Physical vapor deposition method 34
3.1.1.2. Wet chemistry method 37
3.1.2 Synthesis of vertically aligned carbon nanotubes 38
3.2 Characterization techniques 40
3.2.1 Raman spectroscopy 40
3.2.2 Atomic force microscopy 40
3.2.3 Scanning electron microscopy 41
3.2.4 Transmission electron microscopy 41
3.2.5 X-Ray photoelectron spectroscopy 42
3.2.6 Contact angle measurement 43

Chapter 4. Results and Discussion 44

- 4.1 Growth of vertically aligned carbon nanotubes 45
  - 4.1.1 Optimization of catalyst design 45
  - 4.1.2 Optimization of annealing step 60
  - 4.1.3 Effect of growth parameters 67
  - 4.1.4 Modeling for the growth of vertically aligned carbon nanotubes . 88
- 4.2 Functionalization of vertically aligned carbon nanotubes 99
  - 4.2.1 Lithium intercalation of vertically aligned carbon nanotubes 99
  - 4.2.2 Cell attachment on patterned carbon nanotubes 111

Chapter 5. Conclusions 122

Appendixes 127

Appendix I 128

Appendix II 130

Appendix III 131

Appendix IV 133

Appendix V 135

Appendix VI 136

Appendix VII 137

Bibliography 142

List of Publications 178

Copyright Licences 180

List of Figures

Figure 1. The number of publications regarding CNT by years. 1

Figure 2. CNTs and “carbon filaments” reported in the literature by various researchers at different years; (a) 1991, (b) 1952 and (c) 1984 (*1*, *2*, *4*)............. 2

Figure 3. Representative drawings for carbon allotropes; (a) graphene, (b) fullerene and (c) diamond. 3

Figure 4. Representative drawings for one end capped (a) SWCNT and (b) open ended MWCNT. 4

Figure 5. (a) High resolution TEM image of a MWCNT shows the side walls and the hollow core (*14*) while (b) STM image of a SWCNT indicates the atomic sequencing (*15*). 5

Figure 6. The nature of the G and D modes in Raman for graphite (*16*). 7

Figure 7. Schematic drawings for (a) CVD, (b) laser ablation and (c) discharge methods. 11

Figure 8. Schematic representation of processes occurring on the catalyst particle during the growth of a CNT. 16

Figure 9. Representative drawings show the (a) base and (b) tip growth models of CNT... 18

Figure 10. (a-c) The first reported VA-CNTs by Li *et al.* at 1996 (*73*). (d) By Hata *et al.*, the millimeter tall VA-CNTs synthesized using water assisted CVD are compared with a match for a size reference (*8*). 21

Figure 11. SEM images of the catalyst islands formed on (a) 0.5 nm and (b) 6 nm Al buffer layer (*86*). 25

Figure 12. SEM images of CNTs on Si substrates with TiN, TiO_2 and Al_2O_3 buffer layer (*92*). 26

Figure 13. Working principle of Li-ion battery showing the charge-discharge cycle 28

Figure 14. Schematic representation shows three steps for the synthesis of VA-CNTs; preparation of catalyst layers, annealing and growth. The annealing and growth steps are performed inside an ACCVD furnace.................................... 33

Figure 15. Photograph of (a) thermal and (b) e-beam (I) evaporation systems. 35

Figure 16. Drawings for the catalyst configurations used in the experiments. .. 35

Figure 17. Photograph of EBE-4 (II) system mounted with XPS...................... 36

Figure 18. Photograph and schematic drawing of the ACCVD experimental set up.. 38

Figure 19. SEM image of CNTs grown on (a) 1nm Fe/SiO_2 and (b) 1nm Fe/10 nm Al layers at temperature of 625 ^{0}C... 46

Figure 20. Side view SEM images showing the alignment of CNTs grown on (a) 1nm Fe/10nm Al and (b) 1nm Co/10nm Al catalyst layers. 48

Figure 21. Schematic representation showing the subsurface diffusion and coarsening of catalyst particles on the buffer layer of Al during a heat treatment. 50

Figure 22. Side view SEM images of VA-CNTs grown on (a) normal and (b) sandwich catalyst configurations. HRTEM images of CNTs grown on (c) normal and (d) sandwich catalyst configurations. (e) Raman spectra of VA-CNTs grown on both catalyst configurations.. 52

Figure 23. Top view SEM images of collapsed CNTs grown on (a) normal and (b) sandwich catalyst designs. 2D contact mode AFM images of (c) normal and (d) sandwich catalyst designs after reduction process. (e) Size distribution of particles on both catalyst designs after reduction process................................. 54

Figure 24. A representative drawing of a sandwich catalyst layer after the reduction process.. 56

Figure 25. SEM images of VA-CNTs synthesized at 625 °C using sandwich catalyst design on varying thickness of bottom Al layer (3, 5, 7 and 10 nm). AFM images of H_2-reduced catalyst layers at 625 °C and the plot for the change of VA-CNT length and average particle size distribution (*w*) versus bottom Al layer thickness... 58

Figure 26. (a) SEM and (b) HRTEM images of CNTs synthesized at 625 °C on the 0.5nm Al/1nm Fe/10nm Al catalyst configuration...................................... 60

Figure 27. (a-h) SEM images of VA-CNTs grown on the non-reduced and H_2-reduced sandwich catalyst layers at 625 °C for 5,10, 15, 20, 30 and 60 minutes, respectively. (h) The plot shows changes in the length of VA-CNTs by reduction time.. 62

Figure 28. Top view SEM images of (a) as-deposited and H_2-reduced at 625 °C for (b) 15 minutes and (c) 60 minutes sandwich catalyst layers....................... 63

Figure 29. (a-f) XPS spectra of Co 2p regions for various Co layers (● and *, respectively, indicate that Co layers are prepared using e-beam (I) and EBE-4 (II) evaporation systems).. 65

Figure 30. SEM images of VA-CNTs synthesized at 625 °C using ethanol, acetone and isopropanol as carbon sources. 68

Figure 31. (a) Raman spectra of VA-CNTs grown at 625 °C using acetone, ethanol and isopropanol as carbon sources. (b) The plot for I(G/D) and I(2D/G) ratios of VA-CNTs versus carbon sources. 70

Figure 32. SEM images of VA-CNTs synthesized at 750 °C using ethanol, acetone and isopropanol as a carbon source. 72

Figure 33. (a) Raman spectra of VA-CNTs grown at 750 °C using acetone, ethanol and isopropanol. (b) The plot for I(G/D) and I(2D/G) ratios of VA-CNTs versus carbon sources. 73

Figure 34. TEM images of VA-CNTs synthesized at temperatures of (a) 625 °C and (b) 750 °C using ethanol as carbon source. White arrows show the amorphous carbon presence on the side wall of a CNT. 75

Figure 35. CNT surfaces after the growth step at 625 °C using (a) benzene and (b) toluene as carbon sources. 77

Figure 36. Dynamic contact angle measurements of VA-CNTs synthesized using various carbon sources at temperatures of (a) 625 °C and (b) 750 °C. The volume of water droplet used for the measurements was 8 μL. 79

Figure 37. SEM images of VA-CNTs synthesized under pressures of 40, 56, 69, 81 and 94 Torr at 625 °C (pressure set). The plot of the VA-CNT length versus pressure 82

Figure 38. SEM images of VA-CNTs synthesized using various liquid ethanol temperatures (32, 50, 71, 81 °C) at 625 °C (concentration set). The plot of the

VA-CNT length versus pressure that obtained by varying liquid ethanol temperature. 86

Figure 39. Raman spectra of VA-CNTs synthesized at pressure of 40 and 94 Torr (black and red lines, respectively) with an inset of magnified D and G bands.......... 87

Figure 40. XPS spectra taken from the top surface of VA-CNTs. C 1s peak at 284.4 eV was attributed to the presence of CNTs while there was no signal for Co 2p indicating the root growth type. 91

Figure 41. Representative side view schematic of VA-CNTs showing the boundary conditions for the calculations. 92

Figure 42. The plot of the VA-CNT length versus growth time with representative SEM images of VA-CNTs grown at 625 °C.......... 94

Figure 43. An illustration for the arrangement of CNTs in a closed packed design on a substrate (Each circle represents a CNT). 96

Figure 44. Side view SEM images of grown VA-CNTs from the (a) non-Li (Set 3) and (b) Li containing (Set 1) catalyst layers. (c) S/TEM image of a CNT from Set 1 (*165*). 102

Figure 45. EEL spectra of Set 1 for (a) Li-*K* edge and (b) C-*K* edge (inset shows where the spectrum is taken from). (c) A comparison of Raman spectra for VA-CNTs from Set 1 (Li containing) and Set 3 (non-Li containing) (*165*). 104

Figure 46. Li 1s XPS spectra of (a) Set 4, (b) Set 2, (c) Set 3 and (d) Set 1. C 1s XPS spectra of (e) Set 3 and (f) Set 1 (*165*). 106

Figure 47. Li 1s XPS spectra of (a) Set 5 and (b) Set 6. (c) C 1s XPS spectra of Set 5 (*165*). 110

Figure 48. (a) SEM and (b) HRTEM images of VA-CNTs synthesized at 625 °C on the sandwich catalyst layers for the cell attachment experiments. (c) 2D AFM image from the top view of VA-CNTs with inset of top view SEM image. (d) Raman spectra of the synthesized VA-CNTs indicating the variety of MWCNTs as shown in RBM mode as inset (*194*). 113

Figure 49. Schematic representation of experimental approach (*194*). 114

Figure 50. 45° tilted SEM images of non-coated and collagen coated CNT surfaces with higher magnified SEM images showing the smoothing effect of collagen. 115

Figure 51. Attached MSCs from P0 passage on the (a) non-coated and (b) collagen coated CNT surfaces. (c) The plot of average areal density of MSCs from three subsequence passages. (-) indicates CNT surfaces without collagen while (+) means collagen coated CNT surfaces (*194*). 117

Figure 52. MTT assay plots showing the percent viability of MSCs from different passages on the (a) non-coated patterned CNTs and (b) collagen coated patterned CNTs (* indicates significant $p<0.05$.) (*194*). 120

Figure 53. XPS spectra of normal design and sandwich design catalyst layers before and after reduction at 625 °C (black line indicates the layers before the reduction whereas pink line represents the spectra of catalyst layers after the reduction). 129

Figure 54. The images after masking to calculate the compacted areas shown by black. 130

Figure 55. The proposed arrangement of CNTs on the substrate..................... 131

Figure 56. The expression of the markers for bone marrow derived MSCs and hematopoetic stem cells at (a) mRNA and (b) protein levels (*194*)................. 136

Figure 57. (a) Possible Li adsorption sites; top (1), hollow (2) and bridge (3) for 6x6 unit cell. (b) PDOS for Li intercalated cases shown in (c) and (d). Dotted line indicates the Fermi level. Top and side views of the optimized geometry and the charge density of (c) Li intercalated bilayer graphene and (d) similar system but starting from Li substitution to a C site on top layer (*165*)............ 138

List of Tables

Table 1. The properties of catalyst layers and VA-CNTs on normal and sandwich catalyst designs.. 56

Table 2. Tabulation of binding energies of Co 2p peaks for different catalyst configurations indicating the catalyst state before and after the reduction step. 67

Table 3. Summary of the values used in the experiment series of pressure and concentration. The bold values are for the pressure set while the rest is for the concentration set.. 84

Table 4. Summary of the experiments conducted for Li intercalation study. .. 101

Table 5. Binding energies and FWHM for C 1s and Li 1s XPS peaks. 107

Table 6. The atomic ratio of Co/Al calculated for the designs before and after reduction process.. 129

Table 7. Calculated values of the ethanol flow in the pressure set. 134

Table 8. Calculated values of the ethanol flow in the concentration set.......... 135

Table 9. Binding energies, Li-C bond distances, and total charge transfer from Li to C network for Li doped AA stacking bilayer resulted from LDA calculations (*165*). 141

GLOSSARY

ACCVD: Alcohol catalyzed chemical vapor deposition

AFM: Atomic force microscopy

CNT: Carbon nanotube

CVD: Chemical vapor deposition

D band mode: Disorder mode

DFT: Density functional theory

e-beam: Electron beam evaporation

ECM: Extracellular matrix

EELS: Electron energy loss spectroscopy

G band mode: Tangential mode

HRTEM: High resolution transmission electron microscopy

MSC: Mesenchymal stem cell

MWCNT: Multi-walled carbon nanotube

PVD: Physical vapor deposition

RAMAN: Raman spectroscopy

RBM: Radial breathing mode

SEI: Solid electrolyte interphase

SEM: Scanning electron microscopy

STM: Scanning tunneling microscope

S/TEM: Scanning transmission electron microscopy

SWCNT: Single-walled carbon nanotube

TEM: Transmission electron microscopy

VA-CNT: Vertically aligned carbon nanotube

XPS: X-ray photoelectron spectroscopy

a: diameter of a carbon source molecule

C_0: Initial concentration of carbon source

C^*: Effective carbon source concentration at the root

d: Diameter of CNT

D_c: Mass diffusion coefficient

D_e: Efficient diffusion coefficient of a gas molecule

D_k: Knudsen diffusion coefficient

D_m: Molecular diffusion coefficient

F: Filling fraction

h: Average height of particles

J: Net diffusion flux

k_s: Overall reaction rate constant

L: Total length of VA-CNTs

m: Reaction rate order

N_A: Avagodro’s number

R: Gas constant

r: Reaction rate of carbon source

T: Process temperature

t: Process time

w: Average particle size distribution

w_L: Wave numbers (cm^{-1})

ρ: Areal density of CNTs

δ: Theoretical Van der Waals tube distance (0.34 nm)

λ: mean free path

γ: Growth rate of CNTs

β: Porosity value of arrays

ε: Tortuosity of diffusion channels

x: Distance between two adjacent CNTs (pore size)

Chapter 1

Introduction

1.1 Discovery of carbon nanotubes

Over the last decade, carbon nanotubes (CNTs) have been a popular subject for intense scientific and technological investigations owing to their unique properties. Many applications for CNTs have been proposed ranging from biomedical fields to electronic devices for the next generation computers. Although, application of CNTs to a commercial product has not yet to be finalized, the frenzy over the CNTs continues almost unabated as shown in Figure 1.

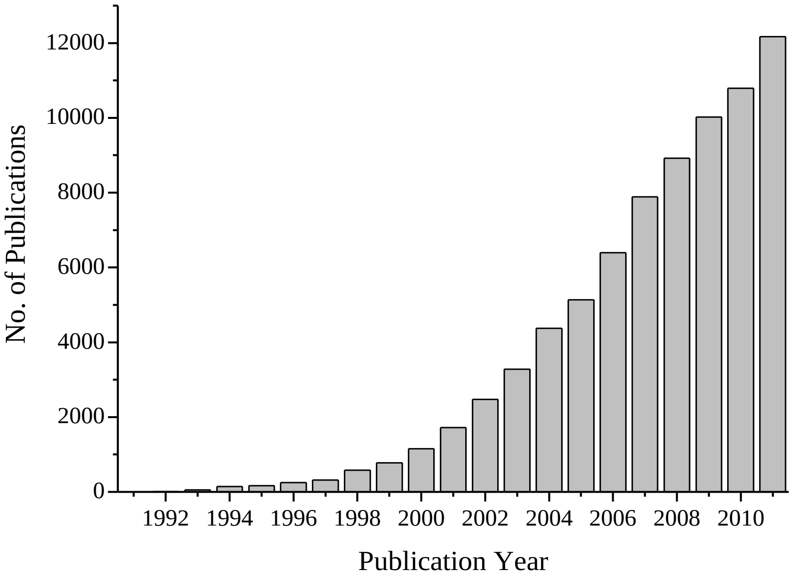

Figure 1. The number of publications regarding CNT by years.

It is widely recognized that Iijima in 1991 has reported the first observation of CNTs (*1*). However, there have been earlier reports displaying TEM images of hollow carbonaceous structures which can be easily recognized as CNTs (*2–4*). The 1991 report by Iijima was actually the first one to accurately describe the atomic scale details of these structures and proposing that these were “nanotubes”(*1*). Nevertheless, the study by two Soviet scientists in 1952 merit recognition in this regard (*2*). Radushkevich and Lukyanovich had observed similar structures in 1952 but due to the limited resolution of electron microscopy in those years, they called their observations as “carbon filaments” (*2*). Similarly, in 1984, Tibbetts reported similar hollow tubular structures as “filaments” (*4*). Figure 2 shows the most known CNT and “carbon filaments” early reported in the literature.

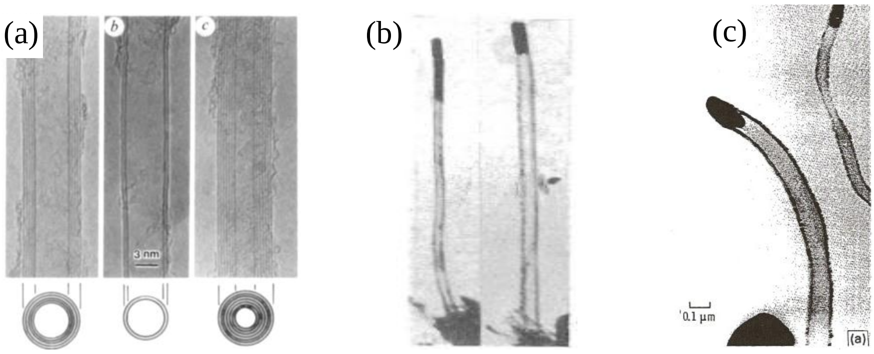

Figure 2. CNTs and “carbon filaments” reported in the literature by various researchers at different years; (a) 1991, (b) 1952 and (c) 1984 (*1*, *2*, *4*).

Still in the light of these earlier reports what now appears to be CNTs, the work by Iijima cannot be dismissed, as only Iijima attempted to explain the atomic structure of his observations through single-sheets of graphite and naming his observations as CNTs (*1*). Furthermore, CNTs continue inspiring further researches on this field.

1.2 *Structure, properties and characterization of carbon nanotubes*

Carbon is the sixth element of the periodic table and has the ability of hybridization in various forms such as sp (acetylene), sp^2 (ethylene) and sp^3 (methane). Carbon is one of the few elements to display orbital hybridization which as a result allows for many carbon allotropes to exist. The best known allotropes of carbon are diamond (*5*), fullerenes (*6*) and graphite (*7*) as shown in Figure 3. Extended flat sheets made up of carbon atoms in honeycomb patterns form graphene layers where carbon atoms are hybridized in the sp^2 form.

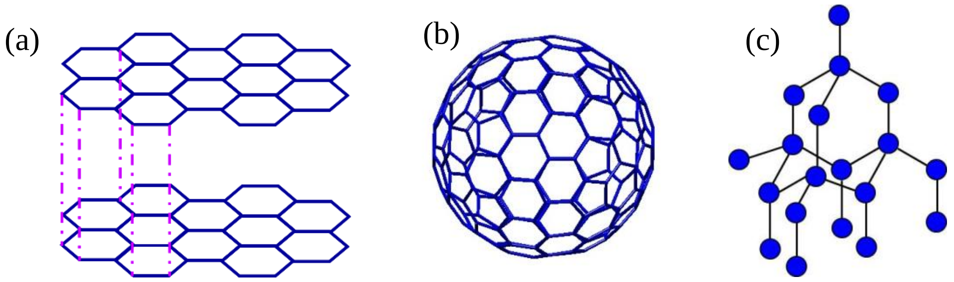

Figure 3. Representative drawings for carbon allotropes; (a) graphene, (b) fullerene and (c) diamond.

In addition to the widely known carbon allotropes such as diamond and graphene, CNT is another one; technically originated from graphene. Single walled carbon nanotubes (SWCNTs) can be defined as the seamless cylinders with hollow cores formed by the wrapping of a single flat graphene sheet (Figure 4a). In fact, rolling up a graphene sheet is not the true mechanism for the growth of CNTs. The actual growth mechanism will be provided in the next chapter. Other than SWCNTs, there is another type of CNTs called as multi walled carbon nanotubes (MWCNTs) as displayed in Figure 4b. These structures consist of multiple layers of concentric tubes. While the diameter of SWCNTs can be up to 2 nm, MWCNT's diameter changes with the number of concentric tubes varying between 5 – 40 nm. The lengths of CNTs vary from a few micrometers to up to several millimeters (*8–13*).

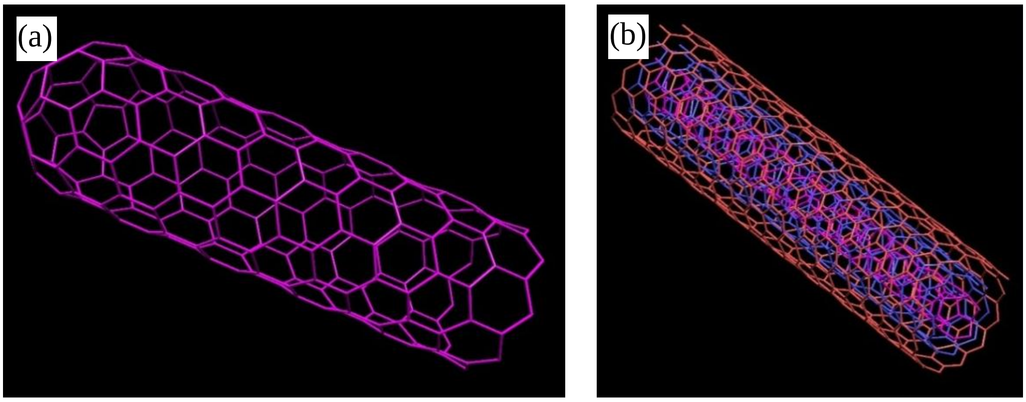

Figure 4. Representative drawings for one end capped (a) SWCNT and (b) open ended MWCNT.

While the resolution of current day scanning electron microscopes (SEMs) can easily allow for the observation of CNTs; their diameter and length, the atomic structure of the sidewalls is generally characterized by using a transmission electron microscope (TEM) (Figure 5a). Atomic force microscope (AFM) and scanning tunneling microscope (STM) are also used for atomic level characterization of CNTs (Figure 5b).

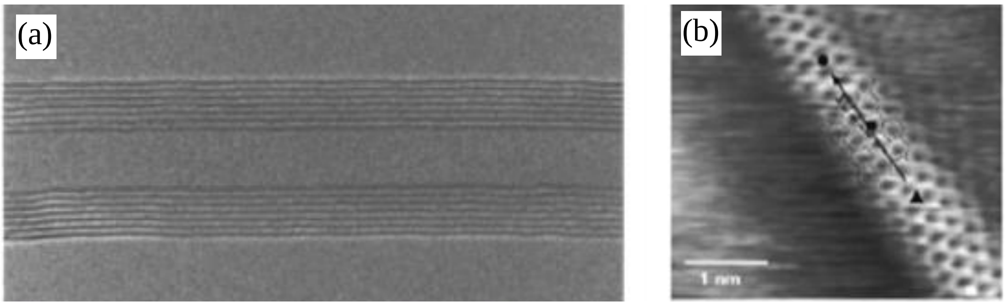

Figure 5. (a) High resolution TEM image of a MWCNT shows the side walls and the hollow core (*14*) while (b) STM image of a SWCNT indicates the atomic sequencing (*15*).

The most widely used analytical technique for the characterization of CNTs is Raman Spectroscopy (Raman). Raman allows for the investigation of the morphology (single or multi walled), electronic properties (semiconductor or metallic), crystallinity and defectivity of CNTs. CNTs have two common Raman active peaks in their spectrum; D (disorder) band around 1380 cm^{-1} and G (tangential) band around 1590 cm^{-1} (*16*, *17*). While D mode corresponds to the breathing like vibration mode of sp^2 sites only possible in hexagonal carbon rings, G mode is the stretching vibration of any sp^2 sites in plane as shown in Figure 6 (*16*, *17*). Figure 6 explains the various factors, which can impact the peak positions of the modes as well as the intensities. The intensity ratio of the

D to the G band for CNTs (*I(D)/(G)*) is to the amount of disorder in the CNT sample. The crystallinity information of CNTs can be obtained by calculating the intensity ratio of G and 2D bands (overtone of the D band) (*I(2D)/(G)*) (*18*, *19*). D and G bands are active in all types of CNTs while another active band exists for SWCNTs. This band prevails in the low-frequency region up to 300 cm^{-1} and is called the radial breathing (RBM) mode. This mode is akin to a finger print for the presence of SWCNTs and can supply a clue for the diameter distribution of SWCNTs in the samples (*20*, *21*). To relate the RBM mode frequencies with the diameter of SWCNTs, a following formula (Eq.1) has been developed with the help of density functional theory (DFT) calculations where w_L is wavenumbers in cm^{-1} and *d* is diameter of SWCNT in nm;

$$w_L = \frac{248\ cm^{-1}}{d} \qquad (1)$$

In addition, Raman spectrum of SWCNTs can be used in determining the chirality of SWCNTs (*22*). Besides the usual electrical conductivity tests, G band splitting in Raman spectrum can provide a clue on electrical properties of SWCNTs as well (*23*).

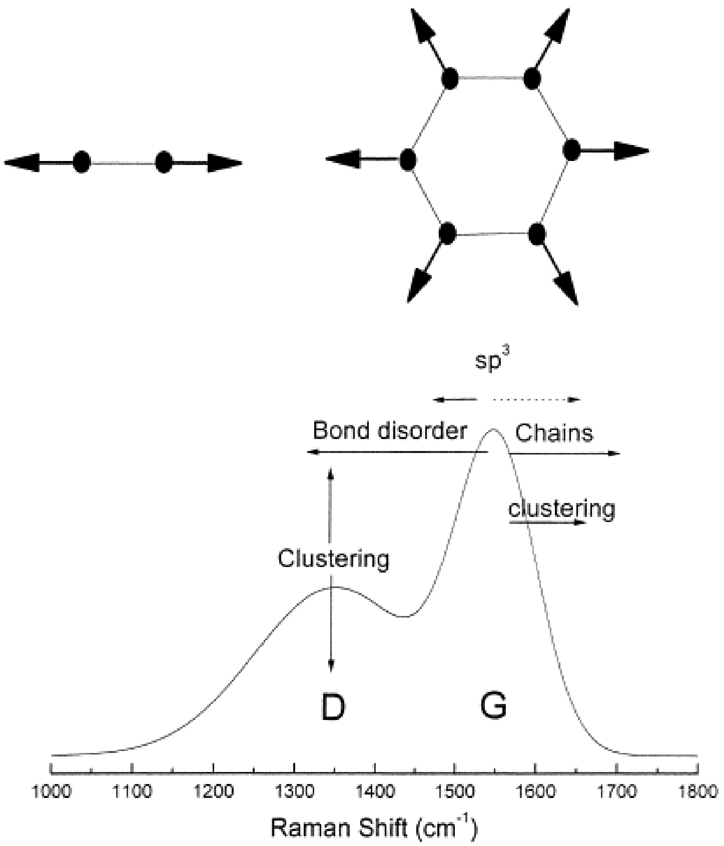

Figure 6. The nature of the G and D modes in Raman for graphite (*16*).

The electrical properties of CNTs depend on the number of sidewalls, diameter and chirality of the CNTs. SWCNTs can be either semiconductor or metallic while MWCNTs are metallic without the introduction of doping elements to the structure capable of carrying current densities up to 10^9 Acm^{-2} (for comparison; the limit for copper is around 10^6 Acm^{-2}) (*15, 24–26*). In general, SWCNTs without any dopants can act as semiconducting materials rather than metallic however, some studies reported that small amounts of dopants such as boron, phosphorous or sulfur can change the electrical properties drastically (*23–25, 27*).

1.3 Thesis objective

As indicated earlier, large-scale commercialization of CNTs requires two major difficulties to be overcome. One is gaining control over the growth of well-aligned, high density CNTs. The other one is regulating and controlling the properties of CNTs through a facile route.

Motivated by the first challenge, an alcohol catalyzed chemical vapor deposition (ACCVD) system was designed to synthesize dense and impurity free vertically aligned carbon nanotubes (VA-CNTs) under various growth conditions. Since the discovery of CNTs in 1991, similar synthesis routes for the growth of VA-CNTs have been followed. However, in this work an attempt at the optimization of the ACCVD process has been made with regards to regulating the VA-CNTs properties for high-volume manufacturing and commercial applications. Furthermore, data gathered during this attempt has been used to build a model of growth for better understanding the growth mechanism. The uncovered growth dynamics of VA-CNTs assisted to build two and three dimensional functional structures on the surfaces through a facile route.

Relevant with the second challenge, the synthesis of VA-CNTs was studied to tailor the surface and structural properties of VA-CNTs using several growth parameters needed no further modifications. For this aim, two different studies of VA-CNTs were conducted; lithium (Li) intercalation and mesenchymal stem cell (MSC) growth. In the Li intercalation study, VA-CNTs were grown already Li intercalated with vertical arrangement which was needed no further lithiation processes. This would provide good conductivity, fast ion diffusion, high rate capacity and surface area for the anode material applications of CNTs in the Li-ion battery field with the help of alignment and lithiation. Furthermore, in the study of MSC growth, VA-CNTs were prepared to be used as scaffolds utilized from the wettability properties of surfaces. VA-CNTs would be an alternative scaffolds for tissue engineering applications compared to the widely used polymer based ones.

Chapter 2

Literature Review

2.1 Synthesis methods for carbon nanotubes

There are many methods to produce inorganic carbon based materials. While graphite presents little trouble during its synthesis, diamond requires precision and harsh environments. Similar to diamond, synthesis of CNTs also requires precision controlled growth parameters and specialized equipment. Regularly, the synthesis of CNTs can be categorized in two main groups with regards to the starting materials; gas-phase and solid-state methods. Laser ablation, arc discharge and pyrolysis techniques are involved in the high-energy group in which CNTs are synthesized by the evaporation of a solid carbon source or a carbonaceous solid; commonly graphite is used (Figure 7). The gas-phase method is the most used one in the literature and it is based on the decomposition of a gaseous carbon source over a metal catalysts as seed for the growth of CNTs. Amongst the techniques utilizing the gas-phase route, catalytic chemical vapor deposition (CVD) technique is the frequently known and used one (Figure 7a).

One of these synthesis methods would meet the needs depending on the desired properties of CNTs. However, the focus of the recent studies is the self-alignment of CNTs in an easy way where they could be easily used for various applications such as sensors and biomaterials. In this section, CVD, laser ablation and arc discharge methods are described.

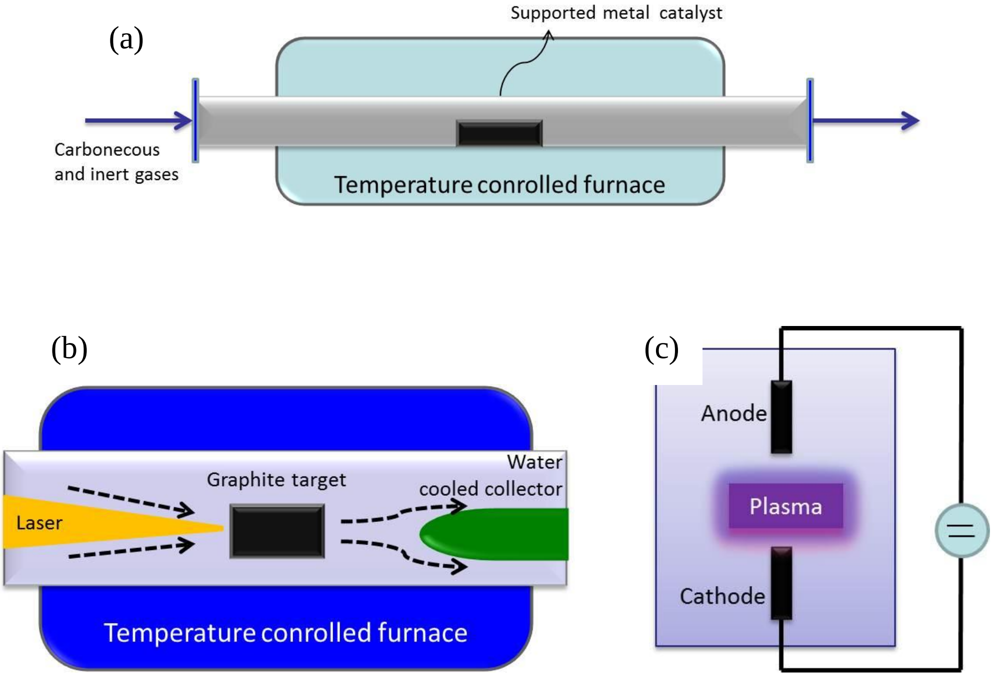

Figure 7. Schematic drawings for (a) CVD, (b) laser ablation and (c) discharge methods.

2.1.1 Chemical vapor deposition method

CVD has become a popular method to grow carbon structures which is partly due to the simple setup and high possibility to be scaled up for industrial production. In the CVD technique, a gaseous carbon source is flowed into a temperature and atmosphere controlled furnace. The carbon containing gas decomposes into reactive carbonaceous species on the hot surface of the substrate with assistance of catalyst layer on the substrate (*28*). As the carbon source cracks, carbon deposits on the catalyst surface and diffuses into the catalyst which will eventually act as a root for growing CNTs (Figure 7a). Commonly, flammable gases such as methane (*29*), acetylene (*30*), ethylene (*31*) and carbon monoxide (*32*) or vapor of alcohols (*11*, *12*, *33*, *34*) are used as carbon source.

The characteristics of CNTs synthesized by CVD method depends on the experimental parameters such as carbon source, catalyst type, operation temperature and pressure of the gas (*35–38*). While SWCNTs are reported to be synthesized at higher temperatures with uniformly dispersed catalyst layer, MWCNTs are grown at comparatively lower temperatures (*35*) and even without a metal catalyst layer (*39*, *40*). In this technique, it is possible to eliminate the impurities, and limit formation of amorphous carbon during the growth of CNTs (*41*). This could be achieved by flowing small amounts of oxidative gases inside the furnace. Thus, this flexibility of CVD process allows for having amorphous carbon free CNTs without any need for an extra purification step. Moreover, self-aligned CNTs can only be successfully synthesized through CVD technique. Hence, alignment of the CNTs can play a key role for the manufacturing of electronic devices.

There are a great variety of catalyst types for the growth of CNTs and numerous ways of applications of catalysts on the substrates. In some reports, the catalyst layers are prepared using liquid base precursors which are applied on the substrates through techniques such as the dip coating and sol-gel methods. These precursors are generally based on acetate (*42*) or nitrate (*43*) solutions of metals. Due to the uniformity and coverage problems of these types of catalyst coating methods, the most commonly used technique in the literature for coating of metal catalysts such as iron, cobalt and nickel (*37*, *44*, *45*) is physical vapor deposition (PVD) methods. The metal catalysts used in the CVD method are supported on various substrates such as metals, oxidized silicon (Si) wafers and alumina (*46*, *47*).

2.1.2 Laser ablation method

In the laser ablation method, a pulsed or continuous laser is used to vaporize a graphite target in a vacuum capable furnace at high temperatures (Figure 7b). The vaporized carbon species are swept by flowing gas and are gathered on a water cooled collector. The material on the collector contains soot and CNTs. Hence an extra purification step is needed after the process. There are studies in the literature reporting the production of CNTs using this technique, while it is not possible to synthesize self-aligned CNTs (*48*, *49*).

2.1.3 Arc discharge method

The arc discharge method is based on the synthesis of CNTs by generating electric arc between two graphite electrodes under an inert atmosphere (helium or argon) at low pressures (Figure 7c). The carbon vaporizes from one of the electrodes (anode) into the plasma and deposited on the other rod (cathode) which is cooled down and where the CNTs are formed (*50*, *51*). Although the original discovery of CNTs was done through using this technique (*1*), it is not surprising to have a mixture of soot and CNT at end of the process as well as non-aligned CNTs.

2.1.4 Pyrolysis

Besides the others, pyrolysis based methods are also known to produce CNTs. The basis of the technique is to sublime and decompose a carbon-based precursor at high temperatures under the flow of inert gases inside a high temperature furnace. Solid or liquid carbon precursors can be used in this technique. While the solid precursors are placed inside the furnace before heating starts, the vapor from the liquid precursors are generally introduced into the furnace by a sweeping gas such as argon (Ar), nitrogen (N_2) or hydrogen (H_2) (*52*). Generally, hydrocarbons and alcohols are used for the carbon source and organometallic compounds for the catalyst to synthesize CNTs using this method (*53–55*). Similar to the arc discharge and laser ablation methods, the product contains CNTs as well as soot at the end of the process.

2.2 Growth mechanism of carbon nanotubes

Commonly, the accepted mechanism for CNT growth is originated from carbon atoms dissolving into the catalyst to form CNTs. This is based on the vapor-liquid-solid mechanism suggested for whiskers growth (*56*). In this model, the catalyst is in a liquid form and adsorbs the reactant gases around which cause the super saturation of the catalyst resulting in the eventual precipitation/growth of a solid product (whisker). The growth of CNTs by catalytic methods includes the four sequential steps shown in Figure 8. These are; (1) carbon source adsorption, (2) dissociation of precursors on the catalyst surface, (3) carbon bulk or/and surface diffusion and (4) carbon precipitation at the catalyst – CNT interface. The carbon sources such as methane and acetylene require these gases dissociating into carbon at the catalyst surface at elevated temperatures. Hence, this step is the crucial for the growth of CNTs. Then, carbon atoms on the surface diffuse over or through the catalyst, which is determined by the catalyst type and growth conditions. The diffused carbon reaches back to the surface and precipitates at the catalyst – CNT interface. The precipitation starts at the edge of catalyst where the surface activation energy is the lowest.

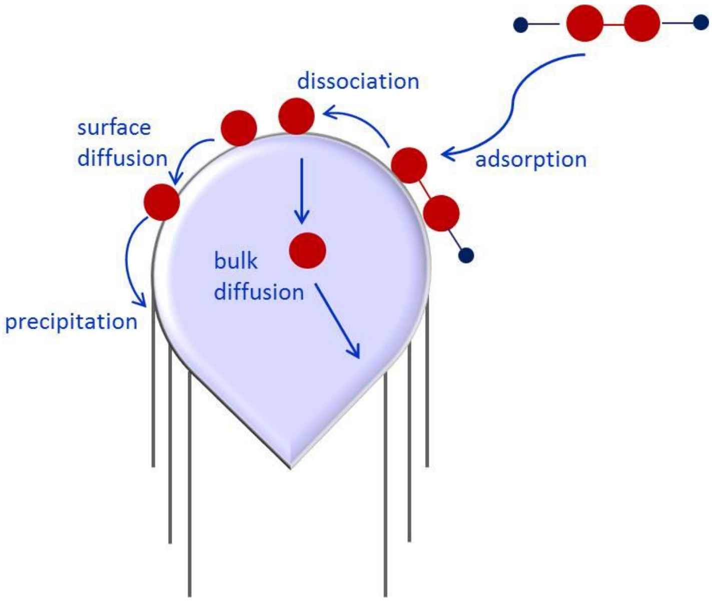

Figure 8. Schematic representation of processes occurring on the catalyst particle during the growth of a CNT.

Generally, the carbon diffusion over or through the catalyst particle is assumed to be the rate limiting step eventually leading to the termination of CNT growth (*57*, *58*). However, this is not enough to explain the effects of catalyst quality and carbon precursor type on the growth. In a study by Robertson *et al.*, it is shown that the CNT growth termination mechanism is actually more complex than explaining it by one rate limiting step (*59*). Both diffusion step and molecular dissociation was shown to have an effect on the growth kinetics. Moreover, it is reported that during synthesis of self-aligned CNTs as the CNTs get longer the decrease in the growth rate were attributed to the slowing rate of the diffusion of carbon feedstock rather than the carbon diffusion to the catalyst (*60*). In this case, hydrocarbon precursors experience difficulty in reaching the catalyst hence the adsorption step which is the initial step for the growth will be severely stunned.

Overall, there are two growth models for CNTs; base and tip growth models (Figure 9). In the base growth mechanism, the CNT grows while the catalyst stays on the support due to the strong interaction between the support and catalyst (Figure 9a). Arriving carbon atoms are added to the structure from the bottom of the CNT where the catalyst is located. Nevertheless, for the tip growth model, catalyst particle is lifted off the support by the CNTs due to the weaker interaction between catalyst and support (Figure 9b). In this model, the decomposed carbon is precipitated to sidewalls from the top where the catalyst is. Any of the mechanisms could be responsible for the growth of CNTs during CVD depending on the carbon source, growth temperature, types of catalyst and support. In the literature, there is one study linking the oxidation state of the catalyst to whether the base or tip growth would be taking place (*61*). According to the study, if the catalyst is partially oxidized first the reduction of the catalyst is induced by the reducing atmosphere found in CVD systems. Hence, carbon will deposit on the metal rich part of the oxidized catalyst which is generally the top of the particle. Hence, the use of oxidized catalysts will lead to a base growth model. Conversely, in the case of metallic catalyst, carbon diffuses into the whole particle and it preferentially deposits on the edge of the catalyst particle which leads the tip growth model. Contrary to the study summarized above by Bernier *et al.* (*61*), there are studies suggesting the effect of the buffer (support) layer and the interaction between the buffer and catalyst layers on the growth models (*62–64*). Furthermore, the pretreatment and growth conditions also govern the growth mechanism. Hence, the growth models for CNTs should be considered case-by-case for each individual system.

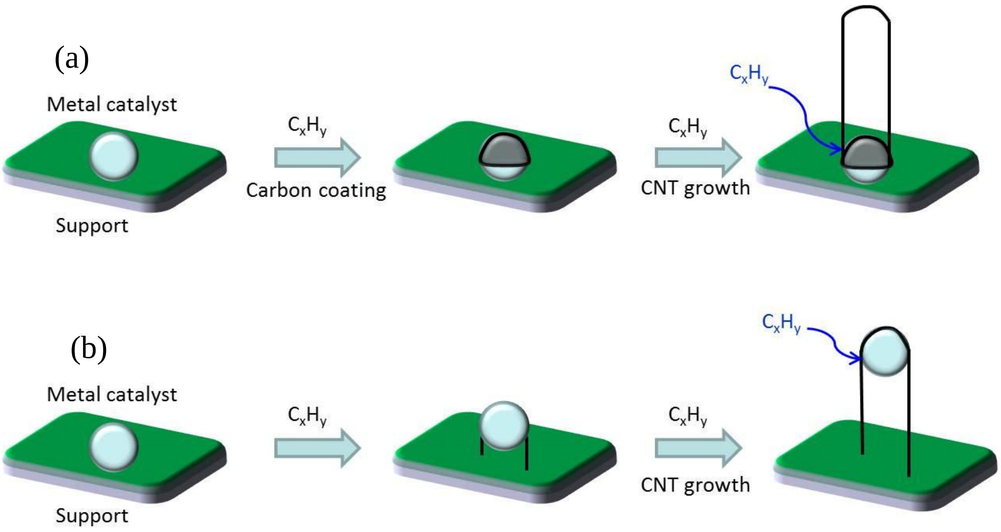

Figure 9. Representative drawings show the (a) base and (b) tip growth models of CNT.

2.3 Synthesis of vertically aligned carbon nanotubes

Through the advances in the growth techniques, the synthesis of CNTs is no more a significant struggle. Yet, starting with the last decade, the current challenge is to synthesize aligned CNTs on a desired surface for various applications. For example, in the field of thin film transistors, while the best reported electron mobility for the randomly scattered CNTs is around 30 $cm^2V^{-1}s^{-1}$, it is 1300 $cm^2V^{-1}s^{-1}$ for aligned ones (*65*, *66*). Moreover, it is reported that the use of powdered CNTs could be toxic for cells, which is in contrast to the studies noting the affirmative effects of the aligned and attached CNTs on the viability of cells (*67*, *68*).

In the literature, well-oriented CNTs have been successfully synthesized mostly using the CVD method due to the earlier mentioned advantages of the technique (*69*, *70*). The orientation of CNTs could be controlled either in horizontal (*71*) or vertical direction (*8*). Generally, well-oriented CNT arrays do not contain impurities and almost all of them are identical in terms of size. Other than direct growth of aligned CNTs, there are post synthesis assemblies for controlling the alignment of randomly scattered CNTs. The post synthesis techniques involve dispersing CNTs in liquid solutions and then orienting them using spin coating, and with the application of magnetic and electrical fields (*72*). Although the post synthesis methods are relatively simple to apply, they have problems leading more defects and contamination due to the used liquid solutions for dispersion (*72*).

The first synthesis of VA-CNTs was achieved by Li *et al.* at 1996 (*73*). In the report, VA-CNTs were synthesized by CVD technique using iron nitrate embedded in mesoporous silica (Figure 10a - c) (*73*). SEM and TEM analysis indicated that the CNTs were thick and short. As mentioned before, flammable gases such as methane (*29*), acetylene (*30*), ethylene (*31*) are commonly used for CVD and these hydrocarbon sources decompose on the catalyst surface by leaving excess carbon behind causing the termination of VA-CNT growth.

Hence, later on, Hata *et al.* at 2004 has shown that by the addition of small amounts of water vapor in the synthesis environment, the accumulated extra amorphous carbon on the catalyst was removed allowing for taller VA-CNTs (*8*). Hata and his group produced the millimeter tall VA-CNTs as a result of the increased catalyst lifetime and activity by water vapor addition and called this process as “super-growth” (Figure 10d) (*8*).

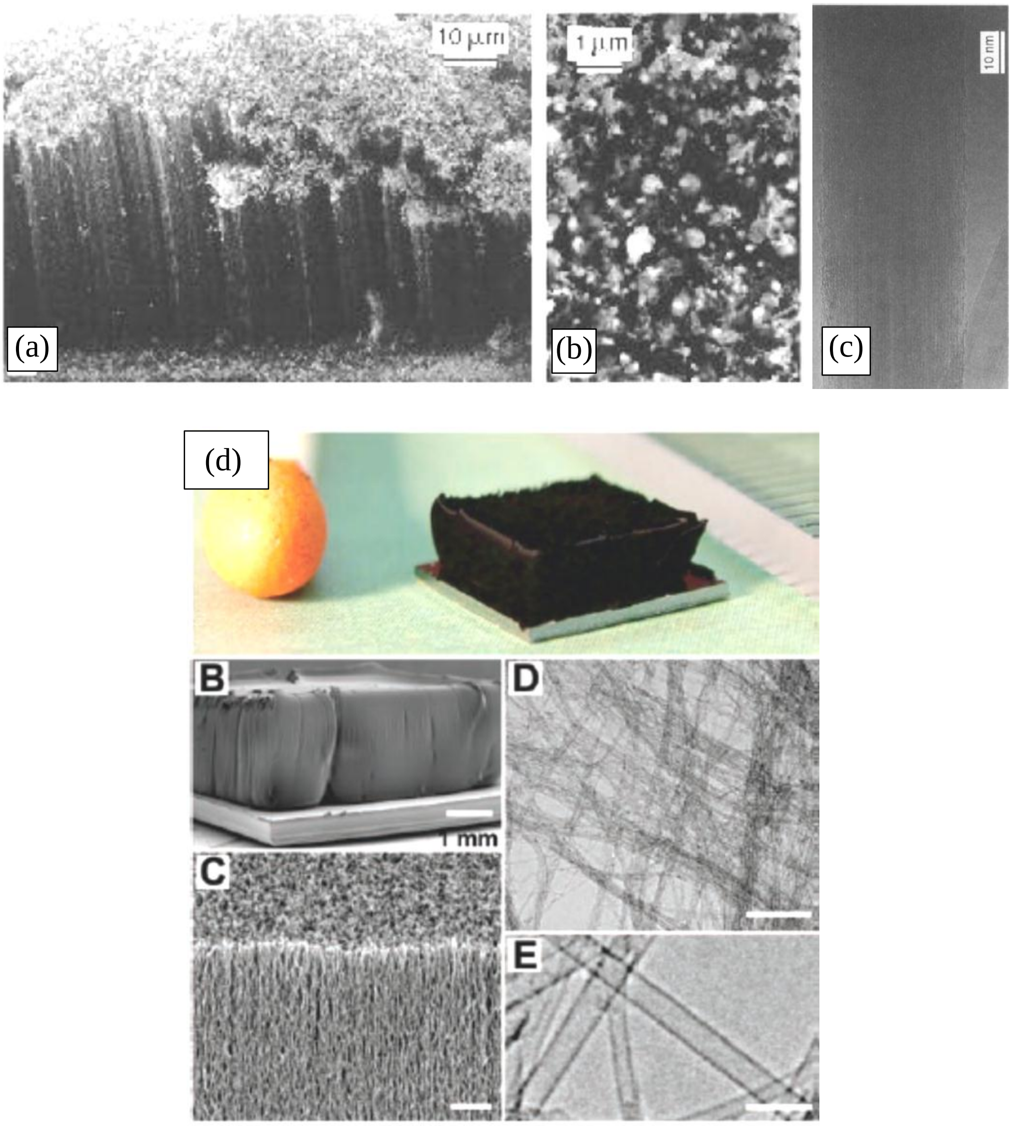

Figure 10. (a-c) The first reported VA-CNTs by Li *et al.* at 1996 (*73*). (d) By Hata *et al.*, the millimeter tall VA-CNTs synthesized using water assisted CVD are compared with a match for a size reference (*8*).

As mentioned before, the purity of VA-CNTs is one of the most important parameters for applications in the electronics and material science fields. It was found that the addition of oxygen containing species to the reaction chamber during the growth of CNTs had a great effect on the size and purity of VA-

CNTs and these oxidative species were called "growth enhancers" (*8*, *41*, *74*, *75*). Particularly, the water addition had an significant impact when hydrocarbon sources are used to synthesize CNTs (*9*, *76*). Furthermore, there are recent studies in the literature for the use of growth enhancers other than water vapor such as carbon dioxide (CO_2) and oxygen (O_2) to synthesize impurity free and longer VA-CNTs (*77*, *78*). In these reports, it was found that CO_2 and O_2 had the same role as an etching agent to keep the catalyst from poisoning. Contrary to the study reporting the enhancing effect of O_2 on the catalytic activity (*78*), Hauge *et al.* reported that even trace amounts of O_2 could be detrimental for the catalyst (*79*). It is likely that water may react with the catalyst and could be saturating the surface with hydroxyl groups (*79*). In the case of CO_2, H_2 gas should be introduced into the growth environment to result in reaction with CO_2 to form water and which then achieves the surface hydroxylation as well as the etching of excess carbon (Rxn. 1 and 2). Moreover, Hauge *et al.* suggested that the surface hydroxylation also keeps the catalyst from coarsening (*79*).

$$CO_2(g) + H_2(g) \rightarrow CO(g) + H_2O(g) \qquad \text{(Rxn. 1)}$$

$$C(s) + H_2O(g) \rightarrow CO(g) + H_2(g) \qquad \text{(Rxn. 2)}$$

Other than hydrocarbon sources, alcohols are another one of the commonly used carbon sources during CVD method for the growth of VA-CNTs (*33*, *34*). Alcohol usage for the VA-CNT synthesis provides a significant advantage in discarding the amorphous carbon formation on the catalyst surface without introducing any extra oxidative compounds such as water and CO_2. During synthesis in the CVD furnace, alcohols are decomposed into species containing OH radicals which can efficiently remove the unwanted amorphous carbons from the catalyst surfaces and etch away the ends of the CNTs keeping them clean (*80*, *81*). In a study by Oida *et. al.*, the effect of various alcohol sources such as methanol (CH_3OH), ethanol (C_2H_5OH) and isopropanol (2-C_3H_7OH) on the growth of VA-CNTs using hot filament CVD reactor has been investigated (*82*). In the study, they reported that the shortest CNTs were grown with methanol, while ethanol resulted in the longest CNTs (*82*). Hence, it was suggested that the growth rate is a competing race between two mechanisms; deactivation (oxidation) and poisoning (amorphous carbon coating) of the catalyst and it is not simply related with the ratio of C/OH. It is reasonable to compare the decomposition rate of alcohols using their standard enthalpy of formation. Ethanol has a higher enthalpy value than methanol meaning to a slower decomposition than methanol as well as the slower generation of oxidative species. Hence, the growth of CNTs would be expected to be affected by the rate of these competing reactions (*82*). In the literature, there are also reports indicating the effect of carbon precursors on the quality of CNTs (*83*–*85*).

As mentioned before, the carbon source is not the only parameter influencing the growth and properties of VA-CNTs. The configuration and thickness of catalyst and buffer (support) layers are used to control whether the growth would be in vertical or horizontal directions. Mostly, PVD techniques are preferred to be used in depositing the catalyst layers. Recently, the studies done by McLaughlin *et al.* (*86*) and Liao *et al.* (*87*) investigated the effect of the aluminum (Al) buffer layer thickness on the growth of VA-CNTs. It was found that thin Al layers with an average thickness around 5 nm was the optimum for growing longer VA-CNTs compared to the thicker Al layers. Two possible mechanisms were suggested for the increase in length of CNTs with decreasing in Al thickness. The first one is that the retardation of carbon diffusivity in the catalyst with increasing Al content resulting the slower growth and the second is the change in the size of the catalyst islands subjected to the thermal treatment (*86*, *87*). The catalyst islands grow as the thickness of buffer layer increases as shown in Figure 11. In another report done by Burt and co-workers, the effect of Al grain size was studied on the CNT growth (*88*). The grain size of Al buffer layer was altered by elevating the temperature during the Al deposition process. It is found that the highest deposition temperature of Al layer resulted in the tallest VA-CNT length due to the reduced grain size of Al layer. Moreover, it is also reported that the grain size of Al layer was higher on the silicon oxide (SiO_2) than Si surfaces due to the wetting properties of Al on the Si based surfaces (*88*).

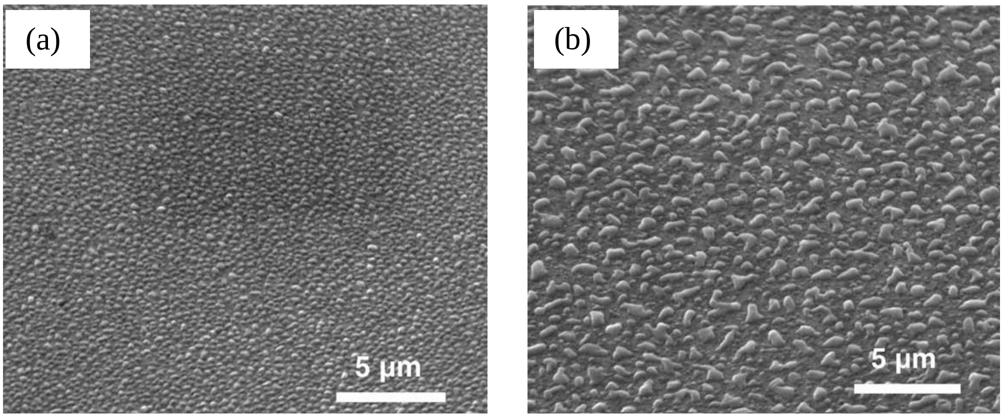

Figure 11. SEM images of the catalyst islands formed on (a) 0.5 nm and (b) 6 nm Al buffer layer (*86*).

Commonly, VA-CNTs are grown on the Si and Al based substrates due to their possible electronic applications. Moreover, there are a number of studies using quartz and glass for the VA-CNT growth (*42*, *89*, *90*) as well for the growth of horizontally aligned CNTs (*91*). In another study, Al, Al_2O_3, TiN, and TiO_2 coatings were used as support layers to synthesize VA-CNTs using CVD technique (*92*). It is found that the CNTs was not aligned on the Al and TiO_2 layers while the well aligned CNTs was observed on the Al_2O_3 surface as well as on the TiN substrates (Figure 12). Hence, it was suggested that the chemical state of the catalyst islands during the growth process changed according to the type of buffer layer (*92*).

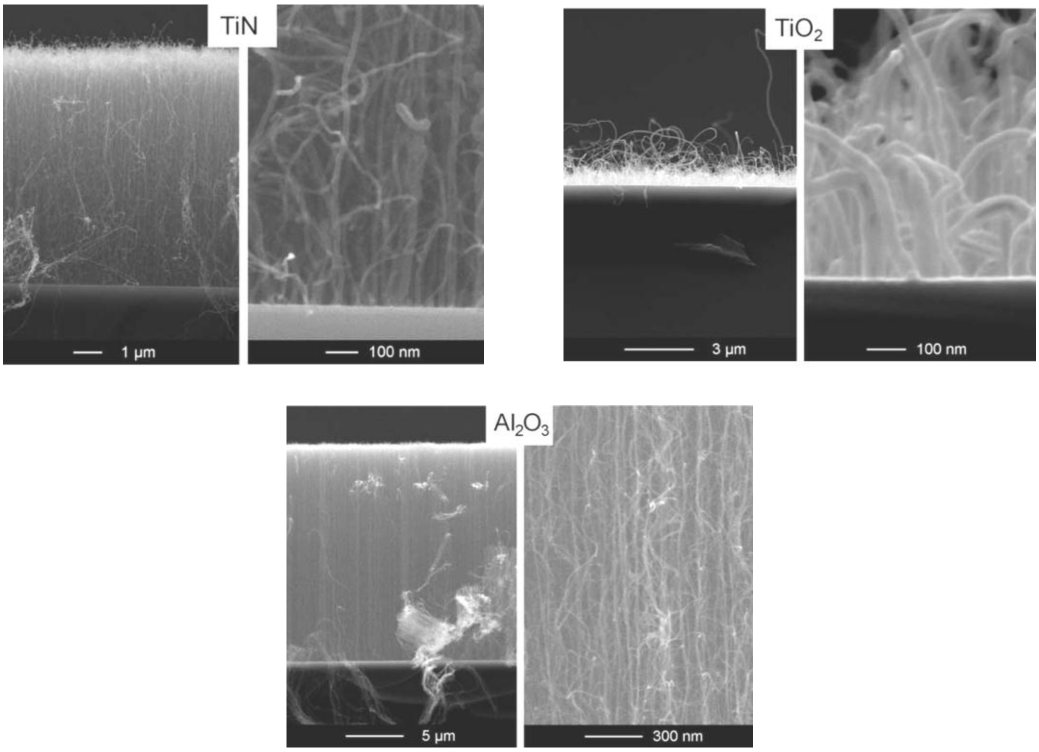

Figure 12. SEM images of CNTs on Si substrates with TiN, TiO_2 and Al_2O_3 buffer layer (*92*).

Beside the effect of buffer layers on the growth, the activity of catalyst layers was also found to be strongly depending on the type of carbon source. A survey of literature shows that there is selective matching between the catalyst particles and the carbon source to enhance the performance of the catalyst. In a study by Choo *et al.*, it is reported that the growth rate of VA-CNTs on the Fe catalyst layer was higher than Co and Ni where ethylene was used as the carbon source (*93*). However, the growth rate enhancement is not the only effect on the CNTs. TEM images showed that the degree of crystallinity of the CNTs changed with the catalyst type. It was suggested that the rate of bulk diffusion of carbon atoms determined the growth rate which could be affecting the defect formation and

(*93*). Also, other studies reveal that Fe as a catalyst performs better for decomposing hydrocarbon sources while alcohol based sources are cracked on the Co catalyst layer more efficiently (*94–96*). The possible reasons for the selectivity are the decomposition rate differences for each carbon sources on the catalysts and the deactivation rate of the catalysts. It is reported that Co can be easily deactivated by the accumulation of amorphous carbon on the surface than Fe and thus the use of alcohols as carbon sources would help to extend the catalyst life by etching a way the excess carbon (*94*).

2.4 Vertically aligned carbon nanotubes as multi-functional surfaces

CNTs have fascinating for scientists due to their unique properties leading to their possible applications in numerous fields. Since the last decade, aligned CNTs are becoming more popular due to the simple handling, denser and orientated arrangement. Hence, there are reports using VA-CNTs for potential applications as field emission materials (*97*), sensors (*98*), supercapacitors (*99*) and catalyst support (*100*). In this section, the applications of VA-CNTs for Li-ion battery materials and biological scaffolds will be discussed.

2.4.1 Anode material for lithium ion battery

A typical Li-ion battery consists of a conducting electrolyte and two electrodes; an anode (made of carbon based materials) and a cathode (made of a Li-containing metal oxide) (Figure 13). During charging process, Li ions are extracted from the cathode and diffuse into the anode and intercalation of Li into the carbonaceous anode takes place. Upon discharge, Li ions are delivered by the anode and inserted into the cathode. During charge-discharge cycles, a passive layer forms on the anode comprising of organic and inorganic decomposed electrolyte in the first charging cycle. This layer is named solid electrolyte interphase (SEI) and consumes some of the Li irreversibly.

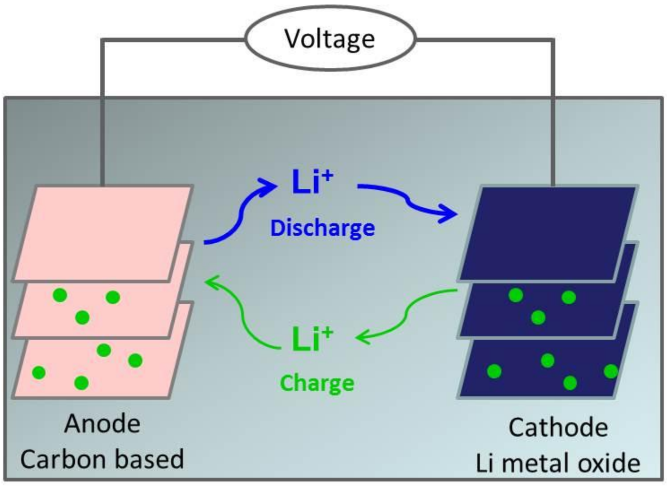

Figure 13. Working principle of Li-ion battery showing the charge-discharge cycle

Carbon based materials are the primary candidates for electrode applications in Li-ion batteries due to their structural stability (*101*). However, there exist some limitations for the use of conventional carbon based materials which are slow ion diffusion, low surface area, low lithiation capability and poor conductivity. To overcome these disadvantages, the introduction of CNTs as an electrode material has been studied to provide higher lithiation and an overall better performance (*102–104*). Furthermore, there are reports in the literature for improving Li adsorption capacity of the CNT based anodes by numerous ways such as doping, functionalizing, defect engineering, hybridizing CNTs with fullerenes and *ex situ* doping of CNTs with Li (*103*, *105*).

VA-CNTs are recently used as electrodes to enhance the conductivity and the rate capacity for the charge transfer (*104*, *106*, *107*). Moreover, the alignment of CNTs increases the Li ion diffusion during the charge cycles. Durstock *et al.* have shown the enhancement in the storage and rate capacities of anode materials when as synthesized VA-CNTs were used as electrodes (*104*). These values were even higher than the ones for the graphite and randomly scattered CNTs emphasizing the role of alignment (*101*, *103*). Further improvement in the conductivity has been studied by using VA-CNTs grown on stainless steel substrates (*108*).

Beside the carbon based structures, Si material would be used as an anode which has the highest specific capacity even higher than graphitic carbon. However, it has two major limitations; very fragile due to the high volume expansion during charging and non-conductive material. Hence, new hybrid structures are proposed to overcome the limitations of Si and CNTs. Recently, there are studies using composite materials made of VA-CNTs and Si (*106*, *107*). In these, VA-CNTs were first synthesized and then decorated with Si nanoparticles. As a result of electrochemical tests, it is found that such a hybrid material exhibited the best rate capability ever reported for Si based and VA-CNT based electrodes (*106*, *107*). Moreover, there was no structural damage observed for CNTs (*106*, *107*).

2.4.2 Extracellular matrix for cells

In recent years, owing to the multiple-lineage potentials and immune-privileged properties, MSCs have become a feasible and potential source for the cell-based therapy and tissue engineering applications due to their proliferative and differentiation capabilities. MSCs, which are also called as bone marrow stromal cells, have the ability to differentiate into other types of cells such as adipocytes, chondrocytes, osteocytes and cardiomyocytes without inducing any immune reactions in the host.

A key issue in MSC based tissue engineering is to control the growth and differentiation of cells. Extracellular matrix (ECM) has an important role in proliferation and differentiation of MSCs (*109*). Commonly, used ECMs are consists of protein fibers such as collagen and elastin and these are extracted from animal tissues. However, these structures are limited by the dimension and the potential pathogen risk (*110*). Therefore, there has been a tremendous demand to develop better scaffolds which mimic the surrounding native tissue.

As an alternative to common used scaffolds, CNTs can be considered due to the similar sizes with collagen fibers (*111*). Giersig *et al.* formed regular 3D patterns on the surface of VA-CNTs and then fibroblast cells were successfully grown on the surface (*112*). Moreover, VA-CNTs have also been reported as a suitable scaffold material due to their superb electrical conductivity to guide the growth of cells (*113*).

The used form of CNTs in cell experiments has a profound role at the viability of cells. While the powder and liquid use of MWCNTs induced DNA damages in mouse embryonic stem cells (*67*), Corat *et al.* (*68*) and Giersig *et al.* (*114*) reported that adhesion and growth of fibroblast cells was achieved successfully without having any toxic effects of VA-CNTs which were already attached firmly to a substrate. Later, further cell viability tests were conducted using VA-CNTs and cells and Corat *et al.* reported that VA-CNTs are not toxic to cells (*68*, *115*). Regarding to these reports in the literature, the use of VA-CNTs could provide a great advantage for biomaterial applications.

Chapter 3

Materials and Method

In this chapter, the synthesis and characterization techniques are briefly described. The first section of this chapter reviews the experimental procedure followed during the work for the synthesis and application of VA-CNTs using ACCVD method. In the following section, characterization techniques and parameters used for the physical and chemical analysis of the surfaces are reviewed.

3.1 Experimental procedure and equipment

In this study, ACCVD method was used to synthesize VA-CNTs. The alignment of CNTs was easily managed using this technique which consists of three steps (Figure 14);

- Step 1: preparation of catalyst layers
- Step 2: annealing of catalyst layers
- Step 3: growth of VA-CNTs

For the first step, two different catalyst preparation methods were followed for different purposes in this study. One of these is based on the thin film technology achieved by PVD techniques while the other is the wet chemistry based method. These techniques will be described particularly at the following section. After the preparation of catalyst layers, the surfaces were conducted to Steps 2 and 3 inside the ACCVD furnace. Figure 14 shows the summary of catalyst preparation methods as well the steps performed inside the ACCVD furnace.

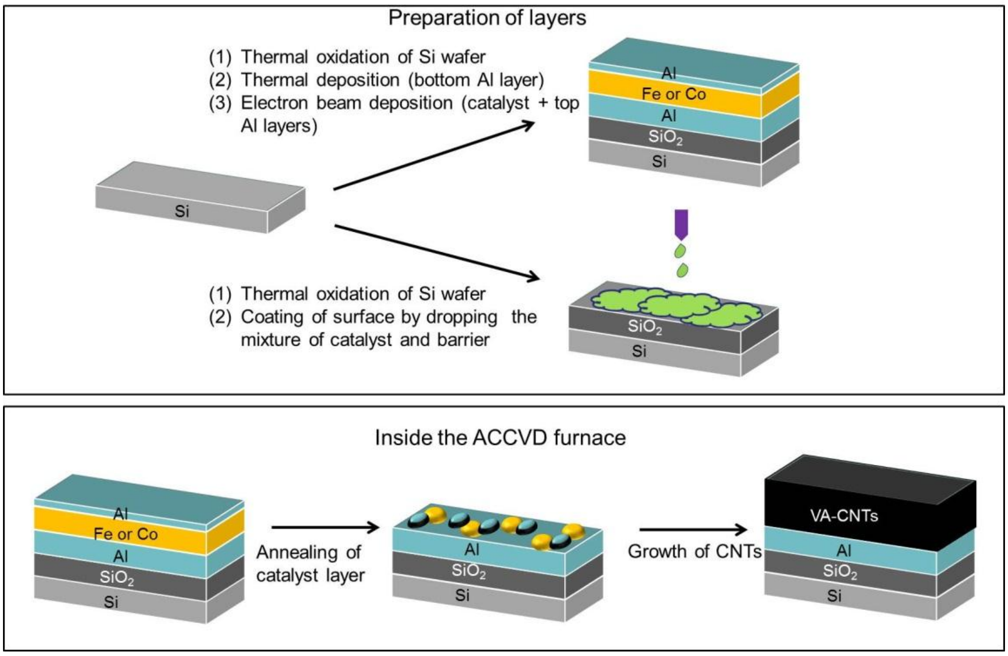

Figure 14. Schematic representation shows three steps for the synthesis of VA-CNTs; preparation of catalyst layers, annealing and growth. The annealing and growth steps are performed inside an ACCVD furnace.

3.1.1 Preparation of catalyst layers

3.1.1.1. Physical vapor deposition method

First, a pre-cleaned Si (100) wafer was oxidized thermally at 900 °C for 30 minutes to have a 30 nm thick layer of SiO_2. This SiO_2 layer on the Si wafer was used as a substrate in this study. Following the oxidation step, Al layer was deposited on a SiO_2 wafer using a thermal evaporation system at 2×10^{-6} mbar pressure with an average deposition rate of 0.5 Å/sec (Figure 15a). The thickness of Al layer was varied as 3, 5, 7 or 10 nm. Al pellets with a purity of %99.9 were used as Al source in the thermal deposition system (Ted Pella Inc.). The purpose of the bottom Al layer in this study is to inhibit the diffusion of catalyst particles to the substrate and to minimize the agglomeration of particles during the ACCVD process. Subsequently, a 1 nm thick catalyst layer either Fe or Co was deposited on the top of Al layer using the electron beam (e-beam (I)) deposition technique (Figure 15b). During the e-beam (I) deposition, the chamber base pressure was kept around 10^{-7} Torr and the deposition rate was 0.1 Å/sec. Fe and Co powders with high purities were used for e-beam (I) (Sigma Aldrich, %99.99). In this study, substrates after the catalyst layer depositions which are ready for ACCVD growth are defined as 1nm Co/10nm Al and also named as “normal catalyst configuration” (Figure 16). Other than this design, a sandwich catalyst configuration was also used where a second layer of Al (top Al layer) was deposited on the catalyst layer to pin and inhibit the coarsening of catalyst particles (Figure 16). 0.5 nm thick Al layer was put on a 1 nm thick catalyst layer using the e-beam (I) deposition system at 0.1 Å/sec rate under 10^{-7} Torr pressure (layer configuration is 0.5nm Al/1nm Co/10nm Al). The samples prepared by using PVD methods were used for the experiments performed to understand the effects of parameters and growth mechanism of VA-CNTs.

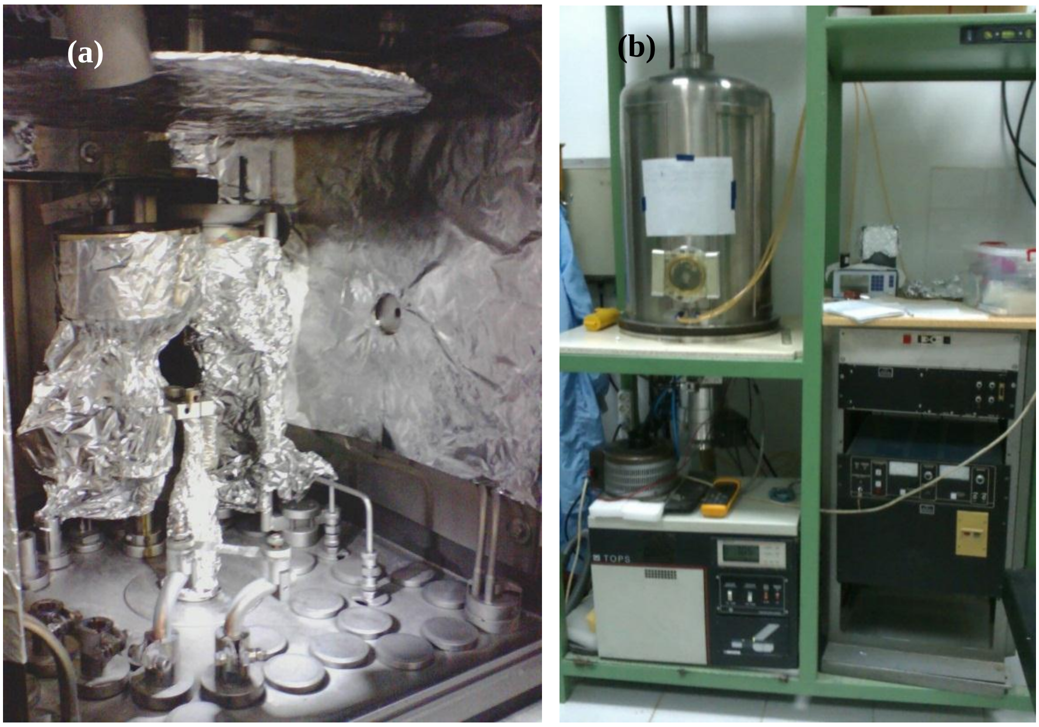

Figure 15. Photograph of (a) thermal and (b) e-beam (I) evaporation systems.

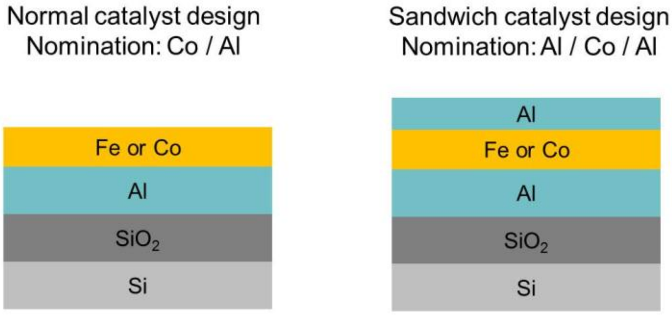

Figure 16. Drawings for the catalyst configurations used in the experiments.

Beside the use of e-beam (I) deposition, another PVD instrument; EBE-4 (II) was also used for the deposition of Co catalyst layer on the 10 nm thick Al layer (Figure 17). The deposition using the EBE-4 (II) instrument is also based on the electron beam deposition technique. However, using this instrument provides a valuable advantage for the analysis of catalyst layers without exposing layers to air due to vacuum transfer ability between the chamber of EBE-4 (II) and the chamber of X-ray photoelectron spectroscopy instrument (XPS). Using the EBE-4 (II), 1nm thick Co catalyst layers were deposited on the 10nm thick Al layers with a rate of 0.05 Å/sec while a second layer of Al was not coated on these samples (indicated as 1nm Co●/10nm Al). %99.999 purity of Co rod was used as a metal source (Ted Pella Inc.). This deposition technique was only used when the catalyst layers will be analyzed by XPS without exposing to air.

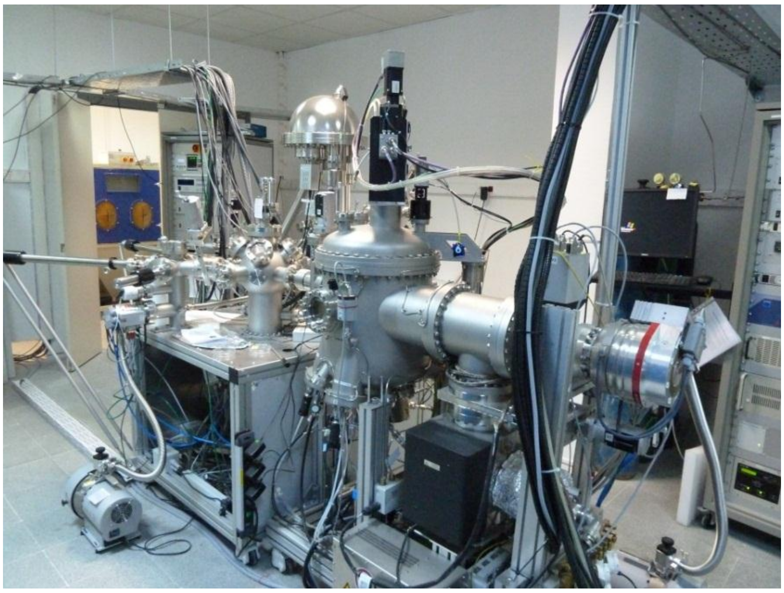

Figure 17. Photograph of EBE-4 (II) system mounted with XPS.

3.1.1.2. Wet chemistry method

VA-CNTs were also grown on the catalyst layers prepared through the wet chemistry technique which is based on dissolving nitrates of cobalt ($Co(NO_3)_2.6H_2O$), aluminum ($Al(NO_3)_3.9H_2O$) and lithium ($LiNO_3$) and then subsequently coating the substrates using the mixture of these solutions. In this study, VA-CNTs grown on catalyst layers prepared through the solution based method were only used for Li intercalation study.

For Li intercalation study, two types of catalyst solutions were prepared. The first one was a Li containing catalyst solution prepared by dissolving $Al(NO_3)_3.9H_2O$, $Co(NO_3)_2.6H_2O$ and $LiNO_3$ (molar ratio of Al/Co/Li is 1/1/1.4) mixture in 10 ml ethanol, and the second was without Li. The second catalyst solution was which $Al(NO_3)_3.9H_2O$ and $Co(NO_3)_2.6H_2O$ (molar ratio of Al/Co: 1/1) were mixed in 10 ml ethanol solution. All the reagents were from Sigma Aldrich (ACS reagent ≥ 98%). After mixing these two solutions for an hour on a magnetic stirrer, the corresponding solution was applied on the oxidized Si (100) substrates ($1 \times 1\ cm^2$) by using a micropipette (volume of solution is about 40 μL). Then, the substrates were left for air drying under ambient conditions. Following these steps, the substrates were treated in the ACCVD for the growth of Li intercalated VA-CNTs.

3.1.2 Synthesis of vertically aligned carbon nanotubes

The synthesis of VA-CNT forests were achieved using an ACCVD furnace designed and built in the Department of Chemistry at Bilkent University (Figure 18). As mentioned before, ACCVD process is consists of two steps, annealing of catalyst layers (Step 2) and growth of CNTs (Step3). The prepared catalyst layer was first subjected to the annealing process and then to the growth process inside the ACCVD furnace under a controlled atmosphere.

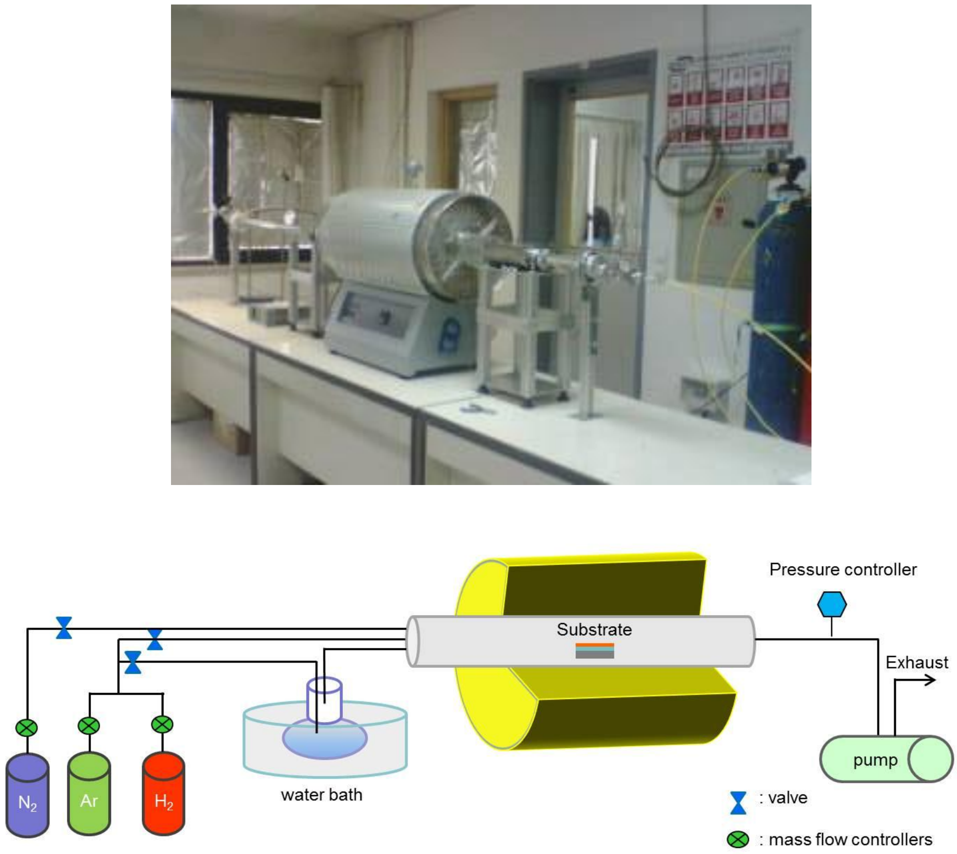

Figure 18. Photograph and schematic drawing of the ACCVD experimental set up.

In the annealing step, a catalyst layer was reduced at either temperature of 625 °C or 750 °C and pressure of 4 Torr under a flowing atmosphere of 20 sccm H_2 and 100 sccm Ar. This step is also called as reduction (annealing) step which is required to have uniform catalyst islands on the Al/SiO_2 layer for initiating the CNT growth. During this study, optimization of the reduction step was performed at 625 °C by varying the reduction time; 5, 10, 15, 20, 30 and 60 minutes.

Following the reduction step, the annealed catalyst layer was conducted to the growth inside the ACCVD furnace either at temperature of 625 °C or 750 °C. During the growth, 100 sccm Ar and 20 sccm H_2 gases are flowed through a bubbler containing the liquid carbon source to sweeping its vapor to the furnace. To keep the temperature of liquid carbon source constant during the growth, the bubbler is placed inside a water filled tank kept at 32 °C unless otherwise mentioned. For this study, as for the liquid carbon sources toluene, benzene, ethanol, acetone and isopropanol were used for the growth. If otherwise is not mentioned, the growth process was run for 30 minutes at 40 Torr pressure.

3.2 Characterization techniques

3.2.1 Raman spectroscopy

Micro Raman equipment (Horiba Ltd., LabRAM HR model, Kyoto, Japan) was used at the wavelength of the Ar ion laser, 514.5 nm. In order to calibrate the instrument before data collection, the spectrum was adjusted to zero wavenumber. All Raman data in this study was collected with 600 groove/cm grating using a 50× objective lenses and averaged for 10 times. Deconvolution of Raman spectrum was performed with the aid of spectral analysis software (Peak Fit version 4.12). To obtain D and G band positions and intensities, a spectrum was fitted using a function of Gaussian–Lorentzian type peak fitting.

3.2.2 Atomic force microscopy

AFM (Nanomagnetics Ltd.) analysis was performed on the prepared and annealed catalyst layers using contact mode with a force constant of 0.7 – 1 V. 512 × 512 resolution AFM images were taken with a scan speed of 0.6 μm/s while there was no applied bias voltage to the samples. All topography images were equalized in x and y directions to correct the plane. No image filtering was applied during data processing.

3.2.3 Scanning electron microscopy

SEM (Carl Zeiss Evo 40) with an energy-dispersive X-ray (EDX) spectrometer was used for imaging samples. For determining alignment and length of CNTs, VA-CNT sample grown on Si wafers was prepared as following; first it was cut into two parts and then pasted on a 90° tilted stub for side view imaging. A relatively high voltage setting (10 kV) was used for high vacuum mode imaging.

Biological samples (cells on CNTs) were imaged using SEM at low vacuum mode (at 40 bar of water vapor pressure) to prevent shrinkage of cells. 10 kV accelerating voltage was set for imaging.

3.2.4 Transmission electron microscopy

For TEM (JEOL 200kX) imaging, VA-CNT samples were prepared by sonicating the samples in a 10 ml of ethanol. Then, a few drops were taken from the suspension and dropped onto a copper based holey-carbon TEM grid. High resolution TEM (HRTEM), Scanning TEM (S/TEM) and low resolution imaging were made at the accelerating voltage of 300 kV. Electron energy loss spectroscopy (EELS) mounted in the TEM instrument is utilized to obtain chemical information about VA-CNTs. In this study, EELS has been used to understand the chemical structure of CNTs intercalated with Li.

3.2.5 X-Ray photoelectron spectroscopy

The XPS analysis were performed in an ultra-high vacuum system with a background pressure of ~10^{-10} Torr equipped with XR50M X-ray Source, Focus 500 monochromator and Phoibos 100 analyzer by Specs GmbH. The photoelectrons were generated by a monochromatic source; Al Kα primary radiation (power set to 400 Ws). In order to overcome the charging effects, a flood gun was used with 30 μA current for all spectrum. The pass energy was set to 25 eV with an energy step width of 0.05 meV and a dwell time of 0.1 ms. The resultant spectrum for each sample was the average of five scans. The energy resolution of the equipment is found to be 0.89 eV (full width half maximum of Ag $3d_{5/2}$ peak).

The peak positions for Co 2p were found by a deconvolution process using Doniach-Sunjic (DS) asymmetric behavior due to the unfilled one-electron levels (conduction electrons). All peak positions for the catalyst layer samples were repositioned with respect to C 1s peak at 284.4 eV even; the flood gun was used to eliminate the charge accumulation. Quantification for the atomic concentrations was performed by fitting Co 2p and Al 2p peaks using Gaussian-Lorentizan (GL) behavior with corresponding Scofield factors; 12.6 for Co $2p_{3/2}$ and 0.356 for Al $2p_{3/2}$. Moreover, Gaussian-Lorentizian fitting was used for the deconvolution of Li 1s and C 1s peaks in the Li intercalation study.

3.2.6 Contact angle measurement

The dynamic contact angle measurements were conducted on the synthesized VA-CNTs using the contact angle instrument (Dataphysics OCA 15 Plus). Water was used as the liquid for the wettability properties. 8 μL amount of water was dropped on the surfaces of VA-CNTs by the help of an automatic syringe. Contact angle values reported in this work were averaged using three consecutive measurements.

Chapter 4

Results and Discussion

The study presented here has two main purposes; first one is investigating the growth mechanism of VA-CNTs and second is applying them as biomaterials and energy materials. The number of studies published on the effect of synthesis parameters show that there is not an accurate description of effect of growth parameter for the synthesis of CNTs. Every growth method has its own optimum parameter set for having the VA-CNTs with desired properties. The future application fields for CNTs would require more controlled growth of VA-CNTs having higher densities and desired surface properties. Hence, it is of great importance to investigate the effect of growth parameters and kinetics of VA-CNTs. On the basis of this, the effect of growth parameters on the synthesis of VA-CNTs will be discussed in the first part. Mainly, the diffusion and/or catalyst deactivation processes govern the acceleration or deceleration of CNT growth. Thus, in order to probe the mechanisms dominating the growth termination of VA-CNTs an attempt has been made.

In the second part of this thesis, the applications of VA-CNTs will be discussed. The synthesized VA-CNTs were used as scaffolds for stem cell seeding. The aim of this study was to speed up the growth of stem cells on the CNT templates. As another study for functionalization of VA-CNTs, the intercalation of Li inside the CNTs was studied to enhance the performance of carbonaceous anode materials.

4.1 Growth of vertically aligned carbon nanotubes

4.1.1 Optimization of catalyst design

In the literature, numerous different ways of catalyst designs were encountered for the synthesis of VA-CNTs. However, each catalyst configuration is unique for different synthesis technique and condition. Thus, in this study, the main aim is to uncover the optimum catalyst configuration resulting in the growth of VA-CNTs with desired properties by using the ACCVD method. The starting point for the optimum catalyst configuration is chosen as the simplest and most common one; a catalyst layer on the top of a buffer layer which is also designated as normal catalyst design.

The buffer (support) layer deposition plays a key role in the growth of CNTs (*63*, *116–118*). One of the important effects of the buffer layer is to inhibit the diffusion of catalyst particles to substrate. The characteristics of CNTs such as adhesion to a substrate and density could be manipulated by varying the morphology and chemical structure of support layer. For instance, it was reported that powdered catalyst and support did not result in a dense CNT growth while well dispersed and continuous thin layers of catalyst on a buffer layer initiated the growth of VA-CNTs (*63*).

First, a comparative study on the barrier effect of support layer was conducted using Fe as a catalyst layer. A Fe layer of 1 nm thickness was deposited on a 30 nm thick SiO_2 wafer using an e-beam (I) evaporation method. Then, the prepared catalyst layer (1 nm Fe/SiO_2) was subjected to the annealing and growth processes at temperature of 625 ^{0}C inside the ACCVD furnace. The SEM image of the 1nm Fe/SiO_2 sample revealed the growth of randomly scattered CNTs on the surface which was far from the main aim of having dense and aligned CNTs (Figure 19a). Hence as a next step, a 10 nm thick Al layer was placed beneath a 1 nm thick Fe catalyst layer (1 nm Fe/10 nm Al) to enhance the density of CNTs. This catalyst layer was subjected to ACCVD processes in same manner with the 1nm Fe/SiO_2 sample. As a result, CNTs were comparatively denser but still no alignment was achieved (Figure 19b).

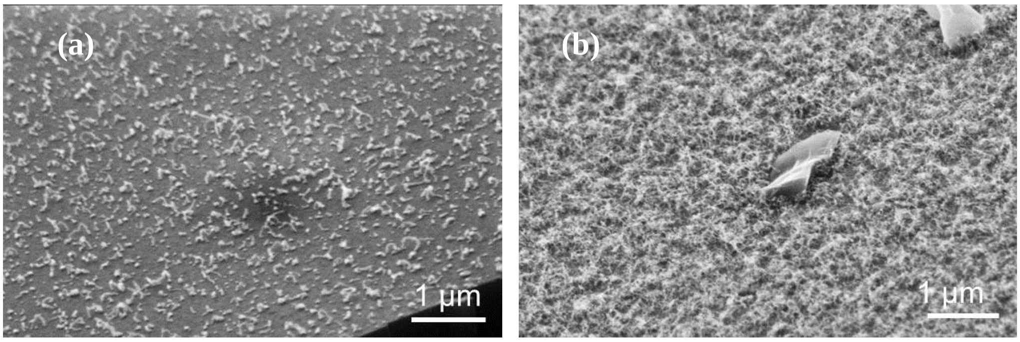

Figure 19. SEM image of CNTs grown on (a) 1nm Fe/SiO_2 and (b) 1nm Fe/10 nm Al layers at temperature of 625 ^{0}C.

In this study, CNTs synthesized on Si substrates without support layers were lacking alignment although there were studies in the literature reporting the growth of CNTs on Si wafers without having support layers (*119–122*). In some of these studies, a thick catalyst layer was used to overcome a mass decrease of catalyst due to a diffusion through a substrate (*121*, *122*). To investigate the effect of support layer, the diffusivity coefficient (D_c) of Fe in Al and Si layers were calculated following the Arrhenius equation (Eq. 1). It was found that the D_c value of Fe/Al sample ($\sim 10^{-10}$ cm^2/s) is less than the Fe/SiO_2 sample's ($\sim 10^{-8}$ cm^2/s) which was similar to the previous report by Lee *et al.* (*118*). This indicates that the presence of support layer hinders the diffusion of catalyst particles into a substrate and hence almost all the catalyst islands stay on the surface during thermal processes. Thus, this may explain the observation of denser CNT formation on the 1 nm Fe/10 nm Al catalyst configuration compared to the 1 nm Fe/SiO_2 in this study.

$$D_c = D_0 \exp\left(\frac{E_a}{kT}\right) \qquad (1)$$

As mentioned in Chapter 2, controlling alignment of CNTs has a vital role for further possible applications. In the initial experiments, the growth of denser CNTs on a Fe catalyst layer with the presence of Al was observed but still the alignment was not achieved (Figure 20a). When cobalt (Co) was used as the catalyst layer alternative to Fe (1nm Co/10nm Al) and subjected to the ACCVD processes at 625°C in a same manner, 10 μm tall VA-CNTs were successfully synthesized (Figure 20b). SEM images show that Co catalyst layer has higher activity than Fe layer for synthesis of VA-CNTs (Figure 20). A survey of literature on the comparative performance of different catalysts indicates that the activity of a catalyst layer strongly depends on the type of carbon source used for the growth. In these studies, it was reported that Co has higher activity with alcohol based carbon sources while Fe is more active with hydrocarbon sources such as ethylene or acetylene (*94*, *123*). However, the activity should not only be counted as an ability of catalyst to decompose a carbon source, it is also meaning to an ability to solve carbon and to diffuse into the catalyst.

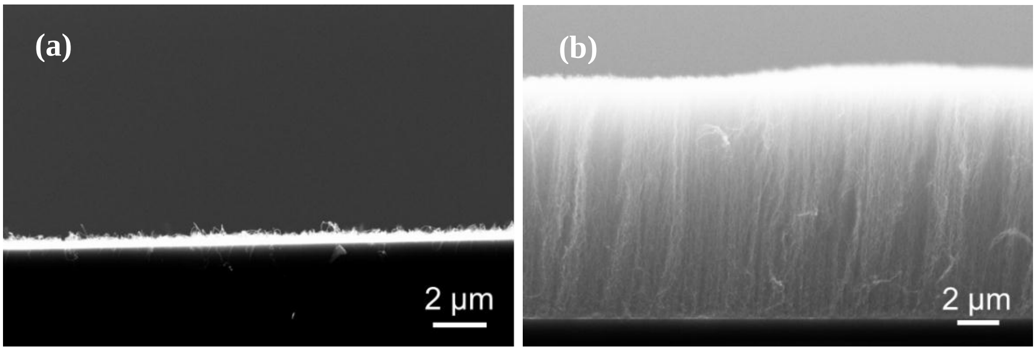

Figure 20. Side view SEM images showing the alignment of CNTs grown on (a) 1nm Fe/10nm Al and (b) 1nm Co/10nm Al catalyst layers.

The first action of a catalyst is to absorb the molecules of carbon on its surface. During this interaction, electrons from carbon species are transferred to the catalyst which has non-filled 'd' orbital and the electronic structure of carbon species changes in a such manner that the dissociation of carbon source occurs. Therefore, the activity of a catalyst is relevant with its electronic configuration. This would give a reason why Fe is more active with unsaturated carbon sources (containing double or triple bonds) while Co is more efficient with saturated carbon sources (*31*, *124*). Other than the dissociation ability, the carbon solubility also has a profound effect on the activity of catalysts. After a carbon source molecule is decomposed on a catalyst surface, carbon atoms are diffused within the catalyst and a CNT growth starts by the precipitation of carbon. Therefore, the solubility of carbon on a catalyst should not be underestimated when the catalyst is evaluated for the activity to grow CNTs.

The annealing step (reduction step) has a vital role in promoting the formation of catalyst islands due to wetting behavior and surface energy of metals used in coating. During ACCVD process, there is a competing mechanism between subsurface diffusion and migration of catalyst particles on the surface (Figure 21). Small particles can diffuse into the support layer over time while others are mobile on the surface to form bigger particles which is called 'Ostwald ripening'. If particles on the surface became larger in size due to the ripening, there would be no possibility to produce denser and thinner VA-CNTs. In order to inhibit the diffusion of particles, a sandwich catalyst design has been developed to produce denser VA-CNTs. In this method, a second layer of non-transition and inactive metal, which is commonly Mo, Al or MgO, is deposited on a catalyst layer (*125–128*) and this second layer stabilizes catalyst particles on the surface by inhibiting their mobility. In the literature, there are studies reporting the enhanced catalytic activity of catalyst particles by using the sandwich catalyst design (*126*, *127*). The possible explanation for the enhancement was that the additives suppressed the formation of secondary phases of catalysts with the bottom layers which are known to be inactive for growing CNTs.

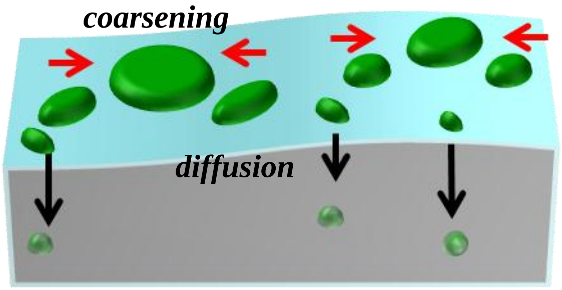

Figure 21. Schematic representation showing the subsurface diffusion and coarsening of catalyst particles on the buffer layer of Al during a heat treatment.

To enhance the density of VA-CNTs in this study, a second layer of Al was deposited on Co catalyst layer to inhibit the coarsening of Co particles and thus, the density of particles would be increased by pinning them on the buffer layer (0.5nm Al/1nm Co/10nm Al). Samples with the sandwich design (0.5nm Al/1nm Co/10nm Al) was subjected to the ACCVD steps at 625 °C in a same manner mentioned before. Figure 22a and b show SEM images of VA-CNTs grown on the 0.5nm Al/1nm Co/10nm Al and 1nm Co/10nm Al layers, respectively. It was observed that the length of VA-CNTs on sandwich design was higher than the CNTs grown on normal catalyst configuration. The reason for the shorter CNTs is the decrease in the activity of catalyst due to the subsurface diffusion. As shown in Figure 21, the subsurface diffusion of catalyst particles might lead to a decrease in the number of active particles because of mass loss. To provide a macroscopic proof for the subsurface diffusion in both catalyst designs, an analysis was performed on the H_2 - reduced and as-deposited catalyst layers using a surface sensitive technique; XPS. The atomic concentrations of Co and Al were estimated from XPS spectra for all samples (Appendix I). In the 1nm Co/10nm Al sample, it was found that there was a decrease in Co concentration from % 74 to % 11 induced by H_2-reduction step. For the 0.5nm Al/1nm Co/10nm Al sample, the decrease of Co concentration was from % 51 to % 38 which provided an evidence for the subsurface diffusion of Co. When the ratios of Co concentration decrease in samples before and after the reduction step were compared, it was found that the catalyst particles on the 1nm Co/10nm Al sample were diffused more than the particles on the 0.5nm Al/1nm Co/10nm Al sample. Regarding to these, it was suggested that the top Al layer pinned the particles by inhibiting their mobility.

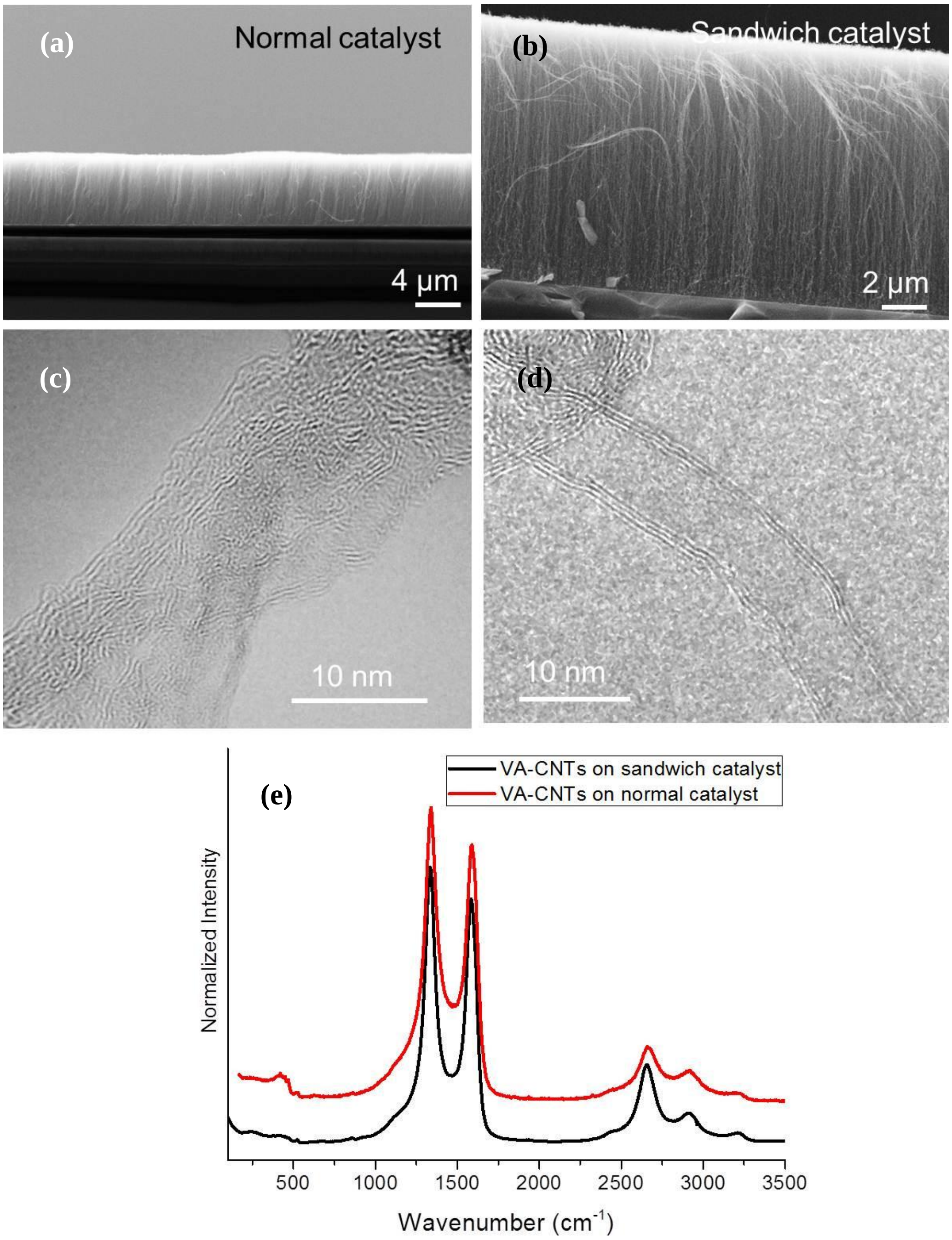

Figure 22. Side view SEM images of VA-CNTs grown on (a) normal and (b) sandwich catalyst configurations. HRTEM images of CNTs grown on (c) normal and (d) sandwich catalyst configurations. (e) Raman spectra of VA-CNTs grown on both catalyst configurations.

HRTEM images of CNTs grown on normal and sandwich catalyst designs indicated that CNTs had 2 or 3 side walls with an average diameter around 7 nm (Figure 22c and d). However, the graphitization of CNT sidewalls grown on the normal catalyst was less than the sidewalls of sandwich design sample.

The presence of top Al layer immobilized the catalyst particles on the surface and thus, the areal density of VA-CNTs (ρ) would be increased due to an increase in numbers of active particles on the surface. Recently, there are three ways to measure the density even none of them provides the exact value. The first method is counting CNTs in SEM or TEM which is less quantitative. Another one is based on the weight gain of substrate after the growth process and the last method is the liquid-induced compaction method (*129–132*). In order to compute the density increment of VA-CNTs by catalyst design, the liquid-induced compaction method was applied to VA-CNTs grown on the normal and sandwich catalyst configurations comparatively. In this method, VA-CNTs on the surfaces were soaked into deionized water and as a result of this; CNTs were compacted to a maximum density due to the wetting / drying process. The top view SEM images show the top surfaces of VA-CNTs grown on the normal and sandwich catalyst designs after the compaction process which help to estimate the filling fractions (F) (Figure 23a and b). The value of F is the areal ratio of compacted surface to total surface and is calculated using Image J software by masking the top of compacted areas (Appendix II) (*133*). The ρ value of CNTs is expressed with F and d where d is tube diameter determined by TEM images and δ is the theoretical Van der Waals tube distance (0.34 nm) (Eq. 2) (Appendix III) (*134*).

$$\rho = \frac{2\,F}{\sqrt{3}(d+\,\delta)^2} \qquad (2)$$

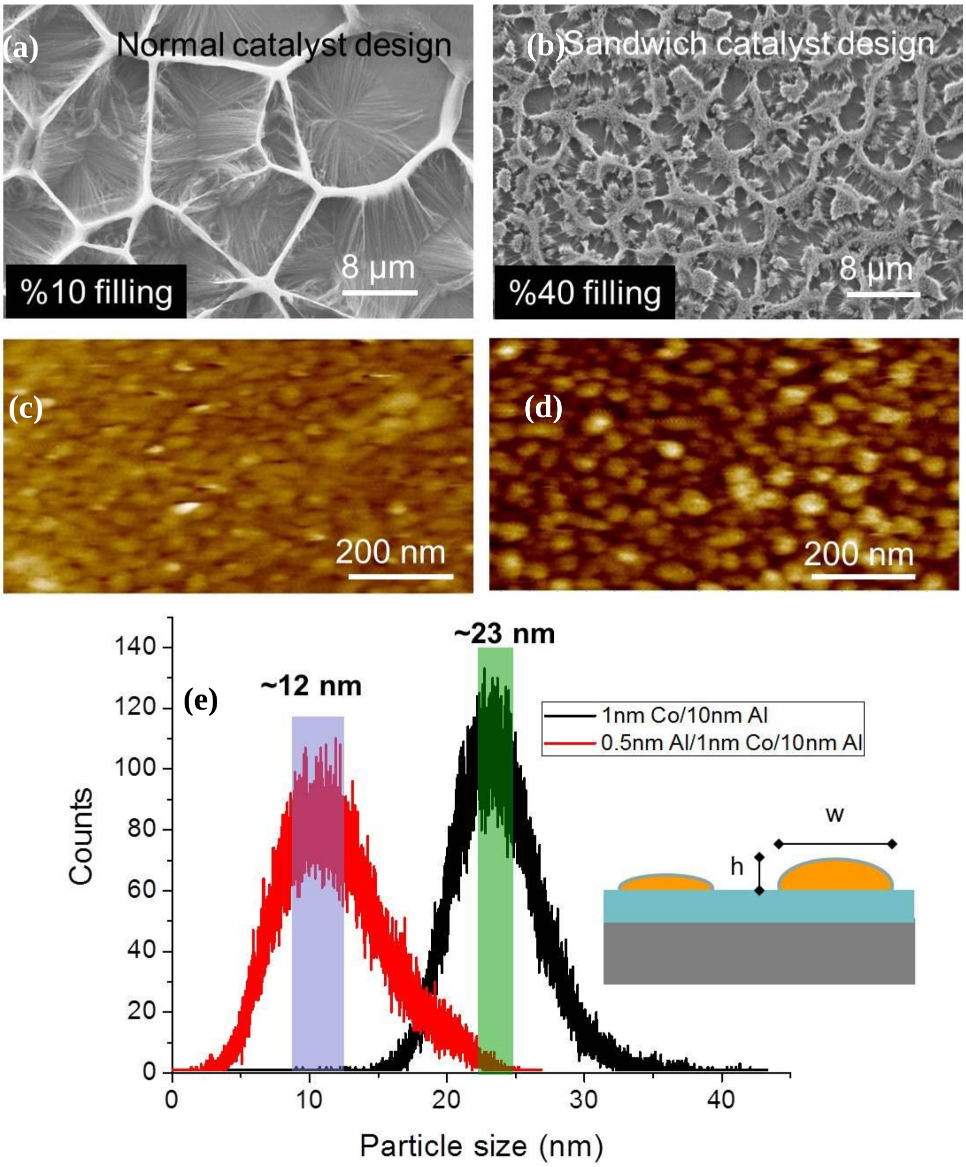

Figure 23. Top view SEM images of collapsed CNTs grown on (a) normal and (b) sandwich catalyst designs. 2D contact mode AFM images of (c) normal and (d) sandwich catalyst designs after reduction process. (e) Size distribution of particles on both catalyst designs after reduction process.

By using the equation, it was found that the density of VA-CNTs on the normal catalyst design was ~2×10^{-11} cm^{-2} while the sandwich catalyst design yielded ~9×10^{-11} cm^{-2} CNTs. Based on these values, it is suggested that the presence of top Al layer increased the density of CNTs. Furthermore, AFM analysis performed on the H_2-reduced 1nm Co/10nm Al (normal) and 0.5nm Al/1nm Co/10nm Al (sandwich) samples to find out a macroscopic evidence for the density increment of catalyst particles (Figure 23c and d, respectively). When 2D AFM images were processed for the particle size distribution (w), it was found that the average value of w for the particles in the sandwich catalyst design (~12nm) were smaller than the average value of w for the particles in the normal configuration (~23nm) (Figure 23e). This indicates that during the thermal annealing, the top Al layer immobilized the particles and hence inhibited the coarsening. In comparison, the average height value (h) of the particles was found to be 2 nm for the normal catalyst configuration while it was 5 nm for the sandwich catalyst configuration. The reason for thicker particles in the sandwich configuration is the presence of second Al layer on the top of catalyst layer.

Moreover, no CNT growth was observed when the thickness of top Al layer was increased from 0.5 nm to 1nm. The possible explanation is the full coverage of catalyst surface by comparatively thicker top Al layer and as a result no catalytic activity was observed.

Table 1 summarizes the properties of catalyst layers and VA-CNTs on both catalyst designs. Regarding to these, the role of top Al layer is found to be pinning catalyst particles on surface as shown in Figure 24. Furthermore, sandwich catalyst configuration (0.5nm Al/1nm Co/10nm Al) yielded denser and taller VA-CNTs comparatively. Thus, the optimum catalyst design in this study was the sandwich method where a second layer of Al was deposited on the catalyst layer (0.5nm Al/1nm Co/10nm Al).

Table 1. The properties of catalyst layers and VA-CNTs on normal and sandwich catalyst designs.

	Normal design	*Sandwich design*
Co/Al %at. before reduction	49	60
Co/Al %at. after reduction	16	47
Average w values (nm)	23	12
Length of VA-CNTs (µm)	4	10
% F	10	40
ρ *(cm*$^{-2}$*)*	2×10^{-11}	9×10^{-11}

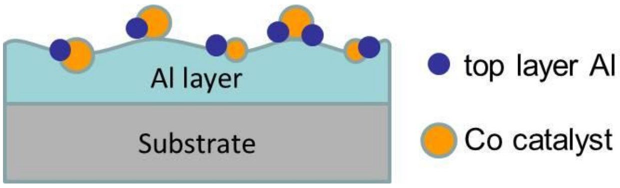

Figure 24. A representative drawing of a sandwich catalyst layer after the reduction process.

Motivated by the earlier studies in the literature, buffer layer thickness was varied to investigate its effect on growth of CNTs (*86–88, 135, 136*). As shown in Figure 25, well aligned CNTs were grown at 625 °C using ethanol as carbon source on 3, 5 or 7nm thick bottom Al layers having the sandwich catalyst design. The side view SEM image of VA-CNTs grown on the 0.5nm Al/1nm Co/10nm Al catalyst configuration was provided previously in Figure 22d. In order to better understand the height difference of VA-CNTs in respect to varying Al thickness, contact mode AFM analysis was performed on the reduced catalyst layers at 625 °C (Figure 25). The images indicated that the particle size were different for each thickness of Al layer. The values of *w* were calculated and it was found that the reduced catalyst particle size on a surface was widened as the thickness of bottom Al layer increased. Moreover, the length of VA-CNTs decreased as long as thicker Al buffer layer was used (Figure 25).

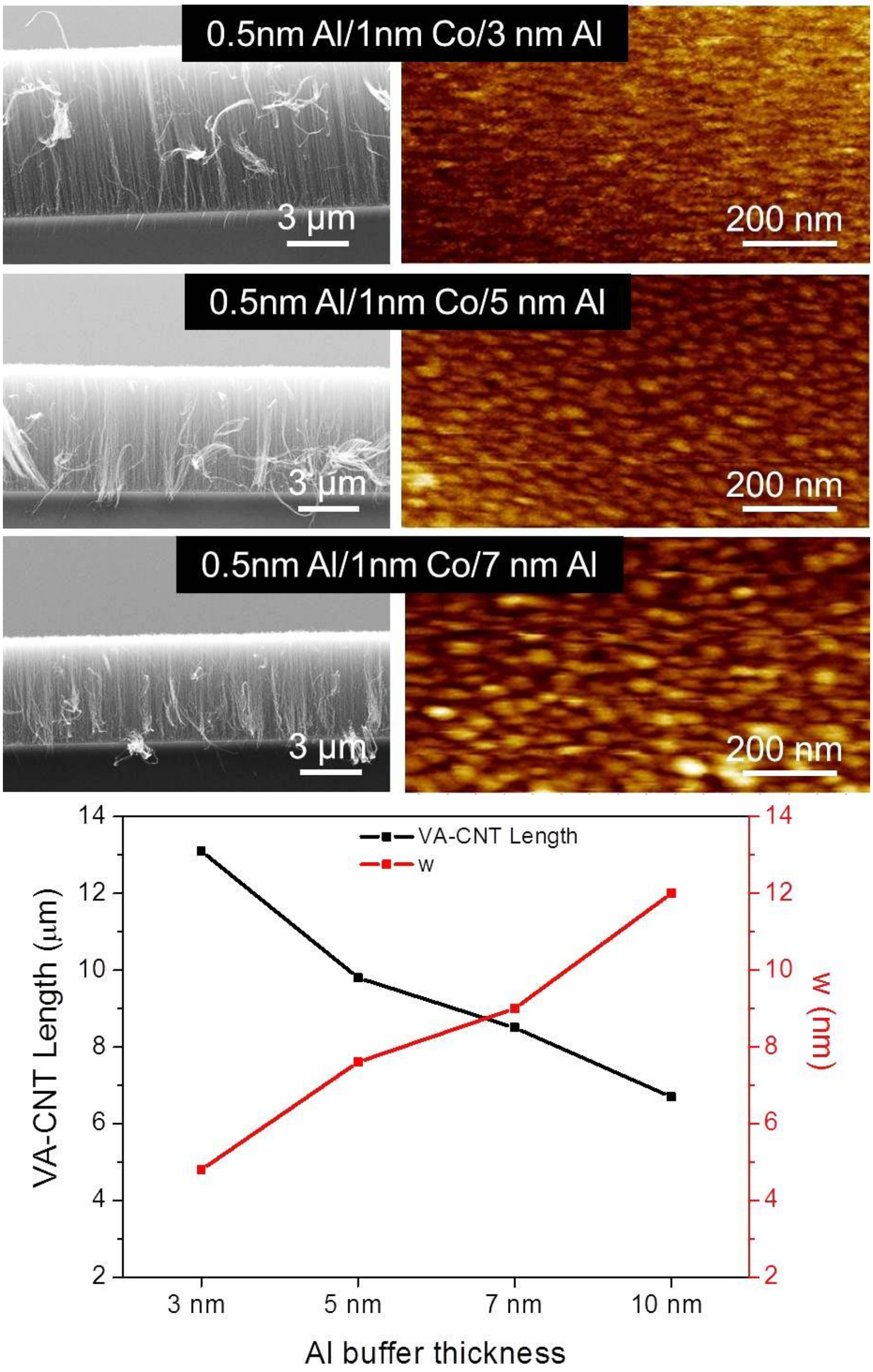

Figure 25. SEM images of VA-CNTs synthesized at 625 °C using sandwich catalyst design on varying thickness of bottom Al layer (3, 5, 7 and 10 nm). AFM images of H_2-reduced catalyst layers at 625 °C and the plot for the change of VA-CNT length and average particle size distribution (*w*) versus bottom Al layer thickness.

In the literature, thicker Al layers have represented more expansion of a layer which resulted in more porous structures. Thus, this porous morphology could contribute an increase in carbon adsorption (*87*, *136*). Regarding to this, a possible explanation of VA-CNT length decrease with respect to thicker Al layers is the high amount of carbon adsorption due to porous structure of thick Al layer and thus the growth rate of CNT could be retarded.

Even the high yield of CNT synthesis was not achieved by using 1nm Fe/10 nm Al catalyst layer, the sandwich catalyst design was also conducted using Fe to synthesize well aligned CNT arrays at 625 °C using ethanol as carbon source (0.5nm Al/1nm Fe/10nm Al). While Figure 26a shows SEM image of randomly scattered CNTs, HRTEM image points that Fe catalyst resulted in thicker CNTs compared with the CNTs synthesized using Co catalyst (Figure 26b). A comparison of HRTEM images of CNTs synthesized using Co (Figure 22d) and Fe (Figure 26b) catalysts indicates that type of catalyst has an important role in thickening CNTs.

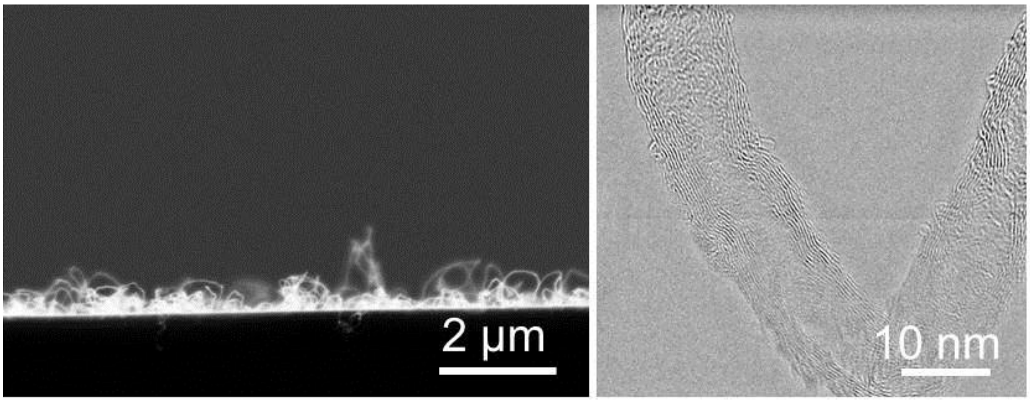

Figure 26. (a) SEM and (b) HRTEM images of CNTs synthesized at 625 °C on the 0.5nm Al/1nm Fe/10nm Al catalyst configuration.

4.1.2 Optimization of annealing step

In the previous section, it was found that denser and oriented CNTs were grown on Co catalyst layer which had sandwich design. But the catalyst design is not the only factor affecting the density and orientation of CNTs as well as the nucleation of catalyst particles. The pretreatment parameters such as time and temperature also have a critical effect on the growth of CNTs. Several researchers have reported various methods for an annealing process to increase the growth yield of CNTs by using gas-assisted processes (*38*, *137–140*).

The majority of the research has been focused on gaining control over the growth of VA-CNTs. Thus, a study has been performed on the sandwich catalyst layers to better understand the effect of reduction step on the growth of VA-CNTs. The catalyst layers having 0.5nm Al/1nm Co/10nm Al configuration have been reduced at 625 °C and 4 Torr pressure under Ar/H_2 atmosphere for 5, 10, 15, 20, 30 and 60 minutes. Then in a same manner, all of them were subjected to the growth step at 625 °C using ethanol as a carbon source for 30 minutes. As shown in SEM images (Figure 27a-g), it was found that randomly scattered CNTs were only grown on non-reduced catalyst layer while well-ordered VA-CNTs were synthesized on reduced layers. The plot in Figure 27h shows how the length of VA-CNTs changes with respect to reduction time. The plot points a decrease in the growth rate of CNTs as the reduction process time was prolonged. The optimum reduction time for the highest VA-CNT growth was found to be 15 minutes at the growth temperature of 625 °C. A possible explanation of the decrease in the growth is the depressed catalytic activity since catalyst diffuses more as the reduction process is prolonged. To better understand the effect of time on the catalyst restructuring, SEM analysis were done on as-deposited and H_2-reduced sandwich catalyst films for 15 and 60 minutes (Figure 28). SEM images clearly indicate that deposited film is a discontinuous thin layer due to the Volmer-Weber film nucleation (*141*) and no active islands were formed without the reduction process (Figure 28a). Moreover, a comparison of SEM images of 15 minutes and 60 minutes reduced catalyst layers indicates that catalyst particle sizes are getting bigger as the process time prolongs. All these suggest that islands are coarsening and diffusing more at longer thermal processes and hence 15 minute reduction at temperature of 625 °C is the optimum window for longer VA-CNT growth.

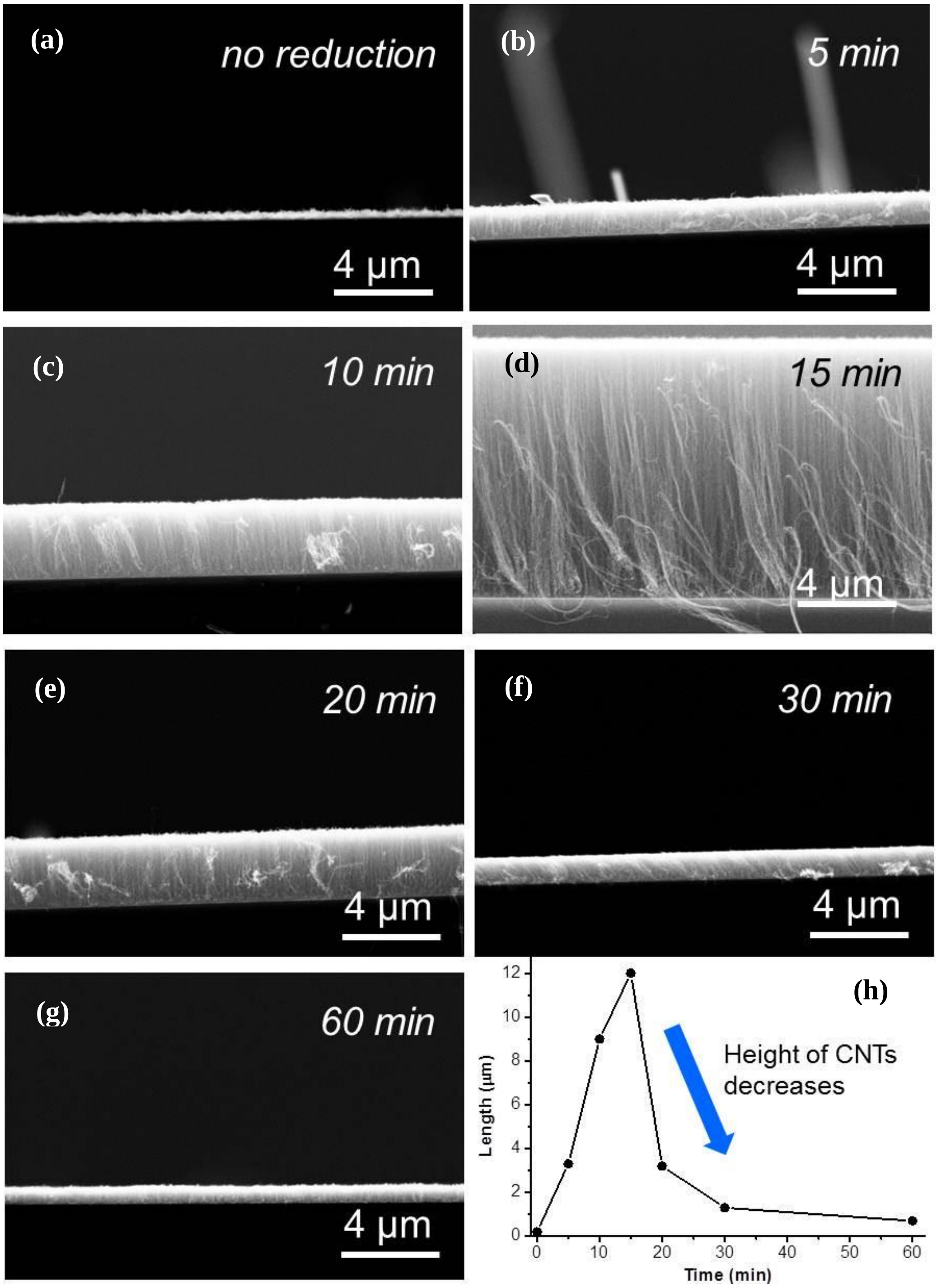

Figure 27. (a-h) SEM images of VA-CNTs grown on the non-reduced and H_2-reduced sandwich catalyst layers at 625 °C for 5,10, 15, 20, 30 and 60 minutes, respectively. (h) The plot shows changes in the length of VA-CNTs by reduction time.

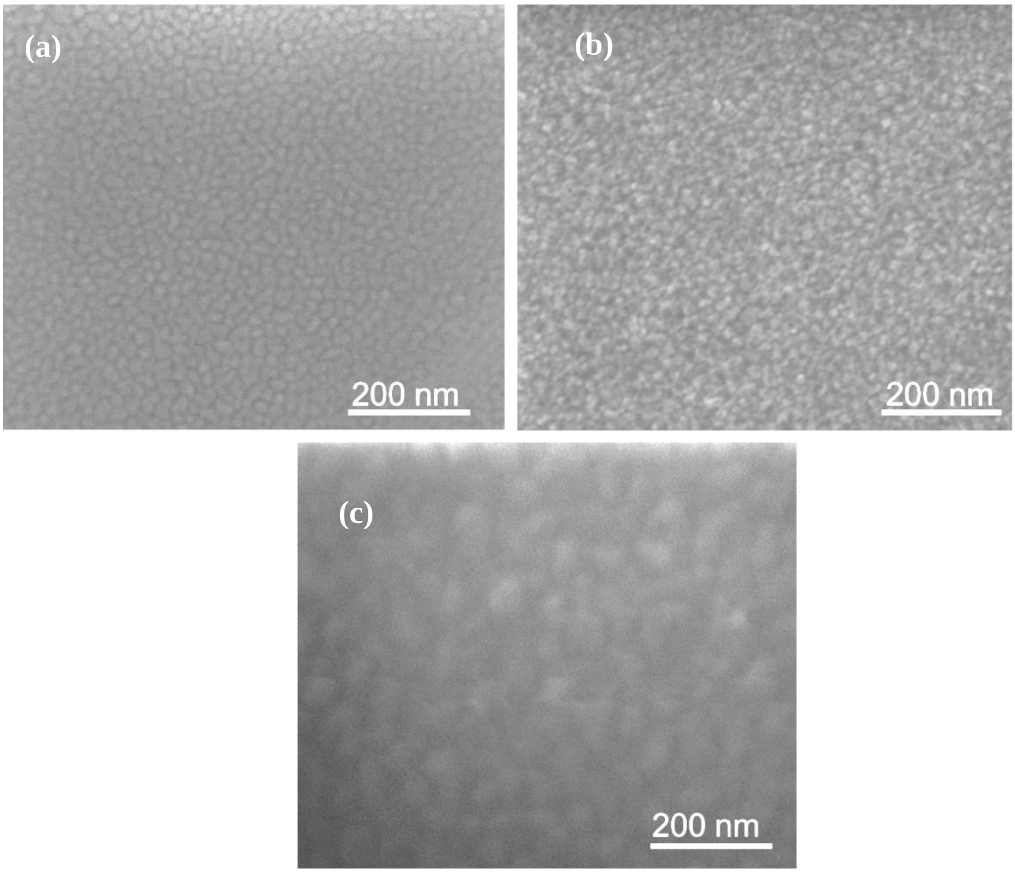

Figure 28. Top view SEM images of (a) as-deposited and H_2-reduced at 625 °C for (b) 15 minutes and (c) 60 minutes sandwich catalyst layers.

To find out the catalyst state, XPS analysis has been cemployed on the catalyst layers before and after the H_2-reduction process at 625 °C for 15 minutes. In this part, two different types of catalyst layer were used to better understand the effect of air exposure. First type was the typical sandwich configuration (0.5nmAl/1nmCo/10nmAl) deposited using e-beam evaporation (I) technique and it was identified as “1nm Co●” in Figure 29. The second type layer was 1nm Co/10nm Al configuration deposited using EBE-4 (II) evaporation system which was already mounted in the XPS instrument. This type catalyst layer was designated as “1nm Co*” in Figure 29. 1nm Co● layer before reduction process (as-is) had Co $2p_{3/2}$ peak at 781.1 eV with a small shoulder at lower binding energy while Co $2p_{1/2}$ peak appeared at 797 eV (Figure 29a and Table 2). Moreover, a broad shake-up satellite (designated with s letter in Figure 29), which is the characteristic sign of oxidized Co, was observed for the as-is form of 1nm Co● layer. In the literature, it was reported that shake-up satellite peak at 5 eV higher than its main peak and a spin-orbit coupling of around 15.5 eV indicated the formation of CoO (Co in the form of +2 valency) (*142*, *143*). The catalyst layers deposited using e-beam evaporation (I) technique (1nm Co●) were have to be exposed to air before transferred to the XPS chamber. Hence, it was not surprising to observe the oxidized form of Co beside the presence of metallic Co which was indicated by a small peak around 778 eV (*144*). As shown in Figure 28a, the catalyst layers are inhomogeneous on the surface and this provides more surface area for air oxidation in contrast to thick layers. Even the reduction process has been performed on the 1nm Co● sample, there was almost no shift at the position of peaks; still Co was in the form of oxide (Figure 29b). This would be explained by the ACCVD design, where the reduction has been performed, is not connected to the XPS chamber directly. Hence, the reduced sample was exposed to air while it was being transferred to the XPS chamber and resulted in the formation of oxide on the Co layer. In the case of air exposed thick layer of Co (40nm Co●), both metallic and oxide Co $2p_{3/2}$ peaks appeared at 777.9 eV and 780.2 eV, respectively (Figure 29c). This indicated that some oxidation occurred only on the top few layers of thick Co and underneath top few layers, Co still remained metallic.

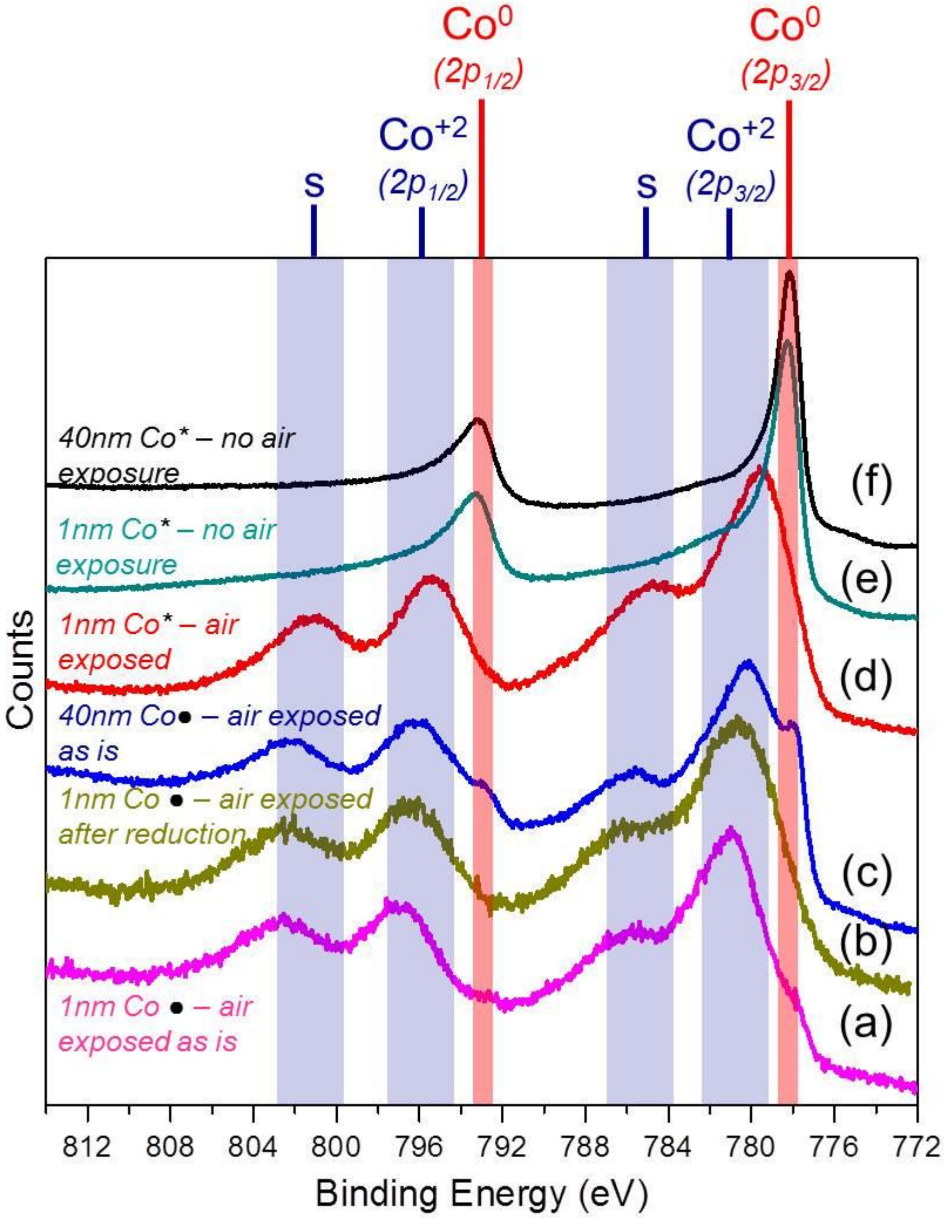

Figure 29. (a-f) XPS spectra of Co 2p regions for various Co layers (● and *, respectively, indicate that Co layers are prepared using e-beam (I) and EBE-4 (II) evaporation systems).

To better understand the chemical state of catalyst after the deposition, a second set of deposition had been performed using EBE-4 technique (II) where the deposition chamber is connected to the XPS analysis chamber and hence samples after the deposition process were not exposed to air. When a comparison was done between XPS spectra of samples 1nm Co* air exposed (Figure 29d) and 1nm Co* no air exposure (Figure 29e), it is clear that there was a shift towards higher binding energy indicating the oxidation of metallic Co by air exposure. Moreover, the shake-up satellite peak (s) around 785 eV pointed the presence of oxides on the 1nm Co* air exposed sample. XPS spectra of thick Co layer (40nm Co*) deposited using EBE-4 (II) shows clear metallic Co 2p peaks at 778.2 eV and 793.2 eV contrary to the air exposed 40nm Co● sample. As a conclusion, it is clear that all catalyst surfaces either deposited using e-beam (I) or EBE-4 (II) instruments were in form of CoO when exposed to air even after the reduction process. Thus, an in-situ system is required to figure out the interaction between Co and Al during the reduction process.

Table 2. Tabulation of binding energies of Co 2p peaks for different catalyst configurations indicating the catalyst state before and after the reduction step.

	Binding energy (eV)	
	Co 2p$_{3/2}$	*Co 2p$_{1/2}$*
(a) 1nm Co● before reduction (as is)	781.1	797
(b) 1nm Co● after reduction	780.6	796.5
(c) 40 nm Co● before reduction (as is)	777.9 / 780.2	793 / 796
(d) 1nm Co before reduction (air exposed)*	779.7	795.5
(e) 1nm Co before reduction (no air exposure)*	778.3	793.3
(f) 40 nm Co before reduction (no air exposure)*	778.2	793.2

4.1.3 Effect of growth parameters

In this section, growth process parameters such as temperature, carbon source type and pressure were investigated. Firstly, the effect of carbon source type under two different growth temperatures was investigated. The sandwich catalyst design (0.5nm Al/1nm Co/10nm Al) was applied for the synthesis of VA-CNTs using ethanol, acetone and isopropanol as carbon sources under a flowing atmosphere of 100 sccm Ar and 20 sccm H_2 at 625 ^{0}C or 750 ^{0}C for 30 minutes. The reduction step for these experiments was conducted in a same manner discussed before at relevant temperatures, 625 ^{0}C or 750 ^{0}C.

Figure 30 shows the SEM images of synthesized VA-CNTs at temperature of 625 ^{0}C using ethanol, acetone and isopropanol as carbon sources. There was no apparent difference in length of VA-CNTs synthesized using different carbon sources and they were at average height of 6 μm. However, the difference in the alignment of CNTs was distinguishable. VA-CNTs synthesized using ethanol and isopropanol were well aligned while it was curly and entangled when acetone was used.

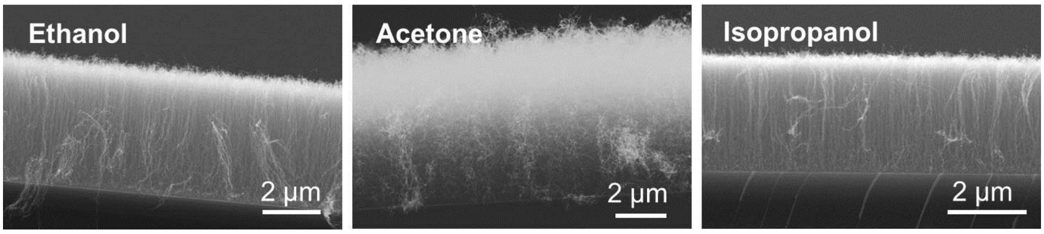

Figure 30. SEM images of VA-CNTs synthesized at 625 °C using ethanol, acetone and isopropanol as carbon sources.

SEM was not the only technique to characterize VA-CNTs. Raman spectroscopy was also conducted to investigate the effect of carbon source type on crystallinity and defectiveness of CNTs. As mentioned before, CNTs have two characteristics peaks; D and G bands appear around 1340 cm^{-1} and 1595 cm^{-1}, respectively and second order 2D band is the overtone of D band frequency. While intensity ratio of G to D bands (I(G/D)) provides a measure for the defectiveness of sample, intensity ratio of 2D to G bands (I(2D/G)) points out the amount of side wall crystallinity of CNTs. If I(G/D) value is high, it means that CNTs are comparatively less defective. When I(2D/G) value is comparatively higher, it indicates that CNTs are better crystallized. Raman spectra of VA-CNTs grown at 625 °C using varying carbon source was provided in Figure 31a. Furthermore, the values of I(G/D) and I(2D/G) of VA-CNTs grown using acetone were the highest one when compared to others (Figure 31b). This indicated that VA-CNTs grown using acetone had less defective structure and less amount of amorphous carbon while they were having well crystalline sidewalls. It is well known that acetone is ketone and has one unsaturated double bond with oxygen (C=O) which has different chemical structure when compared to alcohols. Furthermore, lower formation enthalpy of acetone (ΔH_f ~ -247 kJ/mol at 880 K) points that the decomposition of acetone would be easy to occur compared to other carbon sources. However, a carbon atom in the C=O group does not participate in formation of CNT (*84*). This carbon atom involves in formation of CO molecule. Hence, fewer amounts of carbon molecules involves in the growth of VA-CNTs and this would be responsible for less amorphous carbon presence and better crystalline structure of CNTs. But still, alignment is an issue for synthesis of CNTs when acetone is used as a liquid carbon source.

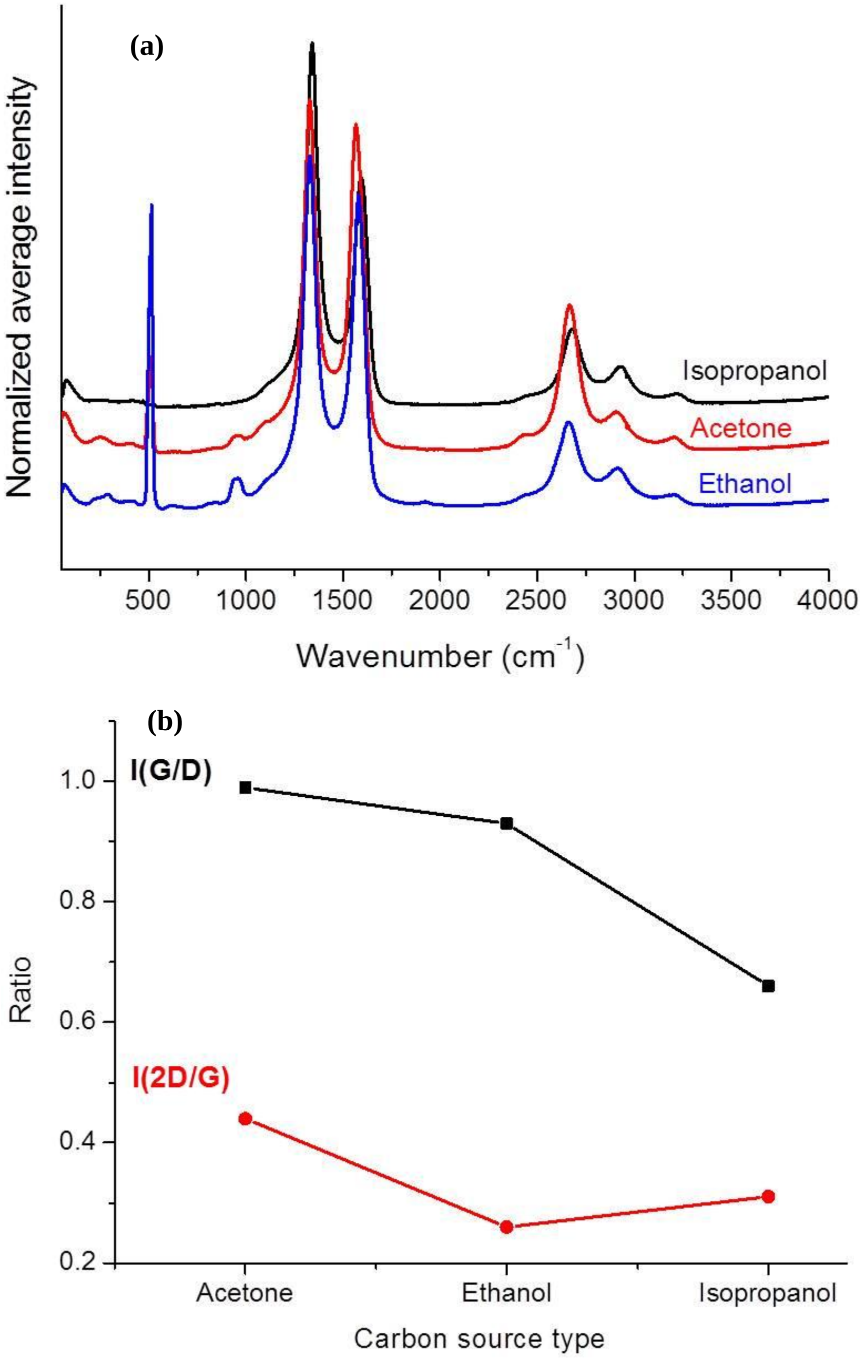

Figure 31. (a) Raman spectra of VA-CNTs grown at 625 °C using acetone, ethanol and isopropanol as carbon sources. (b) The plot for I(G/D) and I(2D/G) ratios of VA-CNTs versus carbon sources.

The alignment of VA-CNTs was achieved at 625 °C in case of ethanol and isopropanol usage where both sources have one bonded OH groups (Figure 30). However, it was found that ethanol as carbon source resulted in less defective CNTs (Figure 31b). In use of alcohols as carbon sources, OH group acts as etchant and protects the surface of catalyst from poisoning. Excess carbon is not the only species being etched by OH groups but also grown CNTs would be etched. For that reason, in case of alcohol use CNTs would have more defect comparatively and as a consequence they would have lower I(G/D) ratio. Regarding to this, it was reasonable that VA-CNTs synthesized using alcohol sources resulted in relatively higher defect density. When ethanol and isopropanol cases were examined, ethanol case resulted in lower defect density in the CNTs which is most probably due to a smaller ratio of C/OH for ethanol. Moreover, a lower formation enthalpy of ethanol compared to isopropanol favors ethanol decomposition more easily (*82, 84*).

Beside the lower growth temperature, VA-CNTs were also synthesized at 750 °C using ethanol, acetone and isopropanol in same manner described above. In Figure 32, SEM images of VA-CNTs show that there was a significant increase in length of CNTs when acetone was used. It was the ‘tallest’ VA-CNTs ever synthesized in this study with almost 200 μm in length. Although, CNTs seemed well aligned at low magnification images for the acetone case, they were curlier compared to others at higher magnified images.

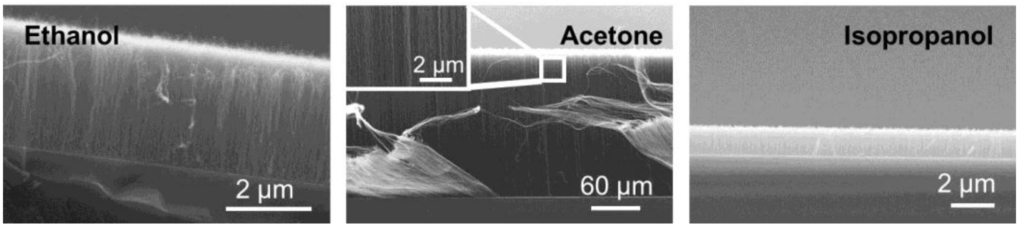

Figure 32. SEM images of VA-CNTs synthesized at 750 °C using ethanol, acetone and isopropanol as a carbon source.

Raman spectra of VA-CNTs synthesized at high growth temperature, 750 °C, was shown in Figure 33a. D and G bands were almost at similar wavenumbers for each carbon source. However, RBM mode only appeared at 220 cm^{-1} and 240 cm^{-1} for VA-CNTs synthesized using ethanol and this indicated the presence of SWCNTs in major amount of MWCNTs. The highest I(G/D) ratio value was found for the ethanol case which indicated the lower defect density in VA-CNTs as shown in Figure 33b. Hence, it was found that at higher growth temperature, ethanol resulted in better quality of CNT arrays. In the case of acetone, the tallest arrays were observed for this study and this might lead more amorphous carbon presence in the sample grown at 750 °C which resulted in a lower I(G/D) ratio compared to the case at 625 °C.

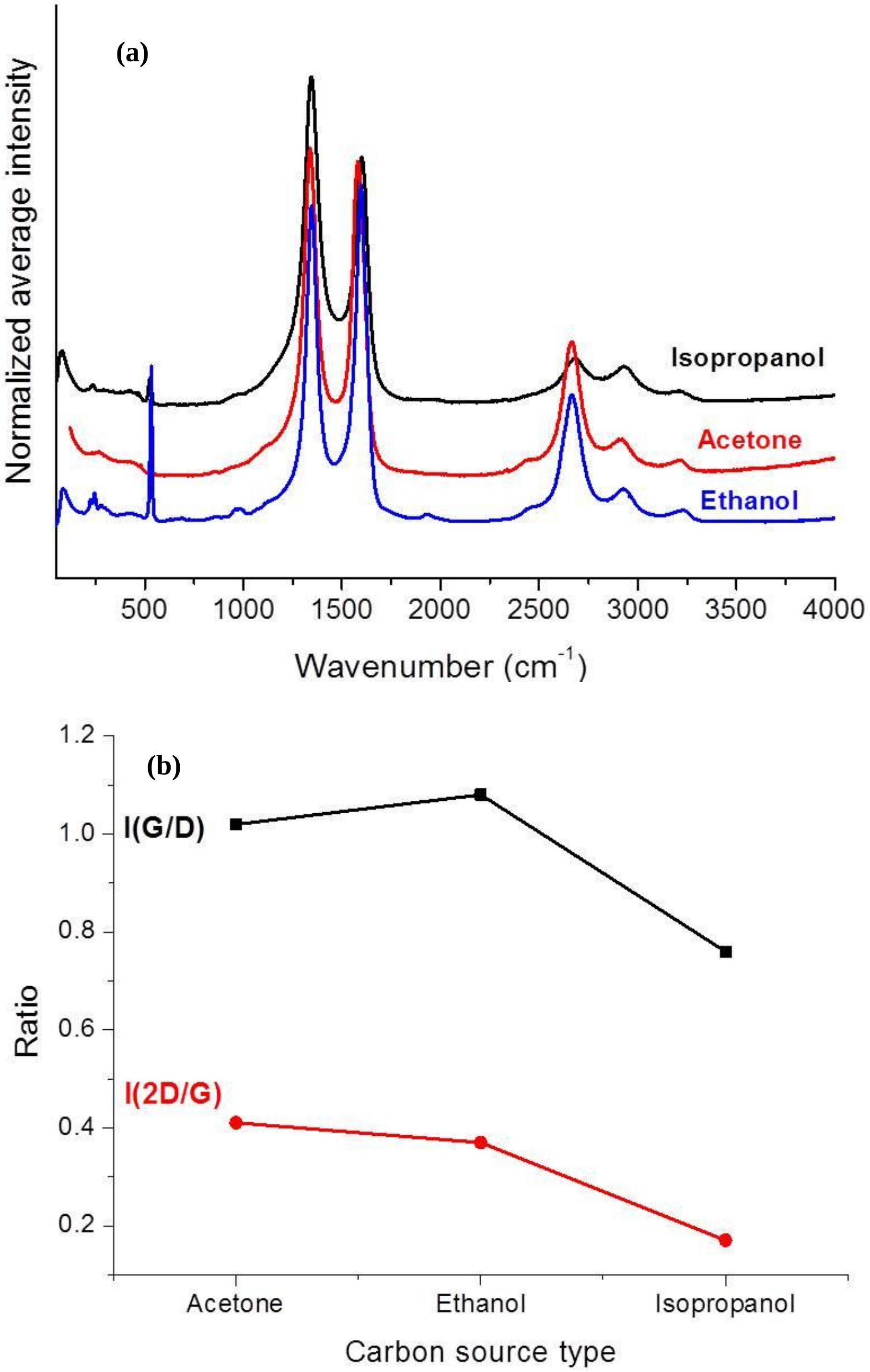

Figure 33. (a) Raman spectra of VA-CNTs grown at 750 °C using acetone, ethanol and isopropanol. (b) The plot for I(G/D) and I(2D/G) ratios of VA-CNTs versus carbon sources.

A representative TEM analysis of CNTs synthesized using ethanol as carbon source showed that CNTs grown at 625 °C had mostly 3 to 5 walls while they were 2 to 3 walled in case of relatively high growth temperature, 750 °C (Figure 34). It was clearly seen that amorphous carbon was present on the sidewalls of CNTs grown at higher synthesis temperature (shown by white arrows at Figure 34b). Thus, it was reasonable to have high intensity for the D band in Raman spectrum of CNTs from ethanol at higher temperature (Figure 33). An explanation for the presence of amorphous carbon might be the increased etching activity of OH radicals by an increase in growth temperature (750 °C). Therefore, the sidewalls of a CNT were combusted and amorphous carbon accumulated on the sidewalls. Also, few SWCNTs were observed in this sample which was coherent with results of Raman spectrum indicating the RBM modes (Figure 33a). From the morphology view, CNTs were less straight at low growth temperature (625 °C) which might be due to low arrangement energy for carbon atoms coming in.

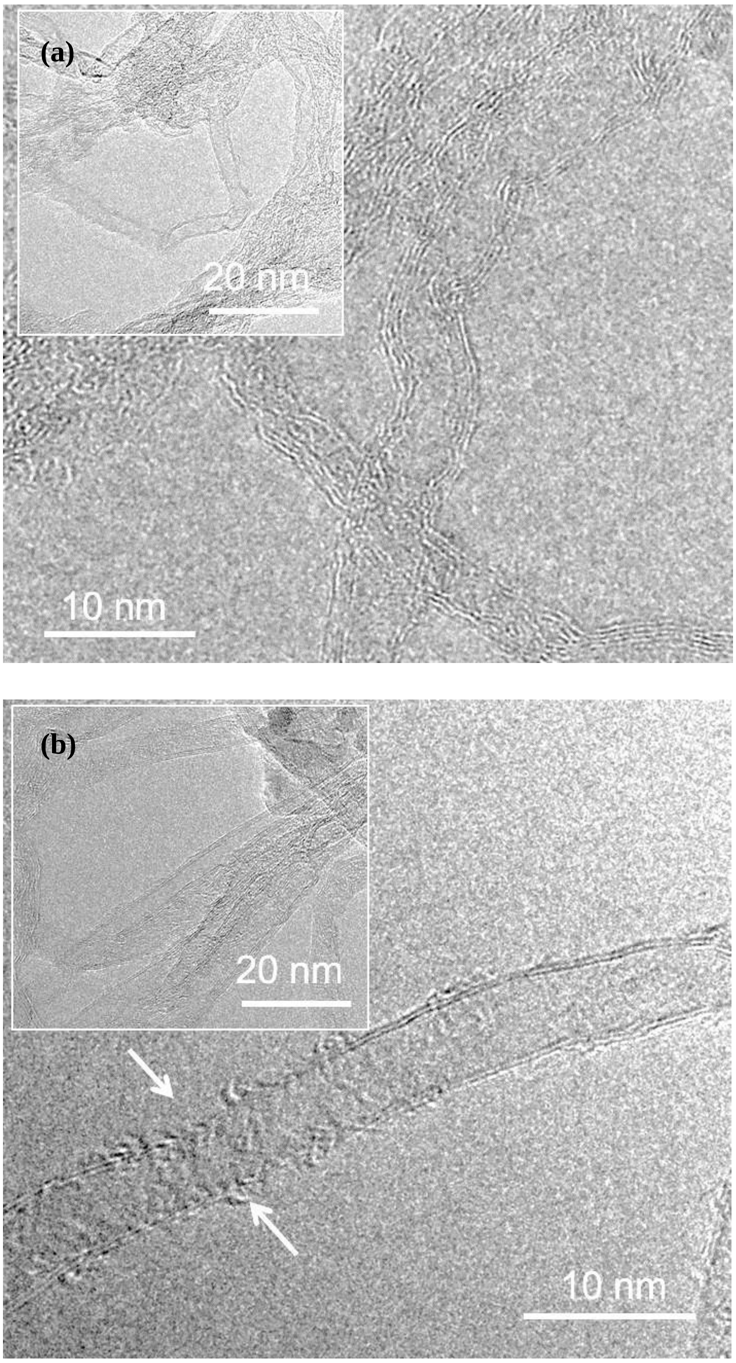

Figure 34. TEM images of VA-CNTs synthesized at temperatures of (a) 625 °C and (b) 750 °C using ethanol as carbon source. White arrows show the amorphous carbon presence on the side wall of a CNT.

Other than alcohols and ketones, aromatic hydrocarbon derivatives; benzene and toluene, were also used to synthesize CNTs on the sandwich layered catalysts. Figure 35 shows the SEM images after the growth step at 625 °C. It was found that the density of CNTs was low and CNTs were randomly scattered on the surfaces (Figure 35). In the literature, aromatic hydrocarbon precursors were studied and proposed as a good candidate for synthesis of CNTs at growth temperatures between 600 and 1000 °C (*35*, *83*, *145*). It was reported that growth of CNTs using aromatic hydrocarbon sources follows the six-membered-ring-based model which was reported by Tian *et al.* (*145*). According to this model, first benzene ring sticks on a catalyst surface and then C–H bonds are broken to incorporate into graphene layers via surface diffusion to form a CNT (*145*). Contrary to the common reports, it was observed almost no CNT for the benzene case while less amount of CNTs were present in the toluene used sample in this work. A possible explanation for these results might be the overfeeding of carbon source resulted in coating of all catalyst surfaces and subsequently deactivation of catalyst occurred (*31*).

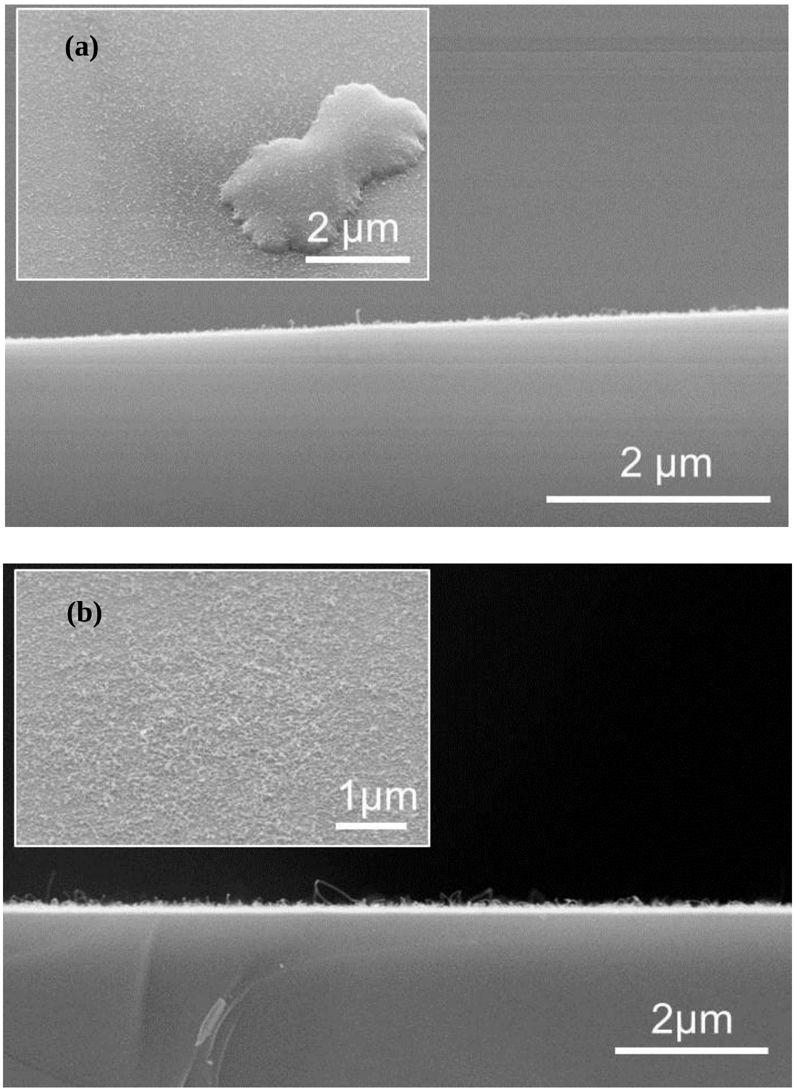

Figure 35. CNT surfaces after the growth step at 625 °C using (a) benzene and (b) toluene as carbon sources.

As a summary, it was found that alcohols and ketones would be a good candidate for the synthesis of well aligned and denser CNTs while aromatic hydrocarbons were not sufficient under these ACCVD growth conditions. Raman and SEM analysis showed that VA-CNTs synthesized using alcohols and ketones had different heights and structural properties. For a further step in characterizing the properties of VA-CNTs, dynamic contact angle measurements were employed in order to investigate the wettability properties of surfaces (Figure 36). In the literature, the numerous studies have been reported on the wettability of carbon films where mostly VA-CNTs have been declared as a hydrophobic surface without doing any modification (*146–150*). There are several agents that influence the surface energy and hence the surface wettability as well. These are chemical modification, roughness and relative presence of sp_2-sp_3 bonds (*147*, *151*, *152*). In this study, it was found that VA-CNTs synthesized at 625 °C using ethanol presented hydrophobic (contact angle ~ 150°) surface and the wettability did not change drastically by time which is consistent with previous reports (*148*, *153*). The decrease in size of water droplet on the surfaces by time was mainly due to the evaporation (Figure 36). In contrary, VA-CNTs grown at 750 °C using ethanol had super-hydrophobic (contact angle ~ 180°) surfaces at least for 20 minutes. The trend in the contact angle plots (Figure 36a and b) were determined in the same behavior with the graphs of I(G/D) ratio which also provided an information for impurities (Figure 31b and Figure 33b). This emphasized that the presence of amorphous carbon on the surface or between CNT arrays resulted in shifting the wettability properties of VA-CNTs from super-hydrophobic to hydrophobic properties. Moreover, the consequences of water droplet contact with the VA-CNT surfaces synthesized using ethanol were given in Figure 36. It was clearly seen that the hydrophobic VA-CNTs grown at low synthesis temperature (625 °C) were patterned after their contact with water droplet. However, the super-hydrophobic VA-CNTs grown at high growth temperature (750 °C) kept their original alignment even after a droplet on CNT surface was evaporated. As a conclusion, it is found that wettability of VA-CNTs could be tuned by varying carbon source without inducing any chemical modification and thus 2D and 3D functional CNT surfaces could be built by a facile route for further applications.

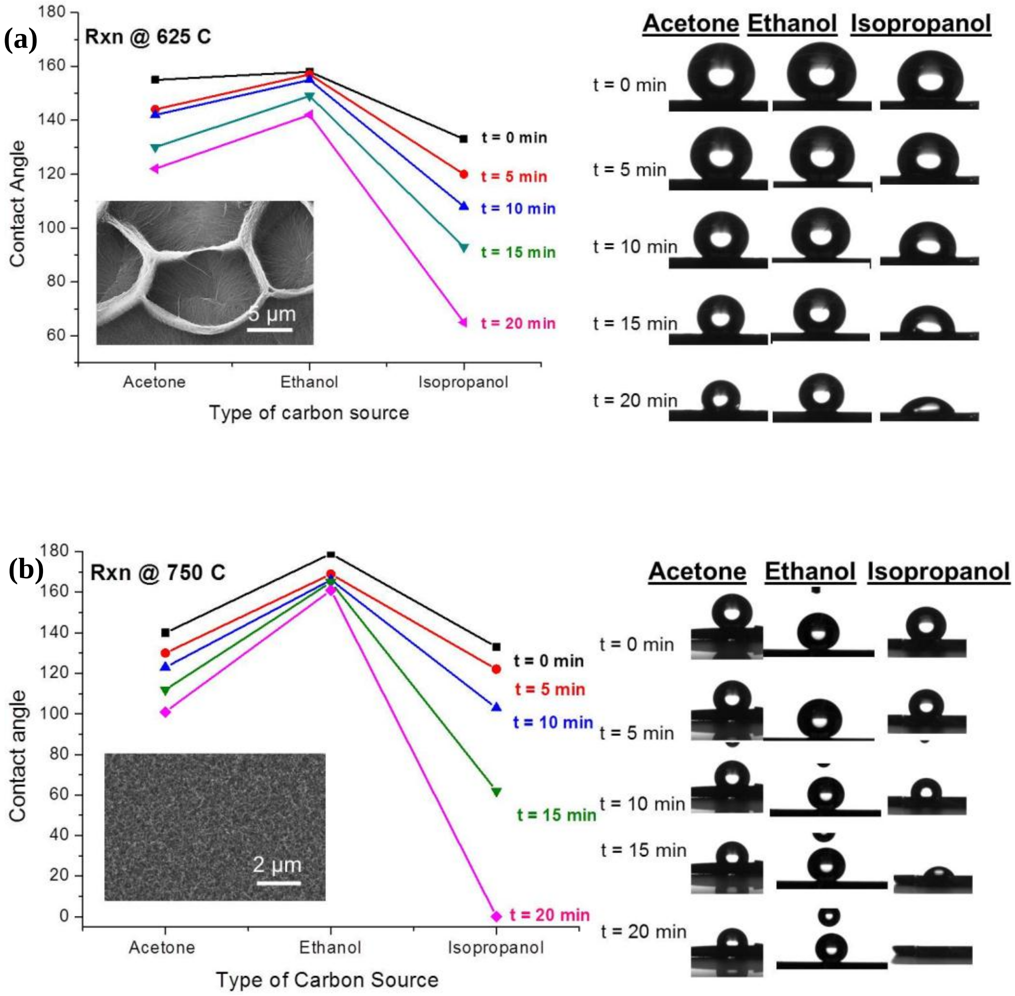

Figure 36. Dynamic contact angle measurements of VA-CNTs synthesized using various carbon sources at temperatures of (a) 625 °C and (b) 750 °C. The volume of water droplet used for the measurements was 8 μL.

Beside the investigation of carbon source type effect, the effect of growth pressure on VA-CNT synthesis was also investigated. The reduction step for all pressure experiments was conducted in a same manner discussed before at temperature of 625 ^{0}C. After the annealing step, the reduced catalyst layers were subjected to the growth step at 625 ^{0}C for 30 minutes using ethanol at varying ACCVD pressure; 40, 56, 69, 81 and 94 Torr. During the growth step, the temperature of liquid ethanol inside the bubbler was kept at 32 °C and the pressure of ACCVD system was adjusted by the valve placed at the end of the furnace. In order to investigate the growth behavior VA-CNTs with respect to both pressure and catalyst design, different bottom Al layer thickness was used in the sandwich catalyst design; 3, 5, 7 and 10 nm Al.

Figure 37 shows the SEM images of synthesized VA-CNTs at different ACCVD pressures at 625 °C and the plot represents the change of CNT length versus ACCVD pressure. Regarding to the plot in Figure 37, it was found that there was an increase in the height of VA-CNTs till 69 Torr pressure where the highest VA-CNT was achieved for each catalyst design. Then, there was a tremendous decrease in the height of VA-CNTs with respect to pressure. Contrary to the effect of carbon source type and temperature, varying ACCVD pressure has the benefit of only affecting the carbon source concentration flowed inside the furnace and not to the decomposition processes. As mentioned before in this study, ethanol was carried inside the ACCVD furnace by bubbling Ar and H_2 gases through and unreacted ethanol was collected inside a trap at the end of the furnace by liquid N_2 cooling. The amount of reacted ethanol was calculated by measuring the volumes of unreacted ethanol which was cooled down at the end of the ACCVD growth (calculations were provided at Appendix IV). Regarding to these calculations, it was found that there was a decrease in amount of ethanol carried inside the furnace from 3.1 to 1.5 sccm as the pressure increased from 40 to 94 Torr, respectively. The flow amount of Ar and H_2 gases were kept constant at 120 sccm while the total amount of flow including ethanol, Ar and H_2 gases decreased with respect to increased pressure. The decrease in the total amount of flow was resulted in an ascend of ethanol residence time (τ) which was expressed with the following equation (Eq. 3);

$$\tau = \frac{System\ volume}{Total\ flow} \qquad (3)$$

The increase in value of τ with respect to pressure provides more time to carbon species to contact with catalyst surface which leads a rise in carbon concentration on the surface of catalyst particle. If contact time of carbon species increases, there is more possibility for carbon coating on catalyst surface since the carbon precipitation is a slower process than the carbon diffusion process. Thus, the increased value of τ would be the reason for the growth of shorter VA-CNTs after a certain value of ACCVD pressure.

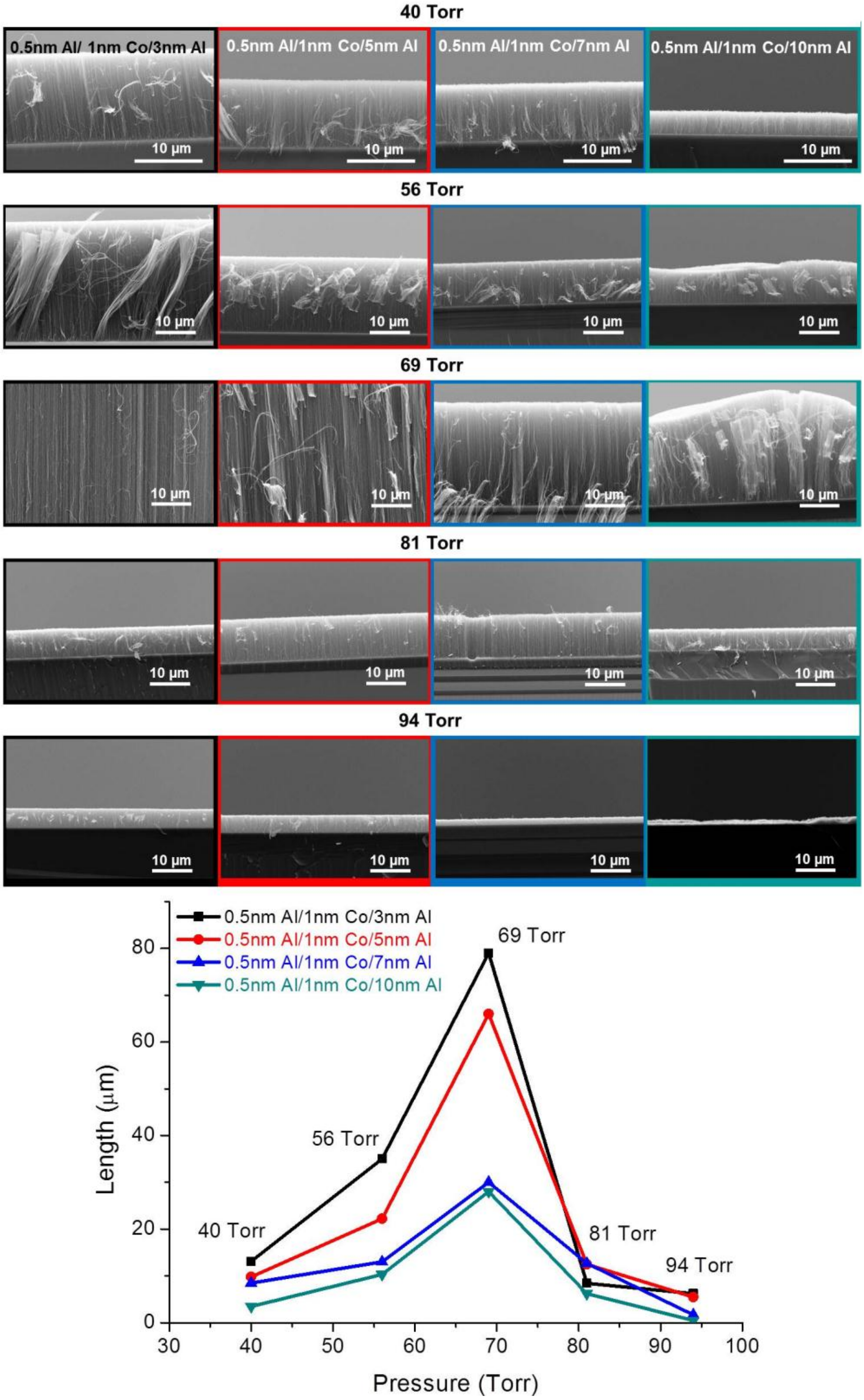

Figure 37. SEM images of VA-CNTs synthesized under pressures of 40, 56, 69, 81 and 94 Torr at 625 °C (pressure set). The plot of the VA-CNT length versus pressure.

The aim of the following experimental set (concentration set) was to investigate how growth of VA-CNTs has been affected from comparatively higher carbon source flow while ACCVD pressure was kept at similar values with pressure set. In the previous set (pressure set), temperature of liquid ethanol inside the bubbler was kept at 32 °C and the pressure of ACCVD system was adjusted by the pressure valve. However, in the following set, the only way to obtain higher concentrations of ethanol flow inside the ACCVD furnace was to increase the temperature of liquid ethanol inside the bubbler while the pressure was kept at similar values with the previous pressure set (see Table 3 for the values of pressure inside the ACCVD, amount of ethanol flow and temperature of liquid ethanol inside the bubbler). Hence, a second set of experiment (concentration set) was conducted where the temperature of liquid ethanol inside the bubbler was altered by using a heater. Varying the temperature of ethanol inside the bubbler affects the amount of ethanol flow inside the furnace and as a consequence the pressure of ACCVD would change. Thus, in this set of experiment, the temperatures of bubbler were selected as 52, 71 and 83 °C to provide similar pressures used in pressure set experiments. The pressures obtained by increasing ethanol temperature are given in Table 3.

Table 3. Summary of the values used in the experiment series of pressure and concentration. The bold values are for the pressure set while the rest is for the concentration set.

Pressure of ACCVD (Torr)	*Temperature of liquid ethanol (°C)*	*Flow of gas ethanol (sccm)*
40	**32**	**3.1**
56	**32**	**2.9**
69	**32**	**2.6**
81	**32**	**2.2**
94	**32**	**1.5**
53	50	4.5
71	71	6.3
81	83	7.2

Figure 38 shows side view SEM images of VA-CNTs synthesized at various temperatures of liquid ethanol which was designated as concentration set. The plot in Figure 38 indicated that the optimum value of temperature was 50 °C which resulted in tallest VA-CNTs at 53 Torr pressure. To better understand the effect of ethanol temperature on the growth, the amounts of ethanol flow were calculated and tabulated in Table 3 for each temperature (Appendix V). According to these values, the flow of ethanol was increased with respect to temperature which also caused an increase in flow concentration of ethanol. As mentioned before, over-feeding of carbon source would deactivate a catalyst particle by covering the surface with excess amount of carbon. In this study, it was observed that the growth rate accelerated up to 53 Torr pressure although the amount of ethanol flow was increased as the temperature of ethanol was raised (Figure 38). After a pressure was reached to 53 Torr, the growth rate of CNTs was decelerated even the pressure was increased up to 81 Torr. The possible explanation for the higher growth rate up to 53 Torr pressure would be related with τ. Just as the amount of flow inside the furnace has been increased, the τ of carbon source inside the furnace would be decreased (Eq.5). Therefore, the carbon source molecules would have less time for the decomposition and also for the contact of carbon with catalyst and this would help to keep the catalyst surface clean. However, after 53 Torr pressure, the concentration of carbon source was came up a threshold value causing the deactivation of catalyst by coating the surface with carbon even the value of τ decreased. In the plot, there was no height value for the 0.5nm Al/1nm Co/10nm Al catalyst configuration at 81 Torr pressure since randomly scattered CNTs rather than VA-CNTs were present on the surface (Figure 38).

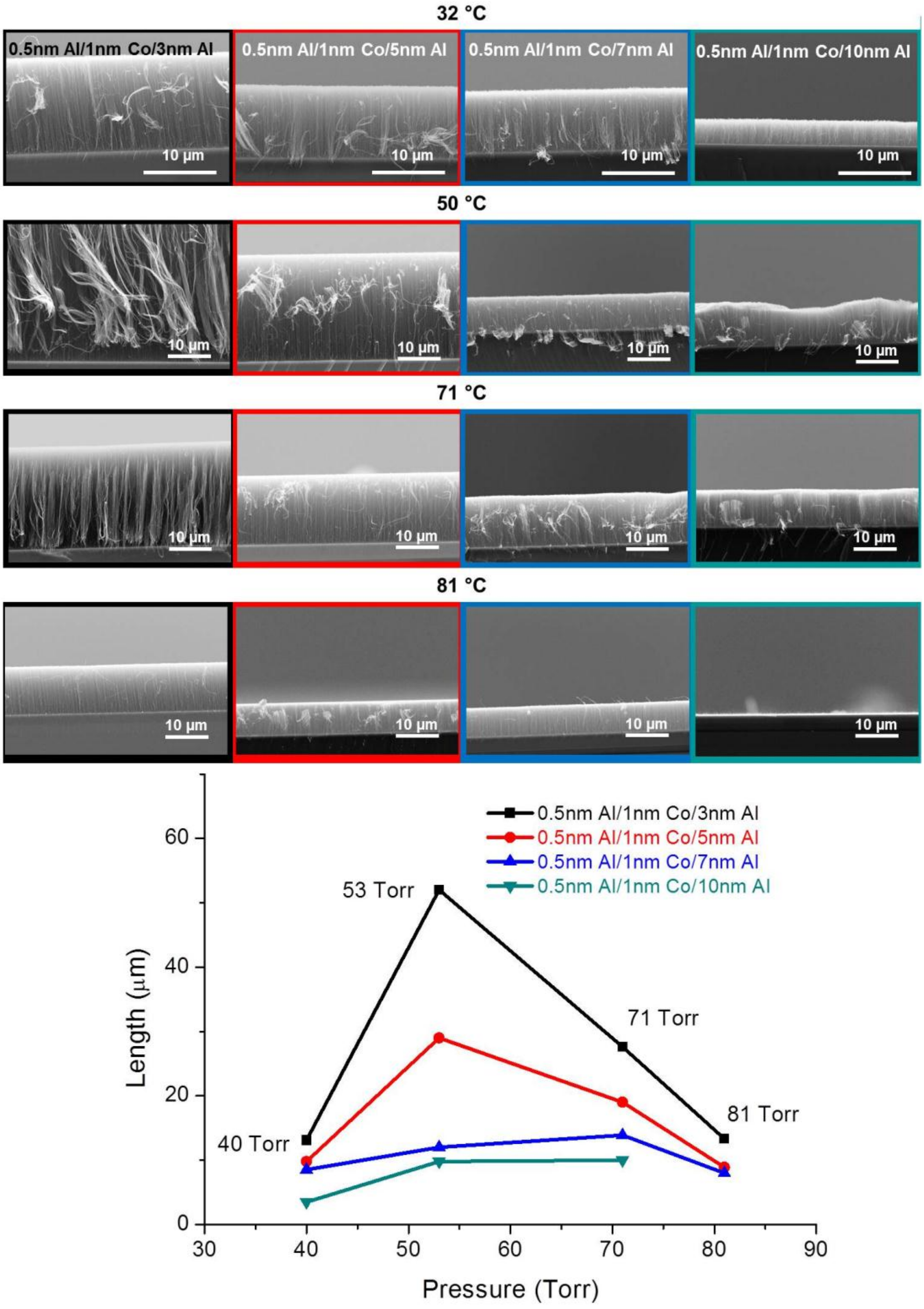

Figure 38. SEM images of VA-CNTs synthesized using various liquid ethanol temperatures (32, 50, 71, 81 °C) at 625 °C (concentration set). The plot of the VA-CNT length versus pressure that obtained by varying liquid ethanol temperature.

Furthermore, Raman analysis was conducted on synthesized VA-CNTs using 0.5nm Al/1nm Co/10nm Al catalyst design. Raman spectra of all VA-CNTs synthesized using different concentrations and pressures were almost identical in terms of intensity and peak positions. Thus, only two Raman spectra of VA-CNTs synthesized at pressure of 40 and 94 Torr (pressure set) were shown here as a representative ones (Figure 39). D and G bands were located around 1327 and 1573 cm^{-1}, respectively, and the ratio of I(G/D) was around 0.7. This indicated the presence of amorphous carbon and suggested that the amount of amorphous carbon did not change with respect to an increase in ACCVD pressure. Regarding to the results, an increase in the pressure or temperature of ethanol only affects the activity of catalyst, not the formation of CNT.

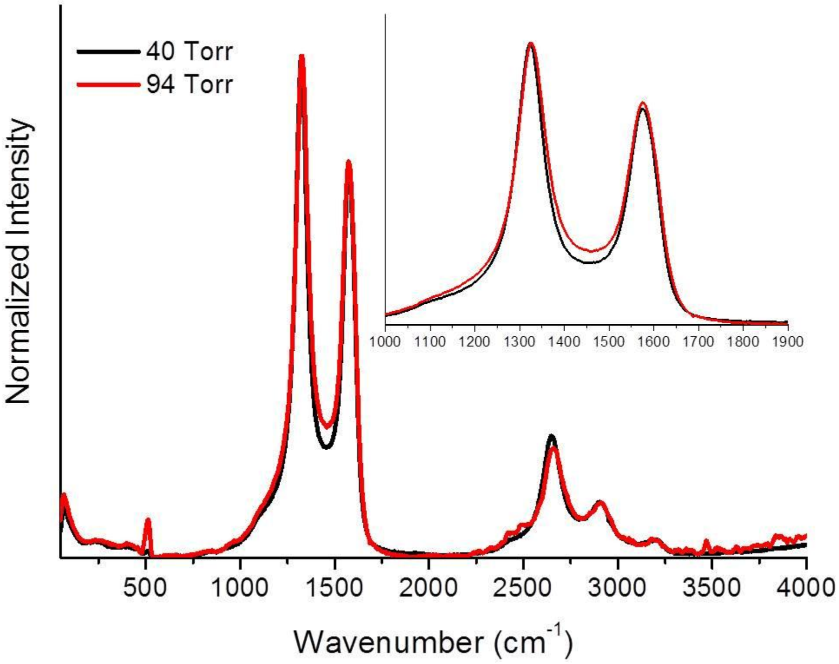

Figure 39. Raman spectra of VA-CNTs synthesized at pressure of 40 and 94 Torr (black and red lines, respectively) with an inset of magnified D and G bands.

In this study, an optimized strategy was developed for the growth of VA-CNTs using ACCVD method by alternating the growth parameters such as carbon source type, temperature and pressure. As a conclusion, the optimum growth range could be offered rather than pointing a certain growth parameter. Alcohol sources resulted in well aligned CNTs rather than hydrocarbon sources at temperature of 625 and 750 °C under the pressure of 40 – 69 Torr. Hence, it is vital to use alcohols as a carbon source to produce VA-CNTs using ACCVD method. Furthermore, it is found that surface properties of VA-CNTs could be tuned by varying growth parameters without inducing any chemical modification and thus 2D and 3D functional CNT surfaces could be built by a facile route for further applications. For instance, hydrophobic VA-CNTs grown at 625 °C using ethanol would be useful for cell applications (*154*) while super-hydrophobic VA-CNTs would be more successful for self-cleaning surfaces (*155*).

4.1.4 Modeling for the growth of vertically aligned carbon nanotubes

To modify CNT properties and to extend their applications, it is important to understand their growth mechanism. In the literature, there are recent reports investigating the growth kinetics of VA-CNTs using *in situ* measuring systems (*59*, *60*, *156–160*). However, in this study, there was no *in situ* system mounted with the ACCVD furnace hence a road of approach was followed for understanding the growth mechanism of VA-CNTs.

Before main processes responsible for the growth termination will be studied, all the possible reactions for ethanol decomposition will be discussed with help of thermodynamic parameter which is the formation Gibbs free energy (ΔG_f) at around 600 °C (*161*). From the view of thermodynamic equilibrium, reactions 3, 4, 5, 6, 7 and 10 are favorable to occur. However, reactions 8 and 9 are unfavorable due to comparatively higher ΔG_f value. Main ethanol decomposition reactions are 3 and 4 where methane (CH_4) and ethylene (C_2H_4) are produced to be used as carbon source for CNT growth. For carbon synthesis, reaction 6 has the lowest ΔG_f value compared with reaction 5. Thus, originally CNTs are grown from the decomposition of C_2H_4 when ethanol is used as the feedstock.

$$C_2H_5OH_{(g)} \rightarrow CO_{(g)} + H_{2(g)} + CH_{4(g)} \qquad \Delta G_f \sim -158\frac{kJ}{mol} \qquad (Rxn. 3)$$

$$C_2H_5OH_{(g)} \rightarrow C_2H_{4(g)} + H_2O_{(g)} \qquad \Delta G_f \sim -66\frac{kJ}{mol} \qquad (Rxn. 4)$$

$$CH_{4(g)} \rightarrow C_s + 2H_{2(g)} \qquad \Delta G_f \sim -5\frac{kJ}{mol} \qquad (Rxn. 5)$$

$$C_2H_{4(g)} \rightarrow 2C_{(s)} + 2H_{S(g)} \qquad \Delta G_f \sim -108\frac{kJ}{mol} \qquad (Rxn. 6)$$

$$2CO_{(g)} \rightarrow C_{(s)} + CO_{2(g)} \qquad \Delta G_f \sim -17\frac{kJ}{mol} \qquad (Rxn. 7)$$

$$C + H_2O_{(g)} \rightarrow CO_{(g)} + 3H_{2(g)} \qquad \Delta G_f \sim +10\frac{kJ}{mol} \qquad (Rxn. 8)$$

$$CH_{4(g)} + H_2O_{(g)} \rightarrow CO_{(g)} + 3H_{2(g)} \qquad \Delta G_f \sim +5\frac{kJ}{mol} \qquad (Rxn. 9)$$

$$H_2O_{(g)} + CO_{(g)} \rightarrow H_{2(g)} + CO_{2(g)} \qquad \Delta G_f \sim -7\frac{kJ}{mol} \qquad (Rxn. 10)$$

There are two main concepts responsible from the growth termination of CNTs; diffusion limit of carbon feedstock and catalyst poisoning. It is worth clarifying that the concept of diffusion limit comes forward when CNT growth model is the bottom up. The concentration of carbon source molecules at the root of CNTs would be much lower than the top if carbon source molecules are not diffusing fast enough through the root of CNTs. As follows, the growth rate would be decreased due to this concentration difference between the root and top of arrays. This effect is called diffusion limit of carbon feedstock. Other than diffusion limit, another important limitation comes from the catalyst coating by amorphous carbon.

To figure out the dominant processes in this study, following calculations were performed by using data collected from VA-CNTs grown on 0.5nm Al/1nm Co/10nm Al catalyst layers under 40 Torr pressure. First, it was needed to define the growth model of VA-CNTs in order to check whether the diffusion limit was dominant or not. For this, XPS analysis was performed on top of VA-CNTs. The signal of C 1s at 284.4 eV was coherent with the presence of CNTs while there was not a signal for Co 2p (Figure 40). This indicated that in this study the growth was root type and diffusion limit should be considered as well the catalyst poisoning for the termination of VA-CNTs.

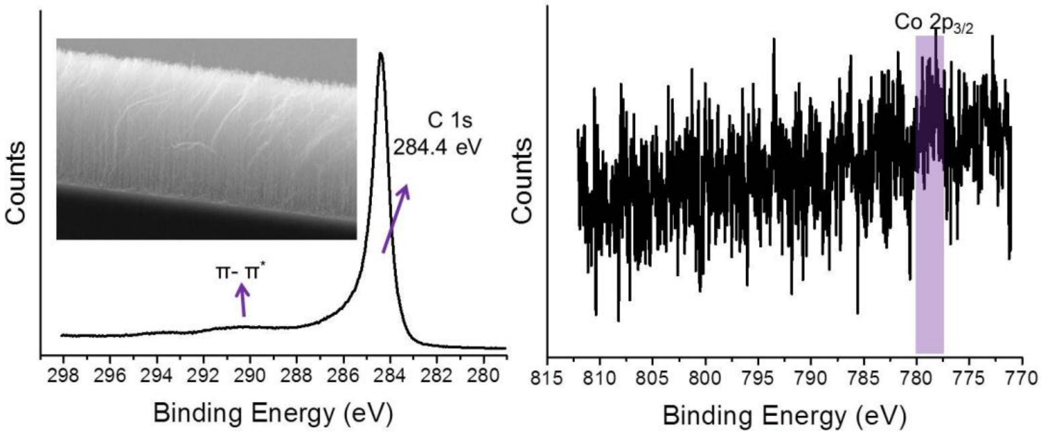

Figure 40. XPS spectra taken from the top surface of VA-CNTs. C 1s peak at 284.4 eV was attributed to the presence of CNTs while there was no signal for Co 2p indicating the root growth type.

Figure 41 represents the root growth and boundary conditions for the following calculations. It was assumed that the diffusion of feedstock was only from the top side (neglected the diffusion from sides of arrays because of high width of film and higher collision frequency in the anisotropic structure of film). Following the basic diffusion theory (Fick's Law; Eq. 4), the difference in the amount of feedstock diffusing in and out should be equal to the consumption inside the *dx* region. It was assumed that the system was at the steady state and there would be no consumption. This was expressed by Eq. 5 where D_e is the effective diffusion coefficient, *S* CNT film area, and C feedstock concentration.

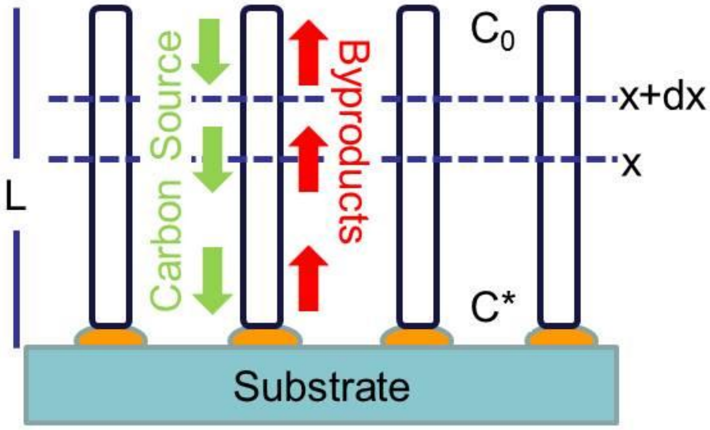

Figure 41. Representative side view schematic of VA-CNTs showing the boundary conditions for the calculations.

$$J = -D_e S \frac{dC}{dx} \qquad (4)$$

$$D_e S \left(\frac{dC}{dx}\right)_{x+dx} - D_e S \left(\frac{dC}{dx}\right)_x = 0 \qquad (5)$$

At the root of CNTs where the catalyst is during the growth, the growth rate of CNT (γ) equals to the reaction rate of carbon source (r) or net diffusion flux at the equilibrium case (Eq. 6) where k_s is the surface reaction constant of carbon source, C^* effective carbon source concentration at the root, L total length of VA-CNTs and m reaction order. In here k_s is the reaction constant for overall processes which are the carbon source decomposition, carbon diffusion inside the catalyst and carbon precipitation for CNT formation.

$$J = r = \gamma$$

$$D_e S \left(\frac{dC}{dx}\right)_{x=0} = k_s S C^{*m} = S \frac{dL}{dt} \qquad (6)$$

Using this relation, the flux equation is solved as;

$$D_e\left(\frac{dC}{dx}\right)_x - D_e\left(\frac{dC}{dx}\right)_{x+dx} = 0 \quad \Rightarrow \quad \frac{dC}{dx} = constant\ value\ or\ \frac{d^2C}{dx^2} = 0$$

This means that feedstock concentration is linearly changing from top to bottom.

$$\frac{dC}{dx} = \frac{C_0 - C^*}{L}$$

$$D_e S\frac{C_0 - C^*}{L} = k_s S C^{*m} = S\,\frac{dL}{dt} \qquad (7)$$

To investigate the reaction order, the growth of VA-CNT were conducted under 40 Torr pressure at 625 °C for varying growth duration after the sandwich catalyst layer was reduced at 625 °C for 15 minutes. The plot of the VA-CNT length versus growth time showed that the length of VA-CNTs increased by ACCVD time till 20 minutes (Figure 42). After 20 minutes passed, the growth rate slowed down and then it was terminated around 40 minutes. Even, the ACCVD time prolonged to 60 minutes, the length of VA-CNTs did not change. This is a typical decay process and is expected to be a first order reaction rate. Hence, based on this plot it was assumed that *m* equals to one and k_s was constant with respect to time. Moreover, it was assumed that reactions were irreversible meaning that there would be no reactivation mechanism of catalyst as shown in reaction 8.

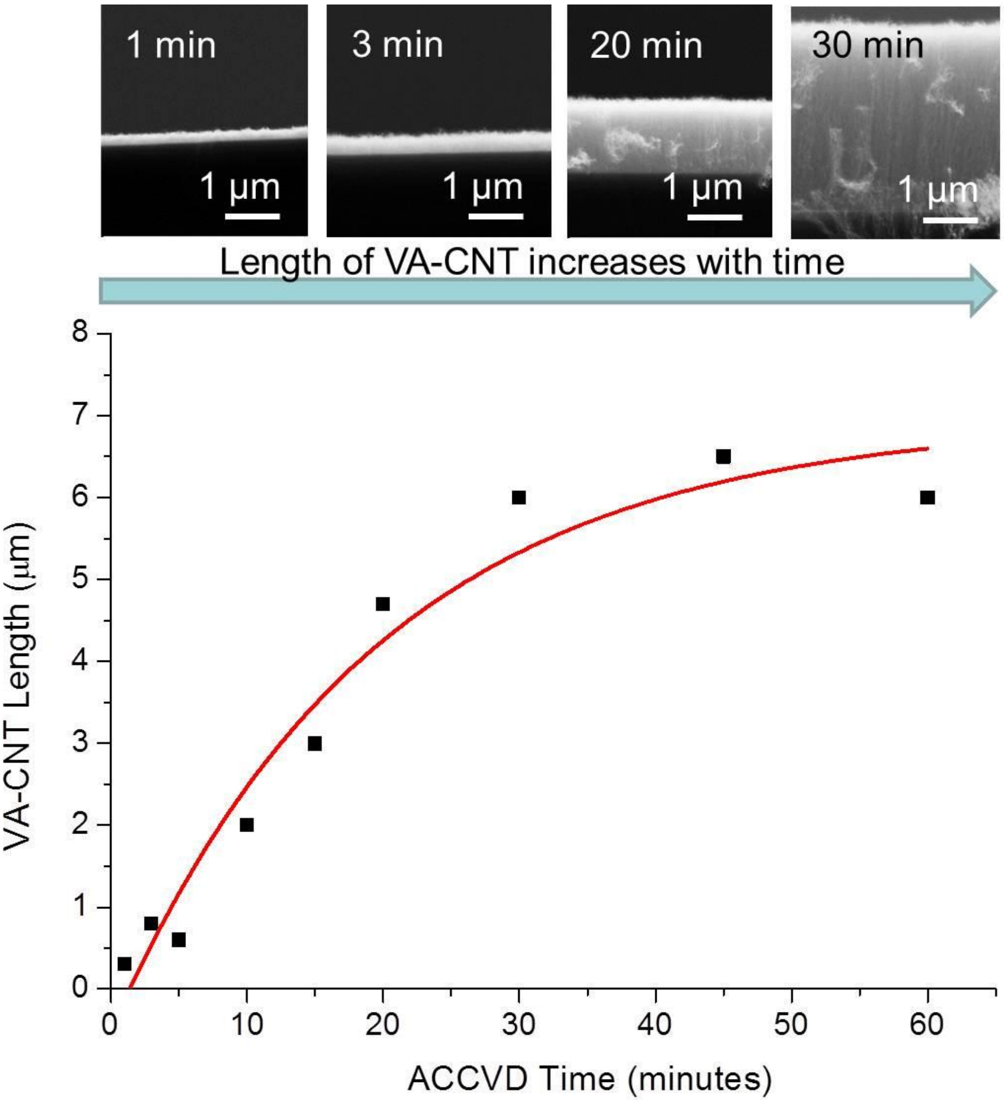

Figure 42. The plot of the VA-CNT length versus growth time with representative SEM images of VA-CNTs grown at 625 °C.

According to the first order reaction rate, C^* was calculated using Eq. 7 and it was found that;

$$C^* = D_e C_0 \frac{1}{(D_e + Lk_s)} \quad (8)$$

Using Eq. 8, the length difference was driven as;

$$\frac{dL}{dt} = k_s C^* = k_s \frac{D_e C_0}{D_e + L k_s} \quad (9)$$

The integration of Eq. 9 resulted in a formula for the length of VA-CNT related with t, D_e, k_s and C_0 (Eq. 10).

$$L = \sqrt{\left(\frac{D_e}{k_s}\right)^2 + 2D_e C_0 t} - \frac{D_e}{k_s} \quad (10)$$

Using this formula, an explanation would be done for the growth termination which was the result of either strong diffusion or no diffusion process. If $(D_e/k_s)^2 < (2D_eC_0t)$;

$$L = \sqrt{2D_e C_0 t} \quad ; \quad L \propto \sqrt{t} \ (strong\ diffusion\ limit) \quad (11)$$

If $(D_e/k_s)^2 > (2D_eC_0t)$;

$$L = C_0 k_s t \quad ; \quad L \propto t \ (no\ diffusion\ limit) \quad (12)$$

To find out the limiting factor, the values of D_e, k_s and C_0 should be defined. First, the type of feedstock diffusion was needed to be assigned using mean free path of carbon molecule under these conditions (λ). In a porous solid, a molecule may collide with another molecule or with pore walls. When gas pressure is high, molecule-molecule collisions dominate. In other words, molecular diffusion occurs if λ is relatively short compared to a pore size (x) ($\lambda << x$). At low pressure, collisions are dominantly between molecules and the walls, and it is called Knudsen diffusion where λ >> x. The value of λ was expressed by Eq. 13 where 'a' represented the diameter of ethanol (0.44 nm), N_A Avogadro's number, P pressure, R the gas constant and T temperature;

$$\lambda = \frac{RT}{\sqrt{2}\pi a^2 N_A P} \qquad (13)$$

Using the mean free path formula (Eq. 13), it was found that λ of the carbon source (ethanol) was 2700 nm for the VA-CNT growth at 625 °C under 40 Torr pressure. In this study, the pores could be assumed as the voids between CNTs and the pore diameter, x, was calculated using the density of VA-CNT, (As provided in Table 1, ρ was found to be 9×10^{-11} cm^{-2}). It was assumed that CNTs were closely pack arranged as shown in Figure 43 and the area (A) shown with red lines contained only one CNT. Along with the assumptions, x was found to be around 7 nm using the following equation (Eq. 14). Thus, λ (2700 nm) was much larger than the value of x (7nm) and the Knudsen diffusion occurred in this study when ethanol was fed inside the ACCVD furnace.

$$A = \frac{1}{\rho} = h\,(d + x) \qquad (14)$$

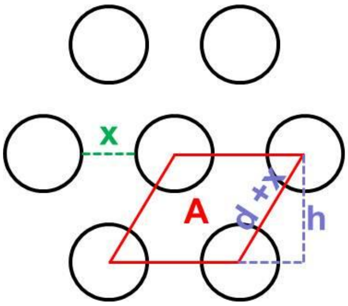

Figure 43. An illustration for the arrangement of CNTs in a closed packed design on a substrate (Each circle represents a CNT).

D_e is expressed as the sum of Knudsen diffusion coefficient (D_k) and the molecular diffusion coefficient (D_m) (Eq. 15). However, it was found that the diffusion of feedstock gas was dominantly Knudsen diffusion and thus D_e was equal to D_k. It is well known that Knudsen diffusion coefficient for cylindrical pores was expressed as in equation 16. However, CNTs did not perfectly straight as cylinders and hence, corrections factors for the shape of pores are added in the previous reports (*60*) (Eq. 17).

$$\frac{1}{D_e} = \frac{1}{D_k} + \frac{1}{D_m} \qquad (15)$$

$$D_k = 4850\, x \sqrt{\frac{T}{M}} \qquad (16)$$

$$D_e \approx D_k = 9700\, x \, \frac{\beta}{\varepsilon} \sqrt{\frac{T}{M}} \qquad (17)$$

In the corrected coefficient equation, β represents the porosity value of arrays and ε is the tortuosity of diffusion channels while M is the molecular weight of gas (M_{ethanol} = 46 g/mol). While β quantifies the ratio of area available for gaseous transport, ε is a quantity which characterizes the nature of the porous pathways followed by diffusing species. In the literature, β was reported as 0.92 (*156*) and ε was 1.5 for VA-CNTs (*60*). Using these values, D_k was found to be 1.84 mm^2/s (Eq. 17).

To calculate the initial concentration of feedstock (C_0), it was assumed that ethanol behaved as an ideal gas at the synthesis conditions used in this study.

Thus, the ideal gas law provided a relation between the pressure of chamber and the concentration where R is the gas constant (62.36 L Torr/K mol) (Eq. 18).

$$PV = nTR$$

$$\frac{n}{V} = C = \frac{P}{TR} \qquad (18)$$

Using the ideal gas law, it was calculated that C_0 value of ethanol feedstock was 7×10^{-4} mol/L at 625 °C and 40 Torr. To investigate the dominant process responsible for the growth termination during the synthesis, a comparison between values of $(D_e/k_s)^2$ and $2D_eC_0t$ was performed. However, for this comparison there was only one missing constant, k_s. To determine the value for k_s, *in-situ* measuring systems are required which was not present in this study. Hence, it was assumed that the value of k_s was between 0.1 and 0.4 mm/s as reported previously in the literature for MWCNTs (*159*).

Regarding to these values, the growth of VA-CNTs at 625 °C under 40 Torr pressure was found to be in a regime where there was not a strong diffusion limit. In a rough conclusion, the growth most probably terminated due to the catalyst deactivation by the accumulation of excess carbon on catalyst surface. In a case of high ethanol pressure, the growth shifts to a regime where there is a strong diffusion limit rather than catalyst poisoning.

4.2 Functionalization of vertically aligned carbon nanotubes

4.2.1 Lithium intercalation of vertically aligned carbon nanotubes

In the literature, there are examples of studies using carbon based materials as electrode in Li-ion batteries due to the structural stability and high capacity (*101*, *162*). Particularly, CNTs are preferred to be used as an electrode material in order to overcome the limitations commonly for conventional electrodes such as low lithiation capacity, slow ion diffusion, low surface area and poor conductivity (*102–104*, *106*, *107*). Furthermore, there was no structural damaging as Li intercalated with CNTs (*106*, *107*). Recently, it was showed that the improvement in the storage, conductivity and rate capacities was achieved if VA-CNTs were used as electrodes (*104*, *108*). It was also reported that aligned CNTs enhanced the Li ion diffusion during charge cycles where it was higher than the graphite and randomly scattered CNTs (*101*, *103*).

In the literature, few studies were published on the growth of carbon nanostructures using Li-containing compounds; however no detailed examination was performed to understand the incorporation of Li to the carbon network (*163*, *164*). In this study, the aim is to *in situ* intercalate VA-CNTs during the growth process and investigate the incorporation of Li to the CNT structure using Raman, XPS, S/TEM and EELS (*165*).

For the Li study, the catalyst layers were prepared using wet chemistry method described in Chapter 3. Basically, SiO_2 wafers were coated using two different catalyst layers; the one was with Li containing (mixture of $Al(NO_3)_3.9H_2O$, $Co(NO_3)_2.6H_2O$ and $LiNO_3$ solutions) and the other was without Li (mixture of $Al(NO_3)_3.9H_2O$ and $Co(NO_3)_2.6H_2O$ solutions). After the catalyst layers were put on the substrates and left for air drying, they were subjected to the reduction and growth steps in the ACCVD furnace at 625 °C by using Ar, H_2 and ethanol for the growth of CNTs. However, for some experiments only the reduction step at 625 °C was performed on the catalyst layers in a same manner described before in order to better examine the intercalation of Li. Hence, for the simplicity, all the experiments conducted in this study were named and a table was given for the summary of experiments (Table 4).

Table 4. Summary of the experiments conducted for Li intercalation study.

Experiment name	Catalyst content	Process run	Observations after ACCVD
Set 1	Li containing Co	ACCVD(reduction+growth)	CNT
Set 2	Li containing Co	ACCVD (reduction)	-
Set 3	Co	ACCVD(reduction+growth)	CNT
Set 4	Co	ACCVD (reduction)	-
Set 5	Co	ACCVD(reduction +growth) + $LiNO_3$ annealing	CNT
Set 6	Co	$LiNO_3$ annealing	-

The growth of VA-CNTs from Li containing catalyst solution (Set 1) was achieved at 625 °C as is the case in the non-Li containing catalyst solution (Set 3) (Figure 44a and b). For further morphological investigation, since SEM is not a powerful technique, S/TEM analysis on the CNTs from Set 1 was conducted (Figure 44c). It was observed that the length of the CNT was around 5 µm and the diameter was between 10 to 20 nm. The particles seen in the S/TEM image was most probably due to the unreacted catalyst stuck on the side walls of CNT.

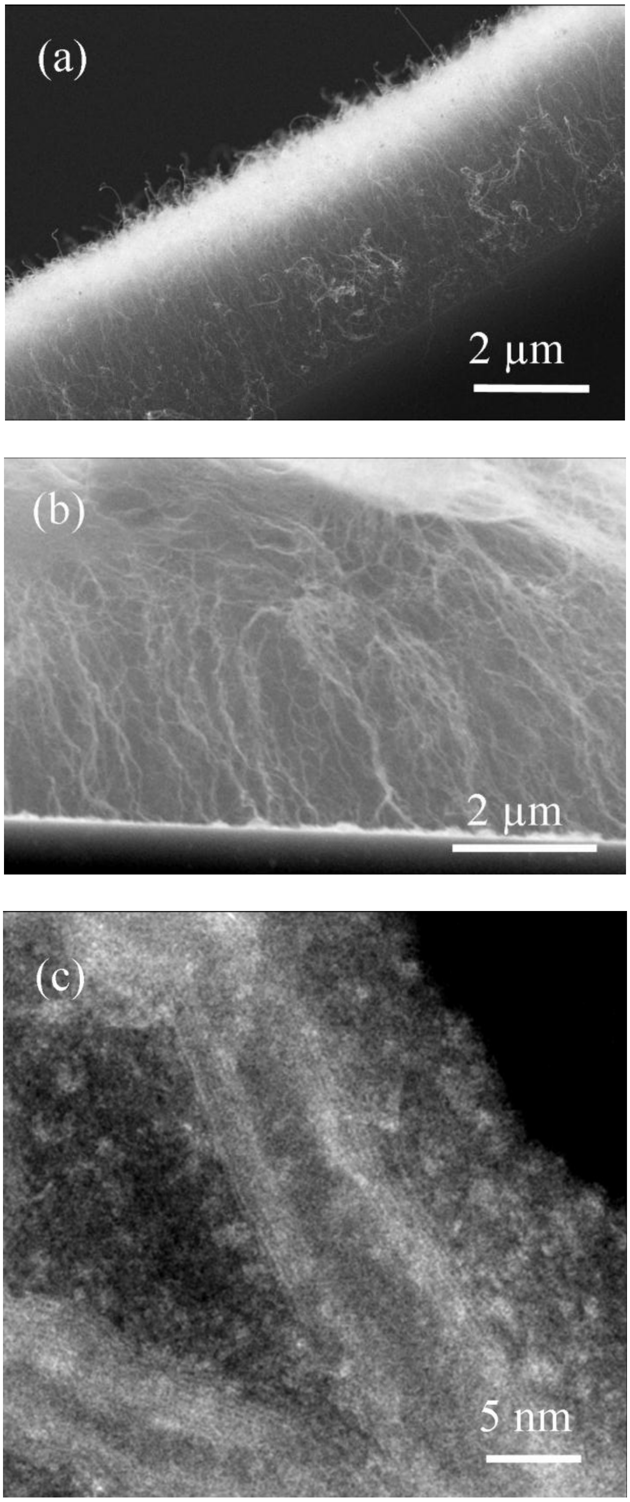

Figure 44. Side view SEM images of grown VA-CNTs from the (a) non-Li (Set 3) and (b) Li containing (Set 1) catalyst layers. (c) S/TEM image of a CNT from Set 1 (*165*).

Other than the electron microcopy images, EELS analysis was performed on the CNT synthesized from Set 1 in order to investigate the chemical composition of the structure. The EEL spectra for Li-*K* and C-*K* edges were provided in Figure 45a and b, respectively, taken from the side wall of CNT (inset image in Figure 45b). Beside the data obtained from the side wall of CNT, the spectra was also collected from the Li containing catalyst particle from Set 1 in order to better differentiate the shape of Li-*K* edge. The energy and shape of Li-*K* edge from the side walls of CNT was different than the LiF, as the reference, and the Li containing catalyst particle (Figure 45a). It was found that the Li-*K* edge was at 55.6 eV for the spectra taken from the side walls of CNT which was shifted by 0.6 – 0.8 eV with respect to the metallic Li-*K* edge where it was reported to be at 55 eV (*166*) and 54.8 eV (*167*). When Li intercalates with C, a new form of compound is generated which is called as LiC_6 and a charge transfer occurs between Li and C. Thus, it is likely that the shift was due to a charge transfer from the Li to the C atoms in the structure. In the literature, it was reported that 0.2 eV shift was observed for bulk LiC_6 compared to the metallic Li-*K* edge (*168*). It was not surprising to observe a sharp edge for the C-*K* edge which suggested the presence of graphite sheets in the sample (Figure 45b). The edge was centered at 285.5 eV (π^*) corresponding to the unoccupied anti-bonding π^*-states of sp^2-hybridized C. In the literature, C-*K* edge for pure CNTs was reported to be at 285 eV (*169*) while it was at 285.5 eV for CNTs intercalated by alkali metals (*170*). Regarding to the EELS spectra, the results would be in agreement with the presence of Li in VA-CNTs.

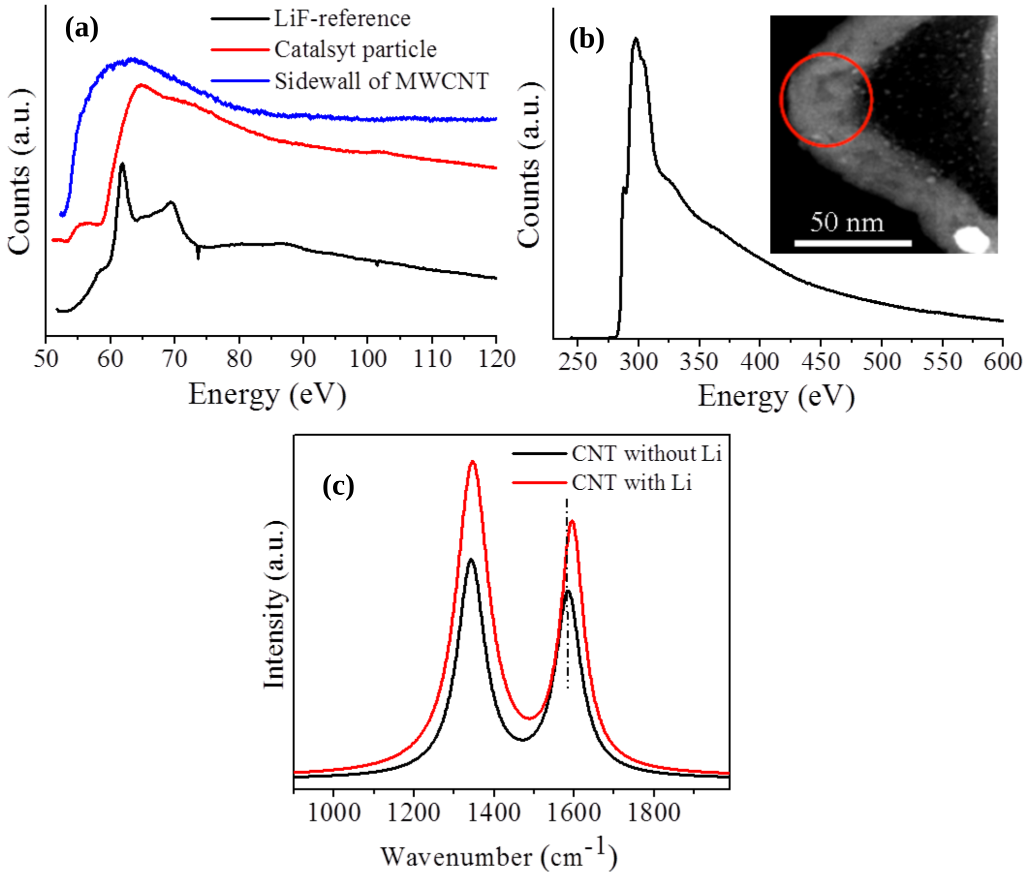

Figure 45. EEL spectra of Set 1 for (a) Li-*K* edge and (b) C-*K* edge (inset shows where the spectrum is taken from). (c) A comparison of Raman spectra for VA-CNTs from Set 1 (Li containing) and Set 3 (non-Li containing) (*165*).

Other than microscopy techniques, Raman analysis could also provide an evidence for Li intercalation by shifts in wavenumbers of G band while there would be no shift for D band. Hence, in order to get more information, high resolution Raman analysis was performed on grown VA-CNTs using the Li containing (Set 1) and non-containing (Set 3) catalysts (Figure 45c). It was found that the G band corresponding to in-plane vibration of C atoms was at

1594 cm^{-1} and 1582 cm^{-1} for VA-CNTs grown in Set 1 and Set 3, respectively. However, D band for both samples attributed to disorder and defects was found to be at same wavenumber value of 1344 cm^{-1}. This indicated that the D band position did not get affected by the presence of Li while the G band shifted up 11 cm^{-1} respect to the Set 3 with the presence of Li. In the literature, there are several studies reporting a G band shift toward higher wave numbers values (*171*, *172*). The possible explanation for this is the charge transfer due to the insertion of Li to the carbon network (*165*, *171*, *172*).

Although TEM and Raman analysis techniques resulted in strong evidences for the presence of Li in the carbon matrix, XPS analysis was also performed. To better understand the chemical states of Li, other than VA-CNTs from Set 1 and Set 3 the catalyst layers from Set 2 and Set 4 were also analyzed. As tabulated in Table 4, Li-containing (Set 2) and non-containing (Set 4) catalyst layers were only subjected to the reduction step at 625 °C to figure out the catalyst state after thermal treatment. XPS spectra for Li 1s and C 1s peaks were shown in Figure 46 and the binding energies of the peaks were tabulated in Table 5. The XPS spectrum of reduced non-Li containing catalyst layer (Set 4) was shown in Figure 46a. As shown, it had a broad asymmetric peak observed at 59.5 eV which was corresponding to Co 3d (*173*). In the XPS spectrum of reduced Li-containing catalyst (Set 2), there was a second peak centered at 54.9 eV which fitted to metallic Li (Figure 46b) (*174*). This indicated that Li and Co were metallic on the substrates after the reduction step conducted.

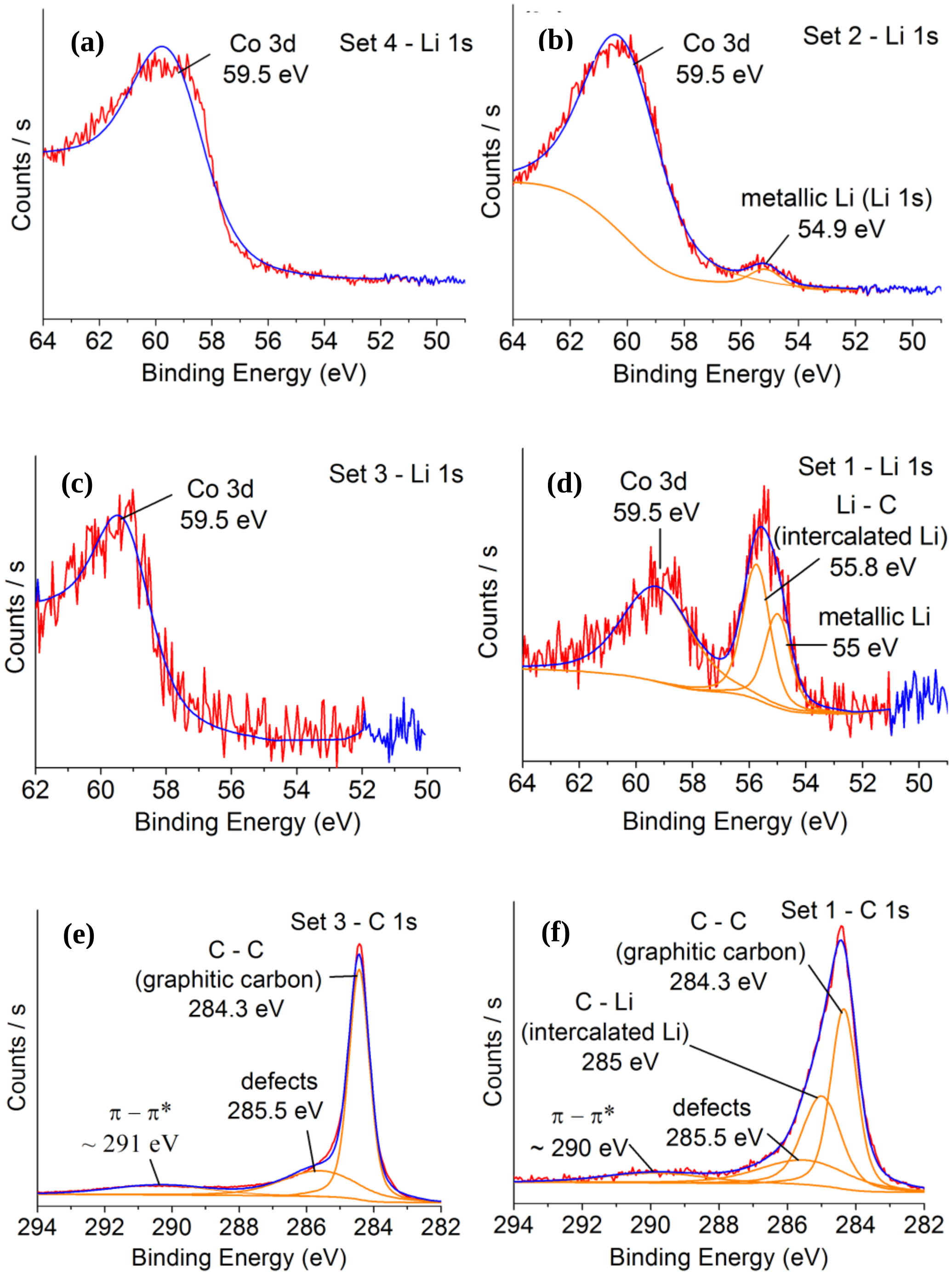

Figure 46. Li 1s XPS spectra of (a) Set 4, (b) Set 2, (c) Set 3 and (d) Set 1. C 1s XPS spectra of (e) Set 3 and (f) Set 1 (*165*).

Table 5. Binding energies and FWHM for C 1s and Li 1s XPS peaks.

Experiments	Binding energy Li 1s (eV)	Binding energy C 1s (eV)
Set 1	55.8	284.3(0.9) 285.0 (1.9)
Set 2	54.9	-
Set 3	-	284.3 (0.7) 285.5 (2.8)

After the chemical state of reduced catalyst layers were investigated, XPS analysis was carried on the synthesized VA-CNTs using these catalysts (Set 1 and Set 3). For the case where CNTs were grown on the non-Li containing catalyst layers (Set 3), Co 3d peak was observed at 59.3 eV (Figure 46c). In the Set 1 (Li containing catalyst), three peaks were appeared around 55 eV (metallic Li 1s), 55.8 eV (Li 1s) and 59.5 eV (Co 3d) (Figure 46d). It was reported that Li 1s peak for the case of Li intercalation in the LiC_6 shifted towards higher binding energy compared to the metallic Li and appeared at 56 eV and the main reason for the shift is the charge transfer from Li to C (*175*). Regarding to the results, it was found that there was a shift towards higher binding energy when the Li 1s peaks of reduced Li containing catalyst (Set 2 – 54.9 eV) and CNTs grown on the Li containing catalyst (Set 1 – 55.8 eV) were compared. This supported the idea of Li intercalation during the CNT growth (Set 1).

The effect of Li intercalation was also observed at C 1s peak. Firstly, the shape of C 1s peak of CNTs grown using Li containing catalyst (Set 1) was distinct to that for CNTs grown on non-Li containing catalyst (Set 3) (Figure 46e and f, respectively). The main C 1s peak for Set 1 was broader than the one in Set 3. After the deconvolution of sample Set 3, it was found that the graphitic C peak was at 284.3eV with 0.7 eV full width half maximum (FWHM) with a broad component at 285.5 eV due to C-H bonding which was consistent with the reports (*176–178*) (Figure 46e). In the case of Set 1, the C 1s peak had a main component at 284.3 eV and a broader one at 285 eV (Figure 46f). The peak at 285 eV was corresponding to the Li intercalated CNTs and shifted toward higher binding energy with respect to the peak at 284.3 eV which was for the CNTs grown with non-Li containing catalyst. According to the report done by Momose *et al.*, C 1s peak has been observed between 285 – 285.2 eV for the Li intercalated LiC_6 and LiC_2 (*179*). Moreover, it was reported that the broadening of the peak with respect to that graphitic C peak (284.3 eV) was due to re-distribution of charge on the carbon network induced by Li (*178*, *180*, *181*).

In order to further confirm the intercalation of Li during the growth, another set of experiments were conducted where VA-CNTs were synthesized using non-Li containing Co catalyst at 625 °C in a same manner. After VA-CNTs were grown, they were soaked in a $LiNO_3$ solution for overnight. Next, a drop containing CNTs were taken from the $LiNO_3$ solution and put on a Si substrate. Air dried CNTs on the substrate were subjected to the annealing step at 625 °C under 4 Torr pressure and flowing atmosphere of Ar and H_2 (5:1). This sample was named as Set 5 in Table 4. Moreover, for comparison, Si substrate was coated with only $LiNO_3$ solution and then conducted to the annealing step in a same manner with Set 5. This sample was called as Set 6 in Table 4. In here, the aim was to promote the *ex situ* Li intercalation.

In order to investigate the *ex situ* intercalation, a comparison between the XPS spectrum of Set 5 and Set 6 was performed. In the case of Set 5, Li 1s peak was appeared to be at 54.6 eV (Figure 47a). Moreover, it was found that Li 1s peak from Set 6 (54.8 eV) was also observed at almost same binding energy (Figure 47b). Regarding to the previous reports, Li 1s peak both from Set 5 and Set 6 was attributed to metallic Li (*174*). Furthermore, no evidence was obtained for the asymmetric broadening and shifts in the C 1s peak of Set 5 indicating the Li intercalation (Figure 47c). Thus, it was clear to say that *ex situ* intercalation of Li did not occur by the annealing.

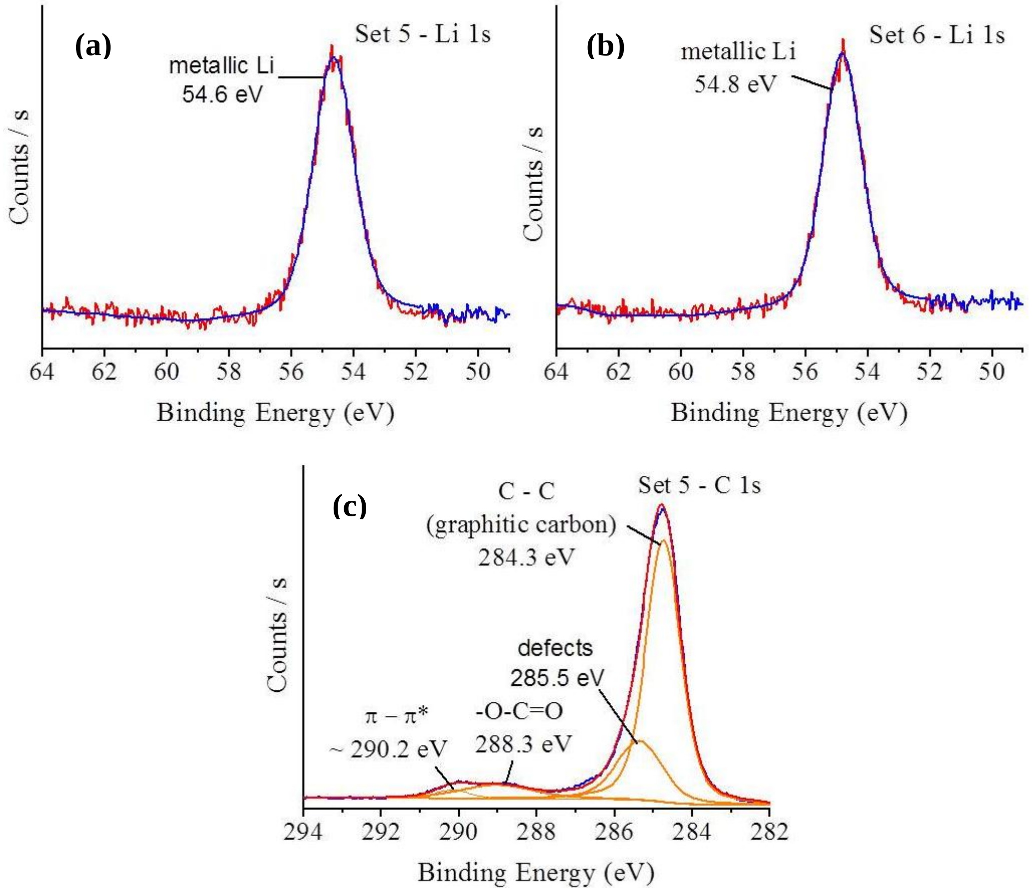

Figure 47. Li 1s XPS spectra of (a) Set 5 and (b) Set 6. (c) C 1s XPS spectra of Set 5 (*165*).

The results of XPS study strongly indicated the intercalation of Li to occur during the growth of CNTs by using Li containing catalysts. It was investigated that Li intercalation did not take place if Li source was supplied after CNT growth. Beside XPS analysis, TEM and Raman results were also suggesting the *in situ* Li intercalation of VA-CNTs by charge transfer from Li to carbon structure. In the literature, there is a controversy for charge transfer between Li and carbon. In order to estimate the charge transfer for this study, density functional theory (DFT) calculations were done by Dr. Oguz Gulseren and co-workers (*165*). The results of DFT calculations were given in Appendix VII.

4.2.2 Cell attachment on patterned carbon nanotubes

The research on the cell attachment has gained important attraction in the last four decades. In recent years, MSCs have become a potential candidate for the tissue engineering applications due to their multiple lineage potentials and immune-privileged properties (*182*, *183*). In the literature, there are studies showing the differentiation capabilities of stem cells into liver and osteocyte cells which would be used for the cell based therapy and tissue engineering (*184*, *185*). However, a key point is to manage the growth and differentiation of cells outside of a body. Since then, ECMs derived from animal tissues such as collagens are used and have an important role in the growth of MSCs (*109*). However, their use brings out some limitations by the dimension and pathogen risk for the growth of cells on (*110*). Therefore, developing better biomaterials is being attracted interest to mimic the candidates for cell adhesion and growth (*111*, *186*).

The application of CNTs has been studied for cell growth in tissue engineering (*187*, *188*). Moreover, CNTs would be considered to be used for scaffold applications since their similar sizes with commonly used collagens (*68*, *111*–*114*). The fundamental principle for cell viability on ECM surfaces is the attachment of cells to surfaces to survive, migrate and grow. The properties of surface such as roughness have a significant role for mimicking the adhesion, proliferation and viability of cells. There are studies in the literature reporting the effect of topography on cell attachment (*189*, *190*). Moreover, it is found that the expressions of cells are increased on relatively rougher surfaces (*191*). However, the results sometimes are controversy for the relationship between surface properties and adhesion (*192*, *193*). In this study, the focus was to use VA-CNTs as functional surfaces to grow cells on. Moreover, the aging effect on the adhesion of cells on the CNTs was also investigated.

For the cell attachment study, the catalyst layers were prepared using PVD techniques as described at Chapter 3 (0.5nm Al/1nm Co/10nm Al) (*194*). The synthesis process of VA-CNTs was performed in a same manner by using ethanol as a carbon source at the low growth temperature (625 °C). The reason for choosing the temperature of 625 °C instead of 750 °C was the hydrophobic surface properties of VA-CNTs grown at 625 °C as shown in Figure 36a. Cells preferentially attach on hydrophilic surfaces, not on super-hydrophobic surfaces as in the case of 750 °C grown VA-CNTs. Hence, for the cell attachment experiments VA-CNTs were synthesized at 625 °C using ethanol which had an average 8 μm length as shown in Figure 48a. TEM image was confirmed that CNTs were multi-walled with an average diameter of 10 nm (Figure 48b). In order to investigate the surface properties of the VA-CNTs, 2D AFM analysis was conducted from the top surface of VA-CNTs (Figure 48c). It was found that the average *w* value was around 40 nm and also the top view SEM image confirmed the smoothness of the surface (Figure 48c, inset). Furthermore, Raman spectra of the synthesized VA-CNTs represented the D and G bands at 1344 and 1582 cm^{-1}, respectively (Figure 48d).

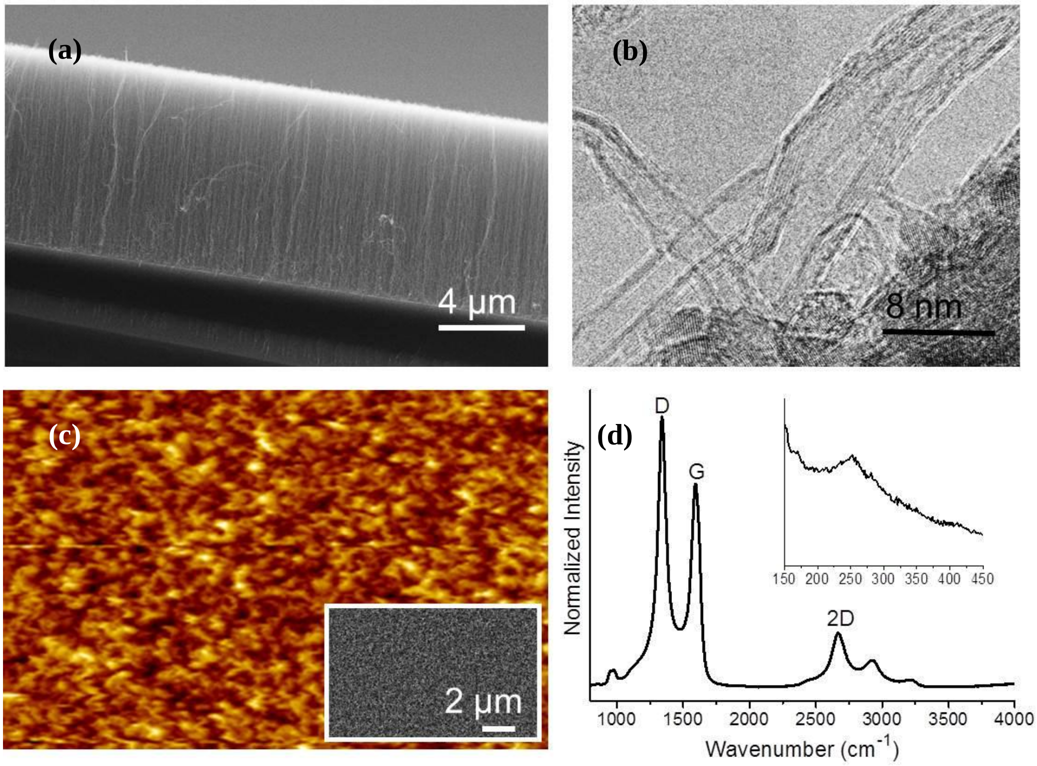

Figure 48. (a) SEM and (b) HRTEM images of VA-CNTs synthesized at 625 °C on the sandwich catalyst layers for the cell attachment experiments. (c) 2D AFM image from the top view of VA-CNTs with inset of top view SEM image. (d) Raman spectra of the synthesized VA-CNTs indicating the variety of MWCNTs as shown in RBM mode as inset (*194*).

As discussed before, cells prefer to attach themselves on rougher surfaces than plane surface (*193*, *195*). Hence, the presence of patterns on the surface is critical for the preparation of a suitable scaffold for anchoring of the cells. Thus, after the VA-CNTs were synthesized, the next step was to create the patterned surfaces for the growth of MSCs. For this, a simple method was applied where 5 μL deionized water was dropped with a syringe on the VA-CNTs as shown in Figure 49 and left for air drying. It was observed that VA-CNTs were self-patterned to form a suitable nest for the cells by some of them collapsing on the substrate due to the capillary forces exerted by water (Figure 50). Similar observation was also reported by Robertson *et al.* (*196*). The main reason for the self-assembled CNTs is thought to be the elasto-capillary effect of VA-CNTs. As shown in Figure 50, the size of these nests was around 10 μm which is equivalent with the average size of MSCs providing a suitable nest.

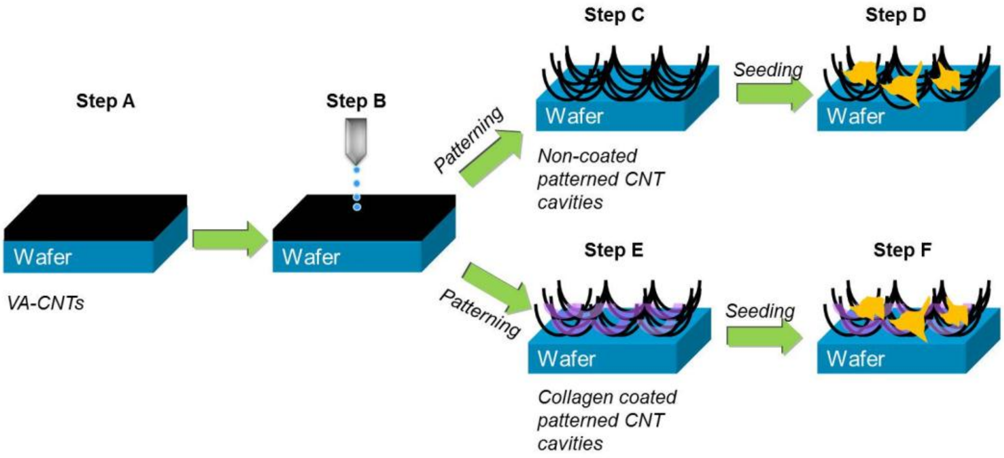

Figure 49. Schematic representation of experimental approach (*194*).

In the literature, there are reports using a composite materials such as CNT/collagen to improve the cell attachment and viability (*111*, *197–201*). In order to investigate the collagen coating effect on the growth of MSCs, following the patterning step, CNT surfaces were either coated with collagen or not. 1µg/µl sterilized collagen solution was applied on the every cm^2 of surface (approximately 10:1 weight ratio of collagen to CNT) results in two different groups of patterned CNT arrays; one non-coated and the other collagen coated (Figure 50).

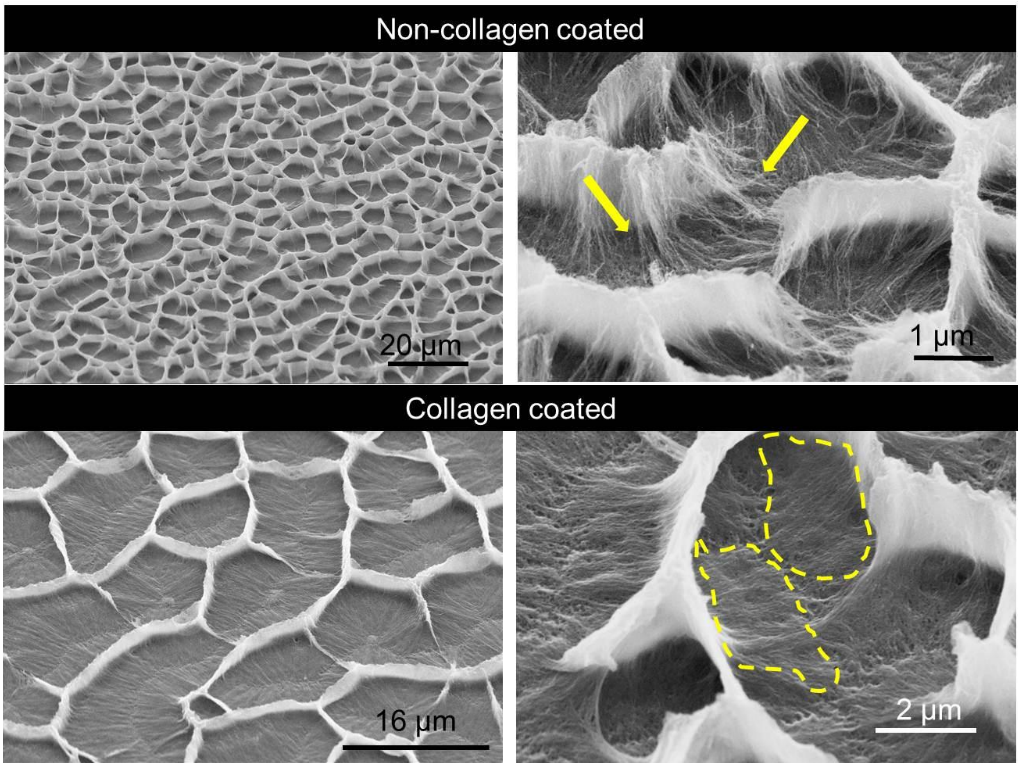

Figure 50. 45° tilted SEM images of non-coated and collagen coated CNT surfaces with higher magnified SEM images showing the smoothing effect of collagen.

At the 14th day of MSC culture, 3 $x10^5$ numbers of cells derived from rat bone marrow were seeded on both the patterned non-coated and collagen coated CNT surfaces and this was stated as passage zero (P0) group in this study. To better understand the adhesion of aged cells, different passage series were used beside P0 series. After P0 passage, MSCs became confluent in the cell culture and then they were passaged for second and third times. In the rest of this study, these were stated as the first passage (P1) and the second passage (P2) groups, respectively. In the same manner with P0, MSCs from P1 and P2 passages were also seeded on the patterned CNT surfaces. The isolation and characterization of MSCs was shown in Appendix VI.

Low vacuum SEM images show that MSCs from P0 passage attached on both non-coated and collagen coated CNT surfaces after three days passed over the seeding of cells (Figure 51a and b). There were so fewer amounts attached cells from P1 and P2 passages on the patterned CNT surfaces. Hence, SEM images were not shown for these passages. Comparison between SEM images did not provide enough information on the adhesion. Hence, all CNT surface was scanned under SEM and numbers of attached MSCs on both CNT surfaces for three passage series were counted. The average areal density of cells was calculated by dividing the number of cells to the total CNT surface area (Figure 51c).

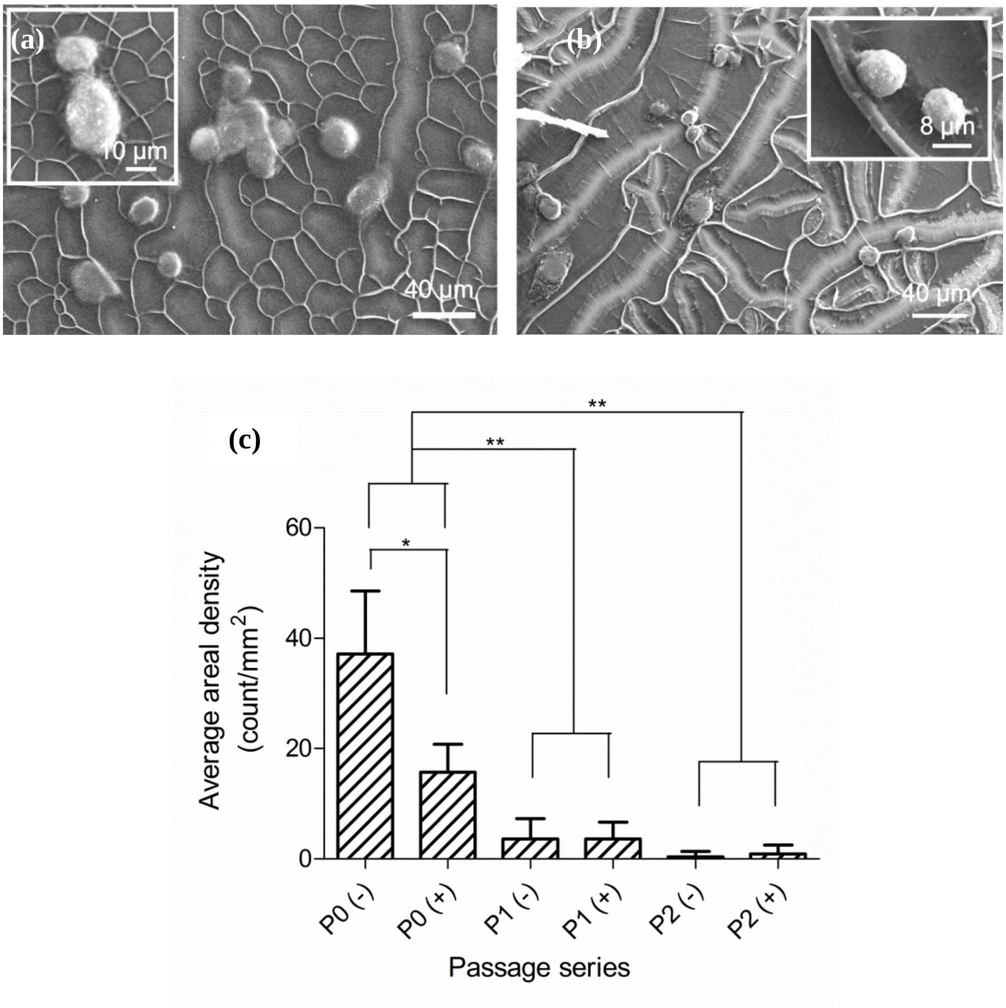

Figure 51. Attached MSCs from P0 passage on the (a) non-coated and (b) collagen coated CNT surfaces. (c) The plot of average areal density of MSCs from three subsequence passages. (-) indicates CNT surfaces without collagen while (+) means collagen coated CNT surfaces (*194*).

The plot shows a decrease in the number of the MSCs through the passage of the cells. When a comparison was done between P0 and P1 and P2, it was found that the decrease was statistically significant (Figure 51c). However, there was not a statistically significant decrease between the number of the cells both on the coated and non-coated patterned CNTs from P1 and P2 passages. Thus, it was suggested that early passages of MSCs, P0, should be preferred for seeding on the patterned CNT surfaces. Interestingly, the number of the MSCs from P0 passage on the non-coated CNT surfaces (P0 (-)) was higher than the collagen coated surfaces (P0 (+)) but not at P1 and P2 series (Figure 51c). In the recent literature about composites of collagen and CNT, the goal is not only to improve the poor mechanical properties of collagen, but also to add further functionality to the scaffold (*154*, *202*). In a study by Cho and Borgens, it was reported the effect of CNT addition into collagen and applied electrical stimuli on the cell viability of PC12 (*197*). According to that study, the metabolic activity of PC12 cells was decreased by the CNT amount at around 50% (wt.) CNT loading (*197*). However, there was no mention of a root cause for this observation. Contrary to the studies, it was found that the number of MSCs for P0 was noticeably higher for the non-coated CNT surfaces than the collagen coated surfaces as shown in (Figure 51c). Simultaneously, there are other studies reporting the enhancement in the viability and the attachment of different type of cells with the addition of CNT to the ECM (*198*, *200*). The study by Hirata *et al.* indicated higher DNA expression for attached mouse osteoblast cells (MC3T3-E1) to a 3D collagen sponge coated with MWCNTs (*198*). In addition, another study confirmed the enhancement in the number of viable smooth muscle cells grown on the collagen/CNT matrix (*200*). Furthermore, surface topography also affects the adhesion of cells to ECM (*193*, *195*). Regarding to these, it was not surprising to observe the attached MSCs both on the collagen coated and non-coated CNT surfaces. It was suggested that the collagen coating on the patterned CNT surfaces acted as a smoothing agent by filling the gaps between the CNTs. Thus, this would limit the anchoring points required for the adhesion of cells. The SEM image provided in Figure 50, displays the comparison of the as-is and collagen infiltrated CNT array surfaces which indicated the smoothing action of the collagen by filling the gaps between individual CNTs.

In addition to the cell count under SEM, the cell viability test (MTT assay; 3-(4,5-dimethyl-2-thiazolyl)-2,5-diphenyl-tetrazolium bromide) was conducted on the MSCs from several passage series grown on the patterned CNT surfaces in the presence and absence of collagen coating. Spectrophotometrical absorbance of the samples was measured by ELISA reader with the wavelength between 550 and 600 nm. The graphs for cell viability are shown in Figure 52 and the control groups in the plots were chosen as cells grown on the bare bottom of 96-well culture plates without CNTs. According to these plots, MSCs from P0 passage not only had the highest capacity of viability both on non-coated and collagen coated patterned CNT surfaces, but also higher than the control groups (Figure 52). However, as the cells from later passage series (P1 and P2) were seeded on the both coated and non-coated surfaces, the cell viability was drastically decreased even it was lower than the control group. Thus, this suggested that either non-coated or collagen coated patterned CNT arrays would be used for suitable ECM to grow cells on from early passages (P0). This should be remembered when scaffolds comprised of CNTs would be used for seeding cells. This may have important regenerative medicine applications.

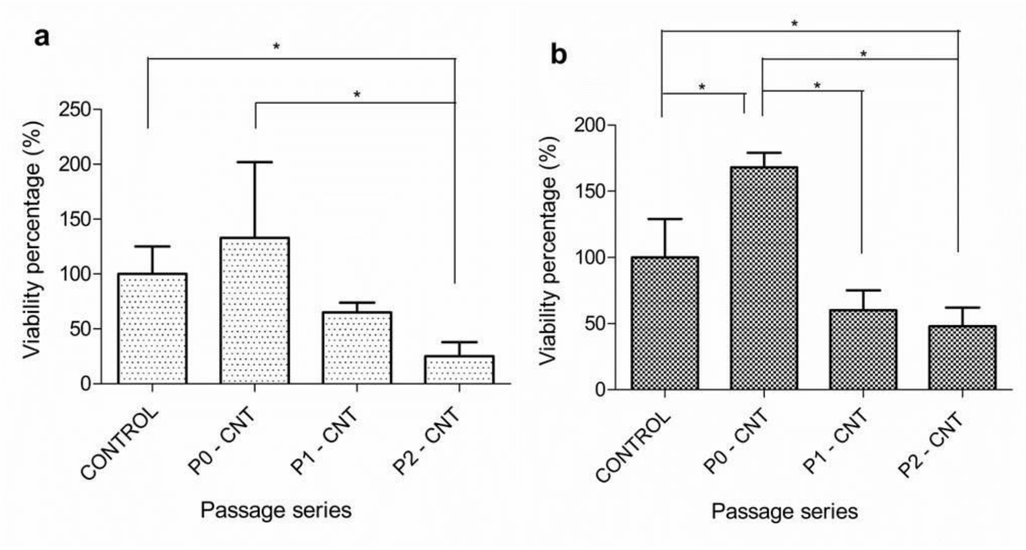

Figure 52. MTT assay plots showing the percent viability of MSCs from different passages on the (a) non-coated patterned CNTs and (b) collagen coated patterned CNTs (* indicates significant $p<0.05$.) (*194*).

The results of the count (Figure 51c) and viability (Figure 52) tests demonstrated the positive effect of CNTs which were either collagen coated or non-coated for the attachment of MSCs from the early passages (P0) while there was a negative effect on the cell adhesion in later passages (P1 and P2). The possible explanation for this observation would be the aging of MSCs as the passage number increased (*203*, *204*). In the literature, similar adversely effect of passage number on the cell viability was observed by the researchers where the mean percent senescence increased significantly with cell passaging and high passage numbers adversely affected the functioning of stem cells (*203*, *204*).

The CNT toxicity is open to discussion in the literature. While some reports were claiming toxic effect of CNTs (*205*, *206*), some were with opposite views exist (*68*, *114*, *115*). In a study by Zhu *et al.*, DNA damaged was induced by powdered form of MWCNTs (*67*) which was similar with the findings of Liu *et al.* (*207*). On the other hand, researchers found that fibroblast cells were attached and grown on the VA-CNTs without having any deleterious toxic effect if the CNTs were firmly attached to a substrate (*68*, *114*, *115*). Furthermore, there are other reports using the patterned CNTs for the growth of cells without having any toxic effects (*113*, *202*). According to the reports, it is appeared that the form of CNTs used for scaffold applications have a key role in the viability of cells. Therefore, using VA-CNTs for the ECM applications where it is firmly attached to the substrate limits the possible toxic effects besides presenting numerous anchoring points to the cells.

Chapter 5

Conclusions

In this thesis, the aim was to gain control over density and orientation of CNTs and secondly, to modulate properties of VA-CNTs during growth. Gaining control on growth of CNTs would provide new application fields by easily building 2D and 3D functional surfaces. With regards to these, the growth parameters and dynamics of VA-CNTs were investigated in this study and a summary of the important points are given below.

Firstly, the effect of catalyst layer configuration on CNT density and alignment was investigated as functions of reduction parameter and layer design. After detailed analysis of catalyst layers using SEM, AFM, HRTEM, XPS and Raman, it was found that the sandwich catalyst layer design was the best for this study to have a high density and well aligned arrays on SiO_2 substrates. In the sandwich design, the Al barrier layer was crucial to inhibit the subsurface diffusion of catalyst particles and the top Al layer acted as a pin to slow down the migration of catalyst particles during the reduction process. Furthermore, the effect of reduction step was investigated on the density and length of CNTs and it was found that there was an optimum reduction time. As a conclusion, the sandwich catalyst design would provide relatively tall, dense and well aligned CNTs.

Secondly, the parameter of reduction step was not the only one affecting the growth of VA-CNTs and thus the effect of synthesis parameters was also investigated. In this study, a morphology transition of CNTs from well aligned-straight to aligned ‘spaghetti’ like structures was achieved by varying carbon source type from alcohols to ketones. Furthermore, with the help of Raman analysis it was found that carbon source type has affected the crystallinity and defect density of VA-CNTs. The most crystalline VA-CNTs were obtained using acetone while CNTs had comparatively higher defect densities when ethanol was used. This finding was explained by the molecular structure of sources. In use of alcohols, OH group acts as an etchant and protects the surface of catalyst from poisoning while it also etches the side walls which results in defective structures. Hence, just by varying the carbon source type the quality and morphology of arrays would be tuned during the growth.

Other synthesis parameters affecting the growth of VA-CNTs were carbon source concentration and pressure inside the flow. In this study, the growth behavior of VA-CNTs was found to have a Gaussian like dependence on the ethanol pressure. Contrary to the effect of carbon source type and temperature, changes in the pressure only affected the residence time and not the decomposition process of carbon source. Thus, the increased residence time with pressure was declared as the possible reason for the growth deceleration due to the deactivation of catalyst sites with respect to increased concentration of carbonaceous species on the catalyst surface. Furthermore, the effect of carbon source concentration was investigated. In the opposite of pressure set experiments, the increased carbon concentration in the flow resulted in less contact time with the catalyst surface. As similar with pressure set results, it was found that the growth rate decreased with respect to increased carbon concentration. The possible reason was the catalyst poisoning due to the over-feeding of carbon source by increased concentration. In a conclusion, the growth of VA-CNTs followed a Gaussian like behavior rather than the continuous type due to the decreased catalytic activity by coating of excess carbon in the growth media when the residence time and concentration of carbon source were increased in this study.

In order to understand the growth mechanism of CNTs, a method of approach was developed by a combination of kinetic and diffusion related processes which were possible limitations for the growth of VA-CNTs. According to these assumptions and calculations, it was found that kinetic mechanism was responsible for the growth termination. Diffusion of feedstock gas did not show any dominant effect on the growth termination of VA-CNTs. This calculation was consistent with the experimental data where the growth rate decreased by increased residence time and carbon concentration due to decreased catalytic activity.

Thirdly, the surface properties of VA-CNTs were investigated and found that the wettability of grown VA-CNTs have been manipulated just by varying growth parameters. While super-hydrophobic VA-CNTs were obtained at 750 °C, hydrophobic surfaces were grown at 625 °C. This showed that synthesis parameters tuned the surface properties of VA-CNTs as well as their structural properties by a facile route without inducing any chemical modification. Since the cells would not prefer to attach on super-hydrophobic surfaces, VA-CNTs synthesized at 625 °C were used as scaffolds for MSCs attachment experiments. It was found that the patterned non-coated or collagen coated CNT surfaces would be used as an alternative scaffold to commercial ones for growing MSCs without encountering any toxicity. But the MSCs from P0 passage resulted in better counts on the patterned non-coated CNT surfaces than the cells from P1 and P2 passage series. The decrease in the attachment of cells by passage series was declared as the aging effect of MSCs. Moreover, collagen coating had an adverse impact on the cell adhesion. It acted as smoothing agent by filling the gaps between patterned CNTs which resulted in decrease of anchoring points required for cell adhesion. Overall, this study demonstrated that surface properties of VA-CNTs could be manipulated in a facile route during their growth and hence they could be used as patterned CNT surfaces as a scaffold for MSC growth and adhesion.

Fourth, the functionalization of VA-CNTs with Li during their growth (*in situ*) has been investigated to overcome the requirements of good conductivity, fast ion diffusion, high rate capacity and surface area. In the Li intercalation case, a charge transfer occurs to carbon lattice resulting in shifts in the spectra. Regarding to the results of XPS, EELS and Raman, the intercalation of Li inside the carbon matrix of CNTs was confirmed during their growth. The further study was also performed to intercalate Li after the growth of CNTs (*ex situ*) however; the insertion of Li inside the matrix was not achieved. As a conclusion, *in situ* Li intercalation during the growth of VA-CNTs was possible through a facile route while their alignment was preserved.

Finally, the results presented in this study can contribute to better understand the catalytic growth and mechanism of VA-CNTs using ACCVD method. The investigation of experimental parameters help to control the growth and properties of VA-CNTs for building functional surfaces to be used in future applications.

Appendixes

Appendix I

To better understand the effect of top layer Al, XPS analysis were done on the reduced and as is catalyst layers having configurations as 1nm Co/10nm Al and 0.5nm Al/1nm Co/10nm Al. The XPS spectra of catalyst layers are shown in Figure 53. The pink lines are for the layers after reduction while the black lines are for the form of layers before the reduction process. Generally, the fitting of Co peaks should be performed using Doniach-Sunjic (DS) asymmetric behavior due to the unfilled one-electron levels (conduction electrons). However, if DS fitting is used, the atomic ratios would not be the correct values because in that case extra areas will be added to the calculations due to the tails of DS fitted peaks. Hence, the fitting of Co 2p and Al 2p regions were performed using the mixture of Gaussian- Lorentizian (GL) instead of DS. In Figure 53, it is clearly observed a decrease in the counts for the Co peaks when the layers were subjected to the reduction. However, in contrast, the counts for the Al peaks were increased after the reduction process. Using the Co $2p_{3/2}$ and Al $2p_{3/2}$ peaks, the atomic ratios were calculated as in

Table 6.

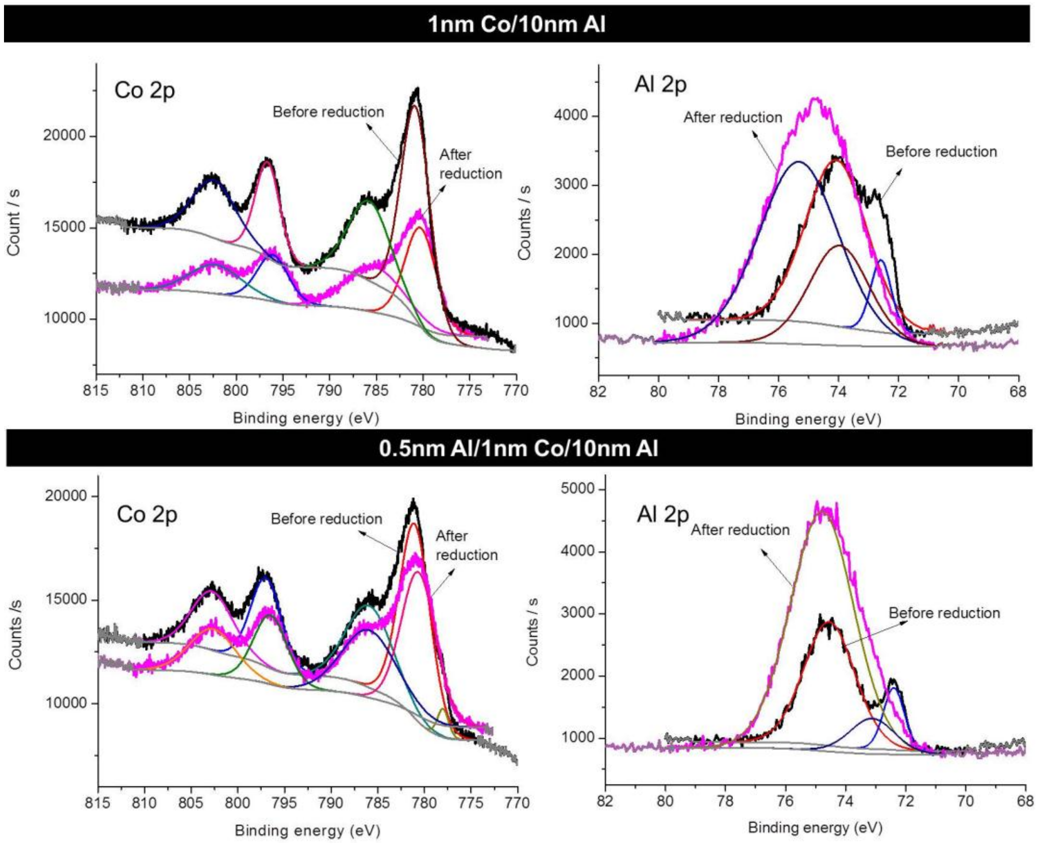

Figure 53. XPS spectra of normal design and sandwich design catalyst layers before and after reduction at 625 °C (black line indicates the layers before the reduction whereas pink line represents the spectra of catalyst layers after the reduction).

Table 6. The atomic ratio of Co/Al calculated for the designs before and after reduction process.

	Atomic ratio of Co/Al before reduction	Atomic ratio of Co/Al after reduction
Normal catalyst design	51 / 49	38 / 62
Sandwich catalyst design	74 / 26	11 / 89

Appendix II

The liquid compaction method is based on the volume shrinkage of material after contact with a liquid and dried. In this study, it was used to calculate the areal density of VA-CNTs grown on the catalyst configurations of 1nm Co/10nm Al and 0.5nm Al/1nm Co/10nm Al at 625 °C. First, the substrates with VA-CNTs were immersed into a beaker filled with deionized water and then pulled back. After the surfaces were left to dry, top view SEM images were taken. To find out the values of F, Image J program was used to pattern a mask from top view SEM images (*133*). Figure 54 shows the images after a mask was applied on the SEM images. The black areas show the places where the CNTs were compacted to a maximum area after the contact while the white ones are for the bended CNTs. Hence, the value of F is the ratio of the sum of black areas to the total image area.

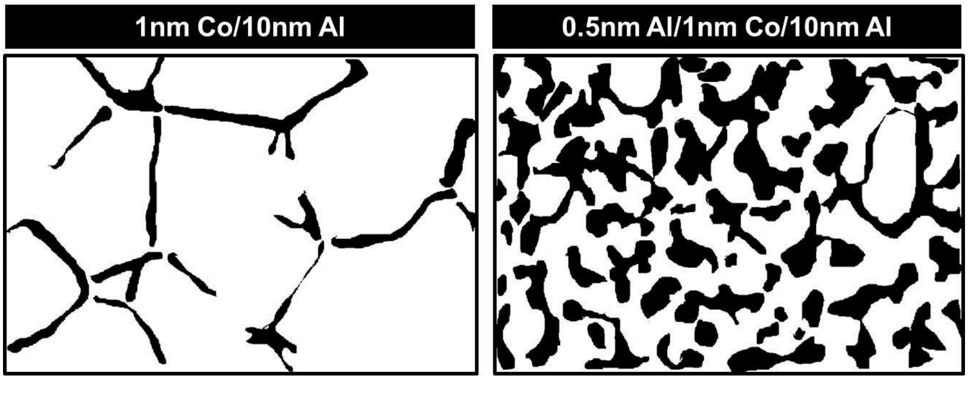

Figure 54. The images after masking to calculate the compacted areas shown by black.

$$F = \frac{Surface\ area\ after\ compaction}{Surface\ area\ of\ film}$$

Appendix III

To calculate the areal density of CNTs, firstly it is assumed that CNTs are closely packed arranged and the intertube distance (δ) is 0.34 nm which is also called as theoretical Van der Waals tube distance. As shown in Figure 55, the area signed as *A* contains one CNT arranged with a theoretical δ distance.

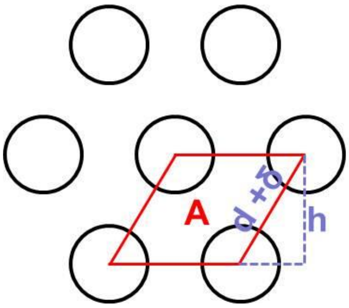

Figure 55. The proposed arrangement of CNTs on the substrate.

$$A = \frac{1}{\rho}$$

Hence, the definition of A provides a maximum density for CNTs having d diameters. Using a simple math for a trapezoid, an equation for A would be found.

$$h = (\cos 30)(d + \delta)$$

$$A = \frac{\sqrt{3}}{2}(d + \delta)^2 = \frac{1}{\rho}$$

Then, the equation for the theoretical ρ would be found as below;

$$\rho = \frac{2}{\sqrt{3}(d + \delta)^2}$$

However, it is known that the arrangement of VA-CNTs is relevant with the catalyst design. Hence, a correction factor which was *F* should be added to the theoretical equation. The value of *F* was found as shown in Appendix II. According to this correction factor, the equation for ρ is;

$$\rho = \frac{2F}{\sqrt{3}(d + \delta)^2}$$

The value of *d* was found to be around 7 nm for CNTs grown on the catalyst layers of 1nm Co/10nm Al and 0.5nm Al/1nm Co/10nm Al at 625 °C. Furthermore, the *F* values were % 10 and % 40 for the layers of 1nm Co/10nm Al and 0.5nm Al/1nm Co/10nm Al, respectively. Using these values, ρ was found to be $\sim 2\times10^{-11}$ cm^{-2} and $\sim 9\times10^{-11}$ cm^{-2} for the layers of 1nm Co/10nm Al and 0.5nm Al/1nm Co/10nm Al, respectively.

Appendix IV

Ar and H_2 gases were flowing through a bubbler containing ethanol to carry the carbon source inside the ACCVD furnace. Some of the carried ethanol was decomposed to form CNTs while the unreacted ethanol was collected at the trap cooled by liquid N_2. To find out the volumetric amount of ethanol (Q) flowed inside the furnace, the following equation is used where ΔV represents the change in the volume by time, Δt.

$$Q = \lim_{\Delta t \to 0} \frac{\Delta V}{\Delta t}$$

$$\Delta V = init. volume\ of\ ethanol - volume\ of ethanol\ inside\ the\ trap$$

Regarding to this equation, ΔV is the change in the ethanol volume at the bubbler after the growth and Δt is the total ACCVD time which is 30 minutes. The initial volume of ethanol for all experiments was kept constant at 149 mL. Using the equation, the values for Q were calculated and tabulated in the Table 7.

Table 7. Calculated values of the ethanol flow in the pressure set.

Pressure (Torr)	Left volume of ethanol at the bubbler (mL)	Calculated Q (sccm)
40	55	3.1
56	62	2.9
69	70	2.6
81	82	2.2
94	105	1.5

Appendix V

In the concentration set of experiments, the initial volume of ethanol at the bubbler was taken different than 149 mL because the carbon source does not last till the end of growth time. If the temperature of bubbler is increased, the growth will not proceed for 30 minutes. Hence, for every temperature, the initial volume of ethanol at the bubbler was changed. As shown before in Appendix IV, the volumetric amount of ethanol (*Q*) flowed inside the furnace was calculated using the change in the volume of bubbler by time. The growth lasts for 30 minutes for all experiments.

Table 8. Calculated values of the ethanol flow in the concentration set.

Temperature of ethanol at the bubbler (°C)	Pressure (Torr)	Initial volume of ethanol at the bubbler (mL)	Left volume of ethanol at the bubbler (mL)	Calculated Q (sccm)
32	40	149	55	3.1
50	53	149	15	4.5
71	71	200	10	6.3
83	81	230	14	7.2

Appendix VI

MSCs both at mRNA and protein levels for P0, P1 and P2 groups were characterized after the isolation from rat bone marrow at the Department of Molecular Biology and Genetics with the help of Dr. Can Akcali's group. MSC markers (*CD90*, *CD71* and *CD29*) were positive for the cells at P0, P1 and P2 groups but negative for hematopoietic stem cell markers (*CD45* and *CD34*) for all passages as expected (Figure 56a). Furthermore, the MSCs at P0, P1 and P2 groups were positive for *CD29* and negative for *CD34* by Western Blot analysis at the protein level (Figure 56b).

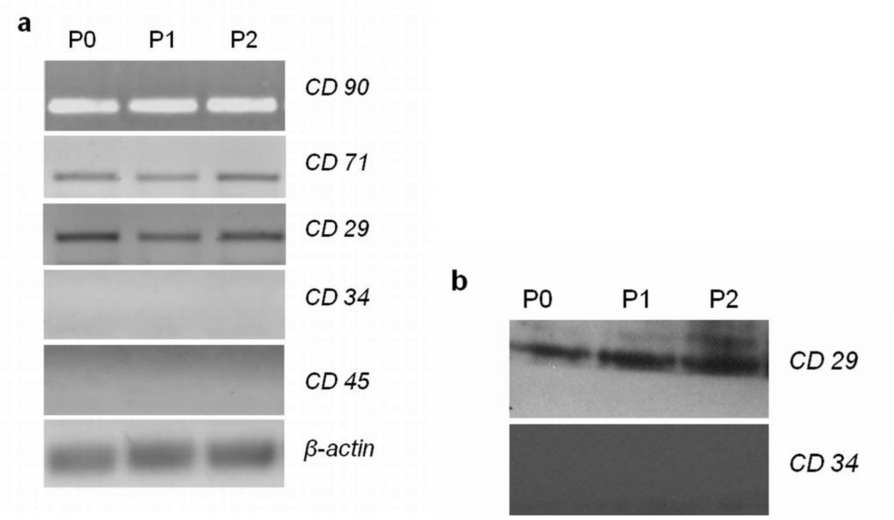

Figure 56. The expression of the markers for bone marrow derived MSCs and hematopoetic stem cells at (a) mRNA and (b) protein levels (*194*).

Appendix VII

DFT calculations for the *in situ* Li intercalation of VA-CNTs were performed by Dr. Oguz Gulseren and his co-workers using the projector-augmented-wave potentials (*208*). The details for the calculations would be found in the recent published work (*165*). A bilayer graphene system with AA (8 initial configurations) and AB (12 initial configurations) stacking having one Li atom on were used and optimized to better understand the binding of Li with CNT. Furthermore, charge densities for the proposed systems were investigated to determine the charge transfer during the intercalation using Bader analysis. All the results of the proposed systems were described in three groups; adsorption, substitution and intercalation. The calculation for the binding energy was described in the below:

$$E_{binding} = E_{total} - (E_{bi\text{-}graphene} + n_{Li}\ X\ \mu_{Li})$$

E_{total}; total energy of the relaxed composite system

$E_{bi\text{-}graphene}$; energy of graphitic system (i.e. bilayer graphene or bilayer graphene with vacancies)

n_{Li}; number of Li atoms

μ_{Li}; chemical potential of single Li atom

There were three possible adsorption sites; top (on top of a carbon atom), hollow site (above the center of a hexagon), and the bridge site (above the bond between two carbon atoms) designated as 1, 2, and 3 in Figure 57. After the systems left for the relaxation, it was found that the Li atom was ~2.2 Å away from the nearest carbon atom where a bonding occurred. The most energetically stable (the highest binding energy) system was the adsorption of Li atom sitting above the center of a hexagon with the binding energy of 2.29 eV while the other sites had binding energies of around 1.9 eV.

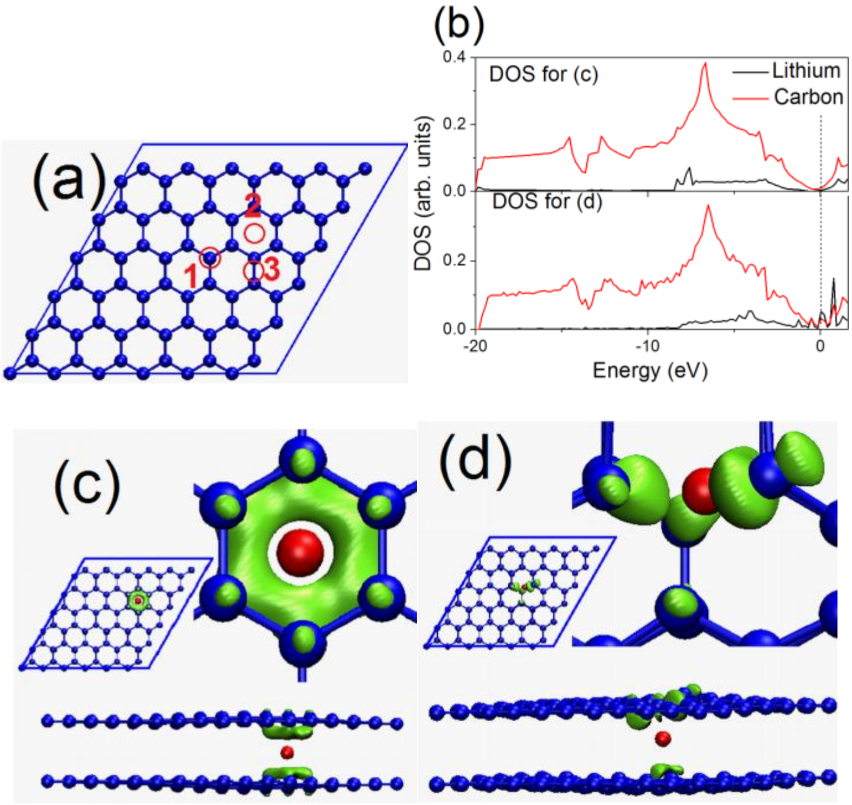

Figure 57. (a) Possible Li adsorption sites; top (1), hollow (2) and bridge (3) for 6x6 unit cell. (b) PDOS for Li intercalated cases shown in (c) and (d). Dotted line indicates the Fermi level. Top and side views of the optimized geometry and the

charge density of (c) Li intercalated bilayer graphene and (d) similar system but starting from Li substitution to a C site on top layer (*165*).

Other than adsorption systems, the substitution geometries were also conducted by replacing one carbon atom with Li atom at the hexagon. In this case, very strong bonds of C-C and Li-C were present; 1.42 Å for C-C and 2.2 Å for Li-C. In the case of double carbon vacancy on graphene system, it was found that Li atom was introduced and after the relaxation of system, it was situated between the graphene layers. Hence, the length of Li-C was around 2.2 Å in the defective graphene and the binding energy was 3.54 eV and 3.29 eV for single and double carbon vacancy cases, respectively. Furthermore, the position of Li atom was checked when left between the graphene layers. Hence, it was found that Li placed on a hollow site and Li-C length was around 2.2 Å whereas the binding energy was ~3.01eV.

Even, the highest energies were found for the substituted Li cases as a result of binding energy calculations, they were not correct since the energies were calculated with respect to defective graphene systems. Thus, the calculations indicated that Li energetically preferred to be between two graphene layers where Li was at *mid hollow* site as shown in Figure. The binding energies, Li-C bond distances, and total charge transfer from Li to carbon network were listed in the table below.

As mentioned before, the charge transfer from Li to the graphene system was calculated using the Bader Analysis. In order to calculate the charge transfer accurately, ten times denser grids were used than the common ones and the difference of charges before and after Li intercalation around each atom was counted. Finally, it was found that almost 0.86 electrons were passed from the Li atom to the nearest carbon atom while it was leaving a positively charged Li core behind. In the case of perfect intercalation case, an electron coming from the Li atom was shared symmetrically by carbon atoms as shown in Figure 57c. However, for the case of intercalation in defective systems, the extra charge was placed more around the missing C atoms to compensate the dangling bonds (Figure 57d).

Table 9. Binding energies, Li-C bond distances, and total charge transfer from Li to C network for Li doped AA stacking bilayer resulted from LDA calculations (*165*).

Adsorption geometry	Binding energy (eV)	Li-C bond distance (Å)	Total charge transferred to carbon atoms (e)
Outer top	1.93	1.99	0.9
Outer bridge	1.96	2.08	0.9
Outer hollow	2.29	2.21	0.88
Mid top	2.6	2.01	0.84
Mid bridge	2.63	2.09	0.84
Mid hollow	3.01	2.3	0.85
Substituted: Single C vacancy	3.54	2.27	0.84
Substituted: Double C vacancy	3.29	2.12	0.86

Bibliography

(1) Iijima, S. Helical microtubules of graphitic carbon. *Nature* **1991**, *354*, 56–58.

(2) V.M. Lukyanovich, L. V. R. CNT ilk paper.pdf. *Zurn Fisic Chim* **1952**, *26*, 88–95.

(3) Oberlin, A. Carbonization and graphitization. *Carbon* **1984**, *22*, 521–541.

(4) Tibbetts, G. G. Why are carbon filaments tubular? *Journal of Crystal Growth* **1984**, *66*, 632–638.

(5) Angus, J. C.; Hayman, C. C. Low-pressure, metastable growth of diamond and “Diamondlike ” phases. *Science* **1988**, *241*, 913–921.

(6) Chai, Y.; Cuo, T.; Jin, C.; Hauflerj, R. E.; Chibante, L. P. F.; Fure, J.; Wang, L.; Alford, J. M.; Smalley, R. E. Fullerenes with metals inside. *Journal of Physical Chemistry* **1991**, *95*, 7564–7568.

(7) Novoselov, K. S.; Geim, A. K.; Morozov, S. V.; Jiang, D.; Zhang, Y.; Dubonos, S. V.; Grigorieva, I. V.; Firsov, A. A. Electric field effect in atomically thin carbon films. *Science* **2004**, *306*, 666–669.

(8) Hata, K.; Futaba, D. N.; Mizuno, K.; Namai, T.; Yumura, M.; Iijima, S. Water-assisted highly efficient synthesis of impurity-free single-walled carbon nanotubes. *Science* **2004**, *306*, 1362–1364.

(9) Nishino, H.; Yasuda, S.; Namai, T.; Futaba, D. N.; Yamada, T.; Yumura, M.; Iijima, S.; Hata, K. Water-assisted highly efficient synthesis of single-walled carbon nanotubes forests from colloidal nanoparticle catalysts. *Journal of Physical Chemistry C* **2007**, *111*, 17961–17965.

(10) Cui, X.; Wei, W.; Chen, W. Lengthening and thickening of multi-walled carbon nanotube arrays grown by chemical vapor deposition in the presence and absence of water. *Carbon* **2010**, *48*, 2782–2791.

(11) Sugime, H.; Noda, S. Millimeter-tall single-walled carbon nanotube forests grown from ethanol. *Carbon* **2010**, *48*, 2203–2211.

(12) Zhang, Y.; Gregoire, J. M.; Dover, R. B. V.; Hart, A. J. Ethanol-promoted high-yield growth of few-walled carbon nanotubes. *Journal of Physical Chemistry C* **2010**, *114*, 6389–6395.

(13) Bradford, P. D.; Wang, X.; Zhao, H.; Maria, J.-P.; Jia, Q.; Zhu, Y. T. A novel approach to fabricate high volume fraction nanocomposites with long aligned carbon nanotubes. *Composites Science and Technology* **2010**, *70*, 1980–1985.

(14) Ebbesen, T. W.; Ajayan, P. M. Large scale synthesis of carbon nanotubes. *Nature* **1992**, *358*, 220–221.

(15) Odom, T. W.; Huang, J.-L.; Kim, P.; Lieber, C. M. Atomic structure and electronic properties of single-walled carbon nanotubes. *Nature* **1997**, *391*, 62–64.

(16) Robertson, J. Diamond-like amorphous carbon. *Materials Science and Engineering R* **2002**, *37*, 129–281.

(17) Ferrari, A. C. Raman spectroscopy of graphene and graphite: Disorder, electron–phonon coupling, doping and nonadiabatic effects. *Solid State Communications* **2007**, *143*, 47–57.

(18) Donato, M. G.; Messina, G.; Santangelo, S.; Galvagno, S.; Milone, C.; Pistone, A. Aid of Raman spectroscopy in diagnostics of MWCNT synthesised by Fe-catalysed CVD. *Journal of Physics: Conference Series* **2007**, *61*, 931–935.

(19) Kim, Y. A.; Hayashi, T.; Osawa, K.; Dresselhaus, M. S.; Endo, M. Annealing effect on disordered multi-wall carbon nanotubes. *Chemical Physics Letters* **2003**, *380*, 319–324.

(20) Wu, G.; Yang, X.; Dong, J. Radial breathinglike mode of the collapsed single-walled carbon nanotube bundle under hydrostatic pressure. *Applied Physics Letters* **2006**, *88*, 223114.

(21) Rols, S.; Righi, A.; Alvarez, L.; Anglaret, E.; Almairac, R.; Journet, C.; Bernier, P.; Sauvajol, J. L. Diameter distribution of single wall carbon

nanotubes in nanobundles. *The European Physical Journal B* **2000**, *18*, 201–205.

(22) Jorio, A.; Saito, R.; Hafner, J.; Lieber, C.; Hunter, M.; McClure, T.; Dresselhaus, G.; Dresselhaus, M. Structural (n, m) determination of isolated single-wall carbon nanotubes by resonant Raman scattering. *Physical Review Letters* **2001**, *86*, 1118–1121.

(23) McGuire, K.; Gothard, N.; Gai, P. L.; Dresselhaus, M. S.; Sumanasekera, G.; Rao, A. M. Synthesis and Raman characterization of boron-doped single-walled carbon nanotubes. *Carbon* **2005**, *43*, 219–227.

(24) Chen, C. F.; Tsai, C. L.; Lin, C. L. The characterization of boron-doped carbon nanotube arrays. *Diamond and Related Materials* **2003**, *12*, 1500–1504.

(25) Ayala, P.; Arenal, R.; Rümmeli, M.; Rubio, a.; Pichler, T. The doping of carbon nanotubes with nitrogen and their potential applications. *Carbon* **2010**, *48*, 575–586.

(26) Frank, S. Carbon nanotube quantum resistors. *Science* **1998**, *280*, 1744–1746.

(27) Maciel, I. O.; Campos-Delgado, J.; Pimenta, M. A.; Terrones, M.; Terrones, H.; Rao, A. M.; Jorio, A. Boron, nitrogen and phosphorous

substitutionally doped single-wall carbon nanotubes studied by resonance Raman spectroscopy. *Physica Status Solidi B* **2009**, *246*, 2432–2435.

(28) Hsieh, C.-T.; Lin, Y.-T.; Lin, J.-Y.; Wei, J.-L. Synthesis of carbon nanotubes over Ni- and Co-supported CaCO3 catalysts using catalytic chemical vapor deposition. *Materials Chemistry and Physics* **2009**, *114*, 702–708.

(29) Colomer, J.; Stephan, C.; Lefrant, S.; Van Tendeloo, G.; Willems, I. Large-scale synthesis of single-wall carbon nanotubes by catalytic chemical vapor deposition (CCVD) method. *Chemical Physics Letters* **2000**, *317*, 83–89.

(30) Zhong, G.; Hofmann, S.; Yan, F.; Telg, H.; Warner, J. H.; Eder, D.; Thomsen, C.; Milne, W. I.; Robertson, J. Acetylene: A Key Growth Precursor for Single-Walled Carbon Nanotube Forests. *The Journal of Physical Chemistry C* **2009**, *113*, 17321–17325.

(31) Hernadi, K.; Fonseca, A.; Nagy, J. B.; Siska, A.; Kiricsi, I. Production of nanotubes by the catalytic decomposition of different carbon-containing compounds. *Applied Catalysis A: General* **2000**, *199*, 245–255.

(32) Nikolaev, P.; Bronikowski, M. J.; Bradley, R. K.; Rohmund, F.; Colbert, D. T.; Smith, K. A.; Smalley, R. E. Gas-phase catalytic growth of single-walled carbon nanotubes from carbon monoxide. *Chemical Physics Letters* **1999**, *313*, 91–97.

(33) Ortega-Cervantez, G.; Rueda-Morales, G.; Ortiz-López, J. Catalytic CVD production of carbon nanotubes using ethanol. *Microelectronics Journal* **2005**, *36*, 495–498.

(34) Kohno, M.; Orii, T.; Hirasawa, M.; Seto, T.; Murakami, Y.; Chiashi, S.; Miyauchi, Y.; Maruyama, S. Growth of single-walled carbon nanotubes from size-selected catalytic metal particles. *Applied Physics A* **2004**, *79*, 787–790.

(35) Li, Q.; Yan, H.; Zhang, J.; Liu, Z. Effect of hydrocarbons precursors on the formation of carbon nanotubes in chemical vapor deposition. *Carbon* **2004**, *42*, 829–835.

(36) Vm, S.; Mohamed, A. R.; Abdullah, A. Z.; Chai, S.-P. Role of reaction and factors of carbon nanotubes growth in chemical vapour decomposition process using methane—A highlight. *Journal of Nanomaterials* **2010**, *2010*, 1–11.

(37) Huang, Z. P.; Wang, D. Z.; Wen, J. G.; Sennett, M.; Gibson, H.; Ren, Z. F. Effect of nickel, iron and cobalt on growth of aligned carbon nanotubes. *Applied Physics A* **2002**, *74*, 387–391.

(38) Cantoro, M.; Hofmann, S.; Pisana, S.; Ducati, C.; Parvez, a.; Ferrari, a. C.; Robertson, J. Effects of pre-treatment and plasma enhancement on chemical vapor deposition of carbon nanotubes from ultra-thin catalyst films. *Diamond and Related Materials* **2006**, *15*, 1029–1035.

(39) Xu, X.; Huang, S.; Hu, Y.; Lu, J.; Yang, Z. Continuous synthesis of carbon nanotubes using a metal-free catalyst by CVD. *Materials Chemistry and Physics* **2012**, *133*, 95–102.

(40) Zhu, J.; Jia, J.; Kwong, F.; Ng, D. H. L.; Crozier, P. A. Metal-free synthesis of carbon nanotubes filled with calcium silicate. *Carbon* **2012**, *50*, 2666–2669.

(41) Futaba, D. N.; Goto, J.; Yasuda, S.; Yamada, T.; Yumura, M.; Hata, K. A background level of oxygen-containing aromatics for synthetic control of carbon nanotube structure. *Journal of the American Chemical Society* **2009**, *131*, 15992–15993.

(42) Murakami, Y. Growth of vertically aligned single-walled carbon nanotube films on quartz substrates and their optical anisotropy. *Chemical Physics Letters* **2004**, *385*, 298–303.

(43) Emmenegger, C.; Bonard, J.; Mauron, P.; Lepora, A. Synthesis of carbon nanotubes over Fe catalyst on aluminium and suggested growth mechanism. *Carbon* **2003**, *41*, 539–547.

(44) Moisala, A.; Nasibulin, A. G.; Kauppinen, E. I. The role of metal nanoparticles in the catalytic production of single-walled carbon nanotubes — a review. *Journal of Physics: Condensed Matter* **2003**, *15*, S3011–S3035.

(45) Veziri, C. M.; Karanikolos, G. N.; Pilatos, G.; Vermisoglou, E. C.; Giannakopoulos, K.; Stogios, C.; Kanellopoulos, N. K. Growth and morphology manipulation of carbon nanostructures on porous supports. *Carbon* **2009**, *47*, 2161–2173.

(46) Sigurdson, S.; Sundaramurthy, V.; Dalai, a. K.; Adjaye, J. Effect of anodic alumina pore diameter variation on template-initiated synthesis of carbon nanotube catalyst supports. *Journal of Molecular Catalysis A: Chemical* **2009**, *306*, 23–32.

(47) Matthews, K. D.; Lemaitre, M. G.; Kim, T.; Chen, H.; Shim, M.; Zuo, J.-M. Growth modes of carbon nanotubes on metal substrates. *Journal of Applied Physics* **2006**, *100*, 044309.

(48) Yudasaka, M.; Zhang, M.; Iijima, S. Porous target enhances production of single-wall carbon nanotubes by laser ablation. *Chemical Physics Letters* **2000**, *323*, 549–553.

(49) Scott, C. D.; Arepalli, S.; Nikolaev, P.; Smalley, R. E. Growth mechanisms for single-wall carbon nanotubes in a laser-ablation process. *Applied Physics A* **2001**, *72*, 573–580.

(50) Journet, C.; Maser, W. K.; Bernier, P.; Loiseau, A. Large-scale production of single-walled carbon nanotubes by the electric-arc technique. *Nature* **1997**, *388*, 756–758.

(51) Zhao, X. Macroscopic oriented web of single-wall carbon nanotubes. *Chemical Physics Letters* **2003**, *373*, 266–271.

(52) Cheng, H. M.; Li, F.; Su, G.; Pan, H. Y.; He, L. L.; Sun, X.; Dresselhaus, M. S. Large-scale and low-cost synthesis of single-walled carbon nanotubes by the catalytic pyrolysis of hydrocarbons. *Applied Physics Letters* **1998**, *72*, 3282.

(53) Mahanandia, P.; Vishwakarma, P. N.; Nanda, K. K.; Prasad, V.; Barai, K.; Mondal, a. K.; Sarangi, S.; Dey, G. K.; Subramanyam, S. V. Synthesis of multi-wall carbon nanotubes by simple pyrolysis. *Solid State Communications* **2008**, *145*, 143–148.

(54) Liu, B. C.; Lee, T. J.; Lee, S. H.; Park, C. Y.; Lee, C. J. Large-scale synthesis of high-purity well-aligned carbon nanotubes using pyrolysis of iron(II) phthalocyanine and acetylene. *Chemical Physics Letters* **2003**, *377*, 55–59.

(55) Rao, C. N. R.; Govindaraj, A. Carbon nanotubes from organometallic precursors. *Accounts of Chemical Research* **2002**, *35*, 998–1007.

(56) Wagner, R. S.; Ellis, W. C. Vapor-liquid-solid mechanism of single crystal growth. *Applied Physics Letters* **1964**, *4*, 89–90.

(57) Liu, K.; Jiang, K.; Feng, C.; Chen, Z.; Fan, S. A growth mark method for studying growth mechanism of carbon nanotube arrays. *Carbon* **2005**, *43*, 2850–2856.

(58) Chhowalla, M.; Teo, K. B. K.; Ducati, C.; Rupesinghe, N. L.; Amaratunga, G. A. J.; Ferrari, A. C.; Roy, D.; Robertson, J.; Milne, W. I. Growth process conditions of vertically aligned carbon nanotubes using plasma enhanced chemical vapor deposition. *Journal of Applied Physics* **2001**, *90*, 5308–5317.

(59) Wirth, C. T.; Zhang, C.; Zhong, G.; Hofmann, S.; Robertson, J. Diffusion and reaction limited growth of carbon nanotube forests. *ACS Nano* **2009**, *3*, 3560–3566.

(60) Xiang, R.; Yang, Z.; Zhang, Q.; Luo, G.; Qian, W.; Wei, F.; Kadowaki, M.; Einarsson, E.; Maruyama, S. Growth deceleration of vertically aligned carbon nanotube arrays: Catalyst deactivation or feedstock diffusion controlled? *Journal of Physical Chemistry C* **2008**, *112*, 4892–4896.

(61) Dijon, J.; Szkutnik, P. D.; Fournier, a.; Goislard de Monsabert, T.; Okuno, H.; Quesnel, E.; Muffato, V.; De Vito, E.; Bendiab, N.; Bogner, a.; Bernier, N. How to switch from a tip to base growth mechanism in carbon nanotube growth by catalytic chemical vapour deposition. *Carbon* **2010**, *48*, 3953–3963.

(62) Song, I. K.; Yu, W. J.; Cho, Y. S.; Choi, G. S.; Kim, D. The determining factors for the growth mode of carbon nanotubes in the chemical vapour deposition process. *Nanotechnology* **2004**, *15,* S590–S595.

(63) Anderson, P. E.; Rodriguez, N. M. Influence of the support on the structural characteristics of carbon nanofibers produced from the metal-catalyzed decomposition of ethylene. *Chemistry of Materials* **2000**, *12*, 823–830.

(64) Mattevi, C.; Wirth, C. T.; Hofmann, S.; Blume, R.; Cantoro, M.; Ducati, C.; Cepek, C.; Knop-Gericke, A.; Milne, S.; Castellarin-Cudia, C.; Dolafi, S.; Goldoni, A.; Schloegl, R.; Robertson, J. In-situ X-ray photoelectron spectroscopy study of catalyst−support interactions and growth of carbon nanotube forests. *Journal of Physical Chemistry C* **2008**, *112*, 12207–12213.

(65) Cao, Q.; Hur, S.-H.; Zhu, Z.-T.; Sun, Y. G.; Wang, C.-J.; Meitl, M. A.; Shim, M.; Rogers, J. A. Highly bendable, transparent thin-film transistors that use carbon-nanotube-based conductors and semiconductors with elastomeric dielectrics. *Advanced Materials* **2006**, *18*, 304–309.

(66) Ishikawa, F. N.; Chang, H.; Ryu, K.; Chen, P.; Badmaev, A.; Gomez, L.; Arco, D.; Shen, G.; Zhou, C. Transparent electronics based on transfer printed aligned carbon nanotubes on rigid and flexible substrates. *ACS Nano* **2009**, *3*, 73–79.

(67) Zhu, L.; Chang, D. W.; Dai, L.; Hong, Y. DNA damage induced by multiwalled carbon nanotubes in mouse embryonic stem cells. *Nano letters* **2007**, *7*, 3592–3597.

(68) Lobo, a. O.; Corat, M. a. F.; Antunes, E. F.; Palma, M. B. S.; Pacheco-Soares, C.; Garcia, E. E.; Corat, E. J. An evaluation of cell proliferation and adhesion on vertically-aligned multi-walled carbon nanotube films. *Carbon* **2010**, *48*, 245–254.

(69) Huczko, A. Synthesis of aligned carbon nanotubes. *Applied Physics A: Materials Science & Processing* **2002**, *74*, 617–638.

(70) Seah, C.-M.; Chai, S.-P.; Mohamed, A. R. Synthesis of aligned carbon nanotubes. *Carbon* **2011**, *49*, 4613–4635.

(71) Xiao, J.; Dunham, S.; Liu, P.; Zhang, Y.; Kocabas, C.; Moh, L.; Huang, Y.; Hwang, K.-C.; Lu, C.; Huang, W.; Rogers, J. A. Alignment controlled growth of single-walled carbon nanotubes on quartz substrates. *Nano letters* **2009**, *9*, 4311–4319.

(72) Ma, Y.; Wang, B.; Wu, Y.; Huang, Y.; Chen, Y. The production of horizontally aligned single-walled carbon nanotubes. *Carbon* **2011**, *49*, 4098–4110.

(73) Li, W. Z.; Xie, S. S.; Qian, L. X.; Chang, B. H.; Zou, B. S.; Zhou, W. Y.; Zhao, R. A.; Wang, G. Large-scale synthesis of aligned carbon nanotubes. *Science* **1996**, *274*, 1701–1703.

(74) Futaba, D. N.; Hata, K.; Namai, T.; Yamada, T.; Mizuno, K.; Hayamizu, Y.; Yumura, M.; Iijima, S. 84% Catalyst activity of water-assisted growth of single walled carbon nanotube forest characterization by a statistical and macroscopic approach. *The journal of physical chemistry. B* **2006**, *110*, 8035–8038.

(75) Futaba, D.; Hata, K.; Yamada, T.; Mizuno, K.; Yumura, M.; Iijima, S. Kinetics of water-assisted single-walled carbon nanotube synthesis revealed by a time-evolution analysis. *Physical Review Letters* **2005**, *95*, 056104 –1–4.

(76) Yoshihara, N.; Ago, H.; Tsuji, M. Chemistry of water-assisted carbon nanotube growth over Fe-Mo / MgO catalyst. *Journal of Physical Chemistry C* **2007**, *111*, 11577–11582.

(77) Nasibulin, A. G.; Brown, D. P.; Queipo, P.; Gonzalez, D.; Jiang, H.; Kauppinen, E. I. An essential role of CO2 and H2O during single-walled carbon nanotube synthesis from carbon monoxide. *Chemical Physics Letters* **2006**, *417*, 179–184.

(78) Wen, Q.; Qian, W.; Wei, F.; Ning, G. Oxygen-assisted synthesis of SWNTs from methane decomposition. *Nanotechnology* **2007**, *18*, 215610–1–7.

(79) Pint, C. L.; Pheasant, S. T.; Parra-Vasquez, A. N. G.; Horton, C.; Xu, Y.; Hauge, R. H. Investigation of optimal parameters for oxide-assisted growth of vertically aligned single-walled carbon nanotubes. *The Journal of Physical Chemistry C* **2009**, *113*, 4125–4133.

(80) Yu, G.; Gong, J.; Wang, S.; Zhu, D.; He, S.; Zhu, Z. Etching effects of ethanol on multi-walled carbon nanotubes. *Carbon* **2006**, *44*, 1218–1224.

(81) Maruyama, S.; Kojima, R.; Miyauchi, Y.; Chiashi, S.; Kohno, M. Low-temperature synthesis of high-purity single-walled carbon nanotubes from alcohol. *Chemical Physics Letters* **2002**, *360*, 229–234.

(82) Oida, S.; Sakai, A.; Nakatsuka, O.; Ogawa, M.; Zaima, S. Effect of alcohol sources on synthesis of single-walled carbon nanotubes. *Applied Surface Science* **2008**, *254*, 7697–7702.

(83) Liu, W.-W.; Aziz, A.; Chai, S.-P.; Mohamed, A. R.; Tye, C.-T. The effect of carbon precursors (methane, benzene and camphor) on the quality of carbon nanotubes synthesised by the chemical vapour decomposition. *Physica E* **2011**, *43*, 1535–1542.

(84) Montoro, L. A.; Corio, P.; Rosolen, J. M. A comparative study of alcohols and ketones as carbon precursor for multi-walled carbon nanotube growth. *Carbon* **2007**, *45*, 1234–1241.

(85) Botello-Méndez, A.; Campos-Delgado, J.; Morelos-Gómez, A.; Romo-Herrera, J. M.; Rodríguez, Á. G.; Navarro, H.; Vidal, M. A.; Terrones, H.; Terrones, M. Controlling the dimensions, reactivity and crystallinity of multiwalled carbon nanotubes using low ethanol concentrations. *Chemical Physics Letters* **2008**, *453*, 55–61.

(86) Mathur, A.; Roy, S. S.; Dickinson, C.; McLaughlin, J. A. Effect of thin aluminum interlayer on growth and microstructure of carbon nanotubes. *Current Applied Physics* **2010**, *10*, 407–410.

(87) Teng, F.-Y.; Ting, J.-M.; Sharma, S. P.; Liao, K.-H. Growth of CNTs on Fe-Si catalyst prepared on Si and Al coated Si substrates. *Nanotechnology* **2008**, *19*, 095607–1–6.

(88) Burt, D. P.; Whyte, W. M.; Weaver, J. M. R.; Glidle, A.; Edgeworth, J. P.; Macpherson, J. V.; Dobson, P. S. Effects of metal underlayer grain size on carbon nanotube growth. *The Journal of Physical Chemistry C* **2009**, *113*, 15133–15139.

(89) Terrado, E.; Redrado, M.; Muñoz, E.; Maser, W. K.; Benito, a. M.; Martínez, M. T. Aligned carbon nanotubes grown on alumina and quartz

substrates by a simple thermal CVD process. *Diamond and Related Materials* **2006**, *15*, 1059–1063.

(90) Tsai, T.-Y.; Tai, N.-H.; Chen, K. C.; Lee, S. H.; Chan, L. H.; Chang, Y. Y. Growth of vertically aligned carbon nanotubes on glass substrate at 450 °C through the thermal chemical vapor deposition method. *Diamond and Related Materials* **2009**, *18*, 307–311.

(91) McNicholas, T. P.; Ding, L.; Yuan, D.; Liu, J. Density enhancement of aligned single-walled carbon nanotube thin films on quartz substrates by sulfur-assisted synthesis. *Nano letters* **2009**, *9*, 3646–50.

(92) de los Arcos, T.; Gunnar Garnier, M.; Oelhafen, P.; Mathys, D.; Won Seo, J.; Domingo, C.; Vicente García-Ramos, J.; Sánchez-Cortés, S. Strong influence of buffer layer type on carbon nanotube characteristics. *Carbon* **2004**, *42*, 187–190.

(93) Kim, N. S.; Lee, Y. T.; Park, J.; Ryu, H.; Lee, H. J.; Choi, S. Y.; Choo, J. Dependence of the vertically aligned growth of carbon nanotubes on the catalysts. *The Journal of Physical Chemistry B* **2002**, *106*, 9286–9290.

(94) Ago, H.; Nakamura, Y.; Ogawa, Y.; Tsuji, M. Combinatorial catalyst approach for high-density growth of horizontally aligned single-walled carbon nanotubes on sapphire. *Carbon* **2011**, *49*, 176–186.

(95) Murakami, T.; Mitikami, K.; Ishigaki, S.; Matsumoto, K.; Nishio, K.; Isshiki, T.; Harima, H.; Kisoda, K. Catalytic mechanism of a Fe–Co bimetallic system for efficient growth of single-walled carbon nanotubes on Si∕SiO2 substrates. *Journal of Applied Physics* **2006**, *100*, 094303–1–4.

(96) Zhou, W.; Ding, L.; Liu, J. Role of catalysts in the surface synthesis of single-walled carbon nanotubes. *Nano Research* **2009**, *2*, 593–598.

(97) Li, C.-S.; Su, S.-H.; Chi, H.-Y.; Yokoyama, M. Application of highly ordered carbon nanotubes templates to field-emission organic light-emitting diodes. *Journal of Crystal Growth* **2009**, *311*, 615–618.

(98) Yilmazoglu, O.; Popp, A.; Pavlidis, D.; Schneider, J. J.; Garth, D.; Schüttler, F.; Battenberg, G. Vertically aligned multiwalled carbon nanotubes for pressure, tactile and vibration sensing. *Nanotechnology* **2012**, *23*, 085501–1–8.

(99) Basirico, L.; Lanzara, G. Moving towards high-power, high-frequency and low-resistance CNT supercapacitors by tuning the CNT length, axial deformation and contact resistance. *Nanotechnology* **2012**, *23*, 305401–1–13.

(100) Yuan, Y.; Smith, J. A.; Goenaga, G.; Liu, D.-J.; Luo, Z.; Liu, J. Platinum decorated aligned carbon nanotubes: Electrocatalyst for improved

performance of proton exchange membrane fuel cells. *Journal of Power Sources* **2011**, *196*, 6161–6167.

(101) Tae, Y.; Seung, C.; Sun, Y. Improved electrochemical performance of Li-doped natural graphite anode for lithium secondary batteries. *Journal of Power sources* **2005**, *139*, 230–234.

(102) Maurin, G.; Henn, F.; Simon, B.; Colomer, J.; Nagy, J. B. Lithium doping of multiwalled carbon nanotubes produced by catalytic decomposition. *Nano Letters* **2001**, *1*, 75–79.

(103) Yang, Z.; Wu, H. The electrochemical impedance measurements of carbon nanotubes. *Chemical Physics Letters* **2001**, *343*, 235–240.

(104) Welna, D. T.; Qu, L.; Taylor, B. E.; Dai, L.; Durstock, M. F. Vertically aligned carbon nanotube electrodes for lithium-ion batteries. *Journal of Power Sources* **2011**, *196*, 1455–1460.

(105) Okada, S.; Saito, S.; Oshiyama, A. Energetics and electronic structures of encapsulated C60 in a carbon nanotube. *Physical Review Letters* **2001**, *86*, 3835–3838.

(106) Gohier, A.; Laïk, B.; Kim, K.; Maurice, J. High-rate capability silicon decorated vertically aligned carbon nanotubes for Li-ion batteries. *Advanced Materials* **2012**, *24*, 2592–2597.

(107) Evanoff, K.; Khan, J.; Balandin, A. A.; Magasinski, A.; Ready, W. J.; Fuller, T. F.; Yushin, G. Towards ultrathick battery electrodes : Aligned carbon nanotube – enabled architecture. *Advanced Materials* **2012**, *24*, 533–537.

(108) Kim, B.; Chung, H.; Chu, K. S.; Yoon, H. G.; Lee, C. J.; Kim, W. Synthesis of vertically-aligned carbon nanotubes on stainless steel by water-assisted chemical vapor deposition and characterization of their electrochemical properties. *Synthetic Metals* **2010**, *160*, 584–587.

(109) Ma, P. X. Biomimetic materials for tissue engineering. *Advanced Drug Delivery Reviews* **2008**, *60*, 184–98.

(110) Li, W.; Tuli, R.; Huang, X.; Laquerriere, P.; Tuan, R. S. Multilineage differentiation of human mesenchymal stem cells in a three-dimensional nanofibrous scaffold. *Biomaterials* **2005**, *26*, 5158–5166.

(111) Hirata, E.; Uo, M.; Takita, H.; Akasaka, T.; Watari, F.; Yokoyama, A. Multiwalled carbon nanotube-coating of 3D collagen scaffolds for bone tissue engineering. *Carbon* **2011**, *49*, 3284–3291.

(112) Correa-duarte, M. A.; Wagner, N.; Morsczeck, C.; Thie, M.; Giersig, M. Fabrication and biocompatibility of carbon nanotube-based 3D networks as scaffolds for cell seeding and growth. *Nano Letters* **2004**, 28–31.

(113) Zhang, X.; Prasad, S.; Niyogi, S.; Morgan, A.; Ozkan, M.; Ozkan, C. Guided neurite growth on patterned carbon nanotubes. *Sensors and Actuators B* **2005**, *106*, 843–850.

(114) Giannona, S.; Firkowska, I.; Rojas-Chapana, J.; Giersig, M. Vertically aligned carbon nanotubes as cytocompatible material for enhanced adhesion and proliferation of osteoblasts-like cells. *Journal of Nanoscience and Nanotechnology* **2007**, *7,* 1679–1683.

(115) Lobo, A. O.; Antunes, E. F.; Machado, A. H. A.; Pacheco-soares, C. Cell viability and adhesion on as grown multi-wall carbon nanotube films. *Materials Science and Engineering C* **2008**, *28*, 264–269.

(116) Amama, P. B.; Pint, C. L.; Kim, S. M.; Mcjilton, Ḱ. L.; Eyink, K. G.; Stach, E. A.; Hauge, R. H.; Maruyama, B. Influence of alumina type on the evolution and activity of alumina- supported Fe catalysts in single-walled carbon nanotube carpet growth. *ACS Nano* **2010**, *4*, 895–904.

(117) Sakurai, S.; Nishino, H.; Futaba, D. N.; Yasuda, S.; Yamada, T.; Maigne, A.; Matsuo, Y.; Nakamura, E.; Yumura, M.; Hata, K. Role of subsurface diffusion and Ostwald ripening in catalyst formation for single-walled carbon nanotube forest growth. *Journal of the American Chemical Society* **2012**, *134*, 2148–53.

(118) Lee, H. C.; Alegaonkar, P. S.; Kim, D. Y.; Lee, J. H.; Yoo, J. B. Growth of carbon nanotubes: effect of Fe diffusion and oxidation. *Philosophical Magazine Letters* **2007**, *87*, 767–780.

(119) Murakami, Y.; Miyauchi, Y.; Chiashi, S.; Maruyama, S. Direct synthesis of high-quality single-walled carbon nanotubes on silicon and quartz substrates. *Chemical Physics Letters* **2003**, *377*, 49–54.

(120) Lee, C. J.; Kim, D. W.; Lee, T. J.; Choi, Y. C.; Park, Y. S.; Kim, W. S.; Lee, Y. H.; Choi, W. B.; Lee, N. S.; Kim, J. M.; Choi, Y. G.; Yu, S. C. Synthesis of uniformly distributed carbon nanotubes on a large area of Si substrates by thermal chemical vapor deposition. *Applied Physics Letters* **1999**, *75*, 1721.

(121) Fan, S. Self-Oriented Regular Arrays of Carbon Nanotubes and Their Field Emission Properties. *Science* **1999**, *283*, 512–514.

(122) Jin, C.; Woon, D.; Jae, T.; Chul, Y.; Soo, Y.; Hee, Y.; Bong, W.; Sung, N.; Park, G.; Min, J. Synthesis of aligned carbon nanotubes using thermal chemical vapor deposition. *Chemical Physics Letters* **1999**, *312*, 461–468.

(123) Mizuno, K.; Hata, K.; Saito, T.; Ohshima, S.; Yumura, M.; Iijima, S. Selective matching of catalyst element and carbon source in single-walled carbon nanotube synthesis on silicon substrates. *Journal of Physical Chemistry C* **2005**, *109*, 2632–2637.

(124) Dupuis, A. The catalyst in the CCVD of carbon nanotubes—a review. *Progress in Materials Science* **2005**, *50*, 929–961.

(125) Zhao, Y.; Huang, D.; Saito, Y. A temperature window for ethanol chemical vapor deposition of a carbon nanotube array catalyzed by Co particles. *Nanotechnology* **2007**, *18*, 445608–445613.

(126) Sugime, H.; Noda, S.; Maruyama, S.; Yamaguchi, Y. Multiple "optimum" conditions for Co–Mo catalyzed growth of vertically aligned single-walled carbon nanotube forests. *Carbon* **2009**, *47*, 234–241.

(127) Yoshida, H.; Shimizu, T.; Uchiyama, T.; Kohno, H.; Homma, Y.; Takeda, S. Atomic-scale analysis on the role of molybdenum in iron-catalyzed carbon nanotube growth. *Nano letters* **2009**, *9*, 3810–3815.

(128) Cantoro, M.; Hofmann, S.; Pisana, S.; Scardaci, V.; Parvez, A.; Ducati, C.; Ferrari, A. C.; Blackburn, A. M.; Wang, K.-Y.; Robertson, J. Catalytic chemical vapor deposition of single-wall carbon nanotubes at low temperatures. *Nano letters* **2006**, *6*, 1107–1112.

(129) Zhong, G.; Warner, J. H.; Fouquet, M.; Robertson, A. W.; Chen, B.; Robertson, J. Growth of ultrahigh density single-walled carbon nanotube forests by improved catalyst design. *ACS nano* **2012**, *6*, 2893–2903.

(130) Esconjauregui, S.; Fouquet, M.; Bayer, B. C.; Ducati, C.; Smajda, R.; Hofmann, S.; Robertson, J. Growth of ultrahigh density vertically aligned carbon nanotube forests for interconnects. *ACS nano* **2010**, *4*, 7431–7436.

(131) Esconjauregui, S.; Fouquet, M.; Bayer, B. C.; Ducati, C.; Robertson, J. Catalyst design for the growth of highly packed nanotube forests. *Physica Status Solidi B* **2011**, *248*, 2528–2531.

(132) Futaba, D. N.; Hata, K.; Yamada, T.; Hiraoka, T.; Hayamizu, Y.; Kakudate, Y.; Tanaike, O.; Hatori, H.; Yumura, M.; Iijima, S. Shape-engineerable and highly densely packed single-walled carbon nanotubes and their application as super-capacitor electrodes. *Nature materials* **2006**, *5*, 987–994.

(133) Rasband, W. S. Image J. *U. S. National Institutes of Health, Bethesda, Maryland, USA*.

(134) Dijon, J.; Okuno, H.; Fayolle, M.; Vo, T.; Pontcharra, J.; Acquaviva, D.; Bouvet, D.; Ionescu, A. M.; Esconjauregui, C. S.; Capraro, B.; Quesnel, E.; Robertson, J. Ultra-high density carbon nanotubes on Al-Cu for advanced Vias. *Electron Devices Meeting* **2011**, *33*, 760–763.

(135) Zhang, R. Y.; Amlani, I.; Baker, J.; Tresek, J.; Tsui, R. K. Chemical vapor deposition of single-walled carbon nanotubes using ultrathin Ni /Al film as catalyst. *Nano Letters* **2003**, *3*, 731–735.

(136) Wu, W.; Teng, F.; Ting, J. The effect of an Al underlayer on Fe – Si thin film catalysts for the improved growth of carbon nanotubes. *Carbon* **2011**, *49*, 4589–4594.

(137) Zhang, G.; Mann, D.; Zhang, L.; Javey, A.; Li, Y.; Yenilmez, E.; Wang, Q.; McVittie, J. P.; Nishi, Y.; Gibbons, J.; Dai, H. Ultra-high-yield growth of vertical single-walled carbon nanotubes: Hidden roles of hydrogen and oxygen. *Proceedings of the National Academy of Sciences of the United States of America* **2005**, *102*, 16141–16145.

(138) Pisana, S.; Cantoro, M.; Parvez, a.; Hofmann, S.; Ferrari, a. C.; Robertson, J. The role of precursor gases on the surface restructuring of catalyst films during carbon nanotube growth. *Physica E: Low-dimensional Systems and Nanostructures* **2007**, *37*, 1–5.

(139) Zhang, Y.; Zou, G.; Doorn, S. K.; Htoon, H.; Stan, L.; Hawley, M. E.; Sheehan, C. J.; Zhu, Y.; Jia, Q. Tailoring the Morphology of Carbon Nanotube Arrays : From Spinnable Forests to Undulating Foams. *ACS nano* **2009**, *3*, 2157–2162.

(140) Zhan, Z.; Zhang, Y.; Sun, G.; Zheng, L.; Liao, K. The effects of catalyst treatment on fast growth of millimeter-long multi-walled carbon nanotube arrays. *Applied Surface Science* **2011**, *257*, 7704–7708.

(141) Ohring, M. *The Materials Science of Thin Films*; 2nd ed.; Acedemic Press, 2002; pp. 87–96.

(142) Petitto, S. C.; Langell, M. a. Surface composition and structure of Co3O4 (110) and the effect of impurity segregation. *Journal of Vacuum Science & Technology A: Vacuum, Surfaces, and Films* **2004**, *22*, 1690–1696.

(143) Riva, R.; Miessner, H.; Vitali, R.; Piero, G. D. Metal – support interaction in Co/SiO2 and Co/TiO 2. *Applied Catalysis A: General* **2000**, *196*, 111–123.

(144) Girardon, J.; Lermontov, A.; Gengembre, L.; Chernavskii, P.; Gribovalconstant, A.; Khodakov, A. Effect of cobalt precursor and pretreatment conditions on the structure and catalytic performance of cobalt silica-supported Fischer Tropsch catalysts. *Journal of Catalysis* **2005**, *230*, 339–352.

(145) Tian, Y.; Hu, Z.; Yang, Y.; Wang, X.; Chen, X.; Xu, H.; Wu, Q.; Ji, W.; Chen, Y. In situ TA-MS study of the six-membered-ring-based growth of carbon nanotubes with benzene precursor. *Journal of the American Chemical Society* **2004**, *126*, 1180–11833.

(146) Yan, A.; Xiao, X.; Külaots, I.; Sheldon, B. W.; Hurt, R. H. Controlling water contact angle on carbon surfaces from 5° to 167°. *Carbon* **2006**, *44*, 3116–3120.

(147) Banerjee, D.; Mukherjee, S.; Chattopadhyay, K. K. Controlling the surface topology and hence the hydrophobicity of amorphous carbon thin films. *Carbon* **2010**, *48*, 1025–1031.

(148) Zhao, B.; Futaba, D. N.; Yasuda, S.; Akoshima, M.; Yamada, T.; Hata, K. Exploring advantages of diverse carbon nanotube forests with tailored structures synthesized by supergrowth from engineered catalysts. *ACS nano* **2009**, *3*, 108–114.

(149) Meng, L.-Y.; Park, S.-J. Effect of fluorination of carbon nanotubes on superhydrophobic properties of fluoro-based films. *Journal of colloid and interface science* **2010**, *342*, 559–563.

(150) Lau, K. K. S.; Bico, J.; Teo, K. B. K.; Chhowalla, M.; Amaratunga, G. a. J.; Milne, W. I.; McKinley, G. H.; Gleason, K. K. Superhydrophobic carbon nanotube forests. *Nano Letters* **2003**, *3*, 1701–1705.

(151) Ramos, S. C.; Vasconcelos, G.; Antunes, E. F.; Lobo, A. O.; Trava-Airoldi, V. J.; Corat, E. J. Total re-establishment of superhydrophobicity of vertically-aligned carbon nanotubes by CO2 laser treatment. *Surface and Coatings Technology* **2010**, *204*, 3073–3077.

(152) Georgakilas, V.; Bourlinos, A. B.; Zboril, R.; Trapalis, C. Synthesis , characterization and aspects of superhydrophobic functionalized carbon nanotubes. *Chemistry of Materials* **2008**, *20*, 2884–2886.

(153) Bu, I. Y. Y.; Oei, S. P. Hydrophobic vertically aligned carbon nanotubes on Corning glass for self cleaning applications. *Applied Surface Science* **2010**, *256*, 6699–6704.

(154) Nguyen-vu, T. D. B.; Chen, H.; Cassell, A. M.; Andrews, R. J.; Meyyappan, M. Vertically aligned carbon nanofiber architecture as a multifunctional 3-D neural electrical interface. *IEEE Transactions on Biomedical Engineering* **2007**, *54*, 1121–1128.

(155) Sethi, S.; Ge, L.; Ci, L.; Ajayan, P. M.; Dhinojwala, A. Gecko-inspired carbon nanotube-based self-cleaning adhesives. *Nano Letters* **2008**, *8*, 822–825.

(156) Puretzky, A. A.; Geohegan, D. B.; Jesse, S.; Ivanov, I. N.; Eres, G. In situ measurements and modeling of carbon nanotube array growth kinetics during chemical vapor deposition. *Applied Physics A* **2005**, *81*, 223–240.

(157) Louchev, O. A.; Laude, T.; Sato, Y.; Kanda, H. Diffusion-controlled kinetics of carbon nanotube forest growth by chemical vapor deposition. *Journal of Chemical Physics* **2003**, *118*, 7622–7634.

(158) Wang, X.; Feng, Y.; Unalan, H. E.; Zhong, G.; Li, P.; Yu, H.; Akinwande, A. I.; Milne, W. I. The mechanism of the sudden termination of carbon nanotube supergrowth. *Carbon* **2011**, *49*, 214–221.

(159) Einarsson, E.; Murakami, Y.; Kadowaki, M.; Maruyama, S. Growth dynamics of vertically aligned single-walled carbon nanotubes from in situ measurements. *Carbon* **2008**, *46*, 923–930.

(160) Vinten, P.; Lefebvre, J.; Finnie, P. Kinetic critical temperature and optimized chemical vapor deposition growth of carbon nanotubes. *Chemical Physics Letters* **2009**, *469*, 293–297.

(161) Wang, G.; Wang, H.; Tang, Z.; Li, W.; Bai, J. Simultaneous production of hydrogen and multi-walled carbon nanotubes by ethanol decomposition over Ni/Al2O3 catalysts. *Applied Catalysis B: Environmental* **2009**, *88*, 142–151.

(162) Shimoda, H.; Gao, B.; Tang, X.; Kleinhammes, A.; Fleming, L.; Wu, Y.; Zhou, O. Lithium intercalation into opened single-wall carbon nanotubes: storage capacity and electronic properties. *Physical Review Letters* **2001**, *88*, 5–8.

(163) Rana, K.; Sil, A.; Ray, S. Modification of the structure of multi-walled carbon nanotubes by choice of catalyst and their electrochemical behavior. *Materials Chemistry and Physics* **2010**, *120*, 484–489.

(164) Rana, K.; Sil, A.; Ray, S. Synthesis and characterization of carbon nanotubes by using catalyst LiNi0.5Co0.5O2 on anodized alumina substrate. *Advanced Materials Research* **2009**, *67*, 197–202.

(165) Rana, K.; Kucukayan-Dogu, G.; Sen, H. S.; Boothroyd, C.; Gulseren, O.; Bengu, E. Analysis of Charge Transfer for in Situ Li Intercalated Carbon Nanotubes. *The Journal of Physical Chemistry C* **2012**, *116*, 11364–11369.

(166) Lru, D.-R.; Williams, D. B. The electron-energy-loss spectrum of lithium metal. *Philosophical Magazine Part B* **1986**, *53*, L123–L128.

(167) Wang, F.; Graetz, J.; Moreno, M. S.; Ma, C.; Wu, L.; Volkov, V.; Zhu, Y. Chemical distribution and bonding of lithium in intercalated graphite: identification with optimized electron energy loss spectroscopy. *ACS Nano* **2011**, *5*, 1190–1197.

(168) Hightower, a.; Ahn, C. C.; Fultz, B.; Rez, P. Electron energy-loss spectrometry on lithiated graphite. *Applied Physics Letters* **2000**, *77*, 238–240.

(169) Liu, X.; Pichler, T.; Knupfer, M.; Fink, J. Electronic and optical properties of alkali-metal-intercalated single-wall carbon nanotubes. *Physical Review B* **2003**, *67*, 125403–125411.

(170) Cupolillo, A.; Giallombardo, C.; Papagno, L. Electronic properties of alkali–metal intercalated single walled carbon nanotubes. *Surface Science* **2007**, *601*, 2828–2831.

(171) Claye, a.; Nemes, N.; Jánossy, a.; Fischer, J. Structure and electronic properties of potassium-doped single-wall carbon nanotubes. *Physical Review B* **2000**, *62*, R4845–R4848.

(172) Bendiab, N.; Anglaret, E.; Bantignies, J.-L.; Zahab, a.; Sauvajol, J.; Petit, P.; Mathis, C.; Lefrant, S. Stoichiometry dependence of the Raman

spectrum of alkali-doped single-wall carbon nanotubes. *Physical Review B* **2001**, *64*, 1–6.

(173) Strydom, A.; Strydom, H. J. X-ray photoelectron spectroscopy studies of some cobalt (II) nitrate complexes. *Inorganic Chemistry Acta* **1989**, *159*, 191–195.

(174) Baer, Y.; Citrin, P. H.; Wertheim, G. K. X-Ray photoemission from lithium: An explanation of its X-ray edge. *Physical Review Letters* **1976**, *37*, 49–52.

(175) Imanishi, N.; Ohashi, S.; Ichikawa, T.; Takeda, Y.; Yamamoto, O. Carbon-lithium anodes for lithium secondary batteries. *Journal of Power Sources* **1992**, *39*, 185–191.

(176) Datsyuk, V.; Kalyva, M.; Papagelis, K.; Parthenios, J.; Tasis, D.; Siokou, a.; Kallitsis, I.; Galiotis, C. Chemical oxidation of multiwalled carbon nanotubes. *Carbon* **2008**, *46*, 833–840.

(177) Buqa, H.; Blyth, R. I. R.; Golob, P.; Evers, B.; Schneider, I.; Santis Alvarez, M. V.; Hofer, F.; Netzer, F. P.; Ramsey, M. G.; Winter, M.; Besenhard, J. O. Negative electrodes in rechargeable lithium ion batteries — Influence of graphite surface modification on the formation of the solid electrolyte interphase. *Ionics* **2000**, *6*, 172–179.

(178) Kanamura, K.; Shiraishi, S.; Takezawa, H.; Takehara, Z. XPS Analysis of the Surface of a Carbon Electrode Intercalated by Lithium Ions. **1997**, *4756*, 1797–1804.

(179) Momose, H.; Honbo, H.; Takeuchi, S.; Nishimura, K.; Horiba, T.; Muranaka, Y.; Kozono, Y.; Miyadera, H. X-ray photoelectron spectroscopy analyses of lithium intercalation and alloying reactions on graphite electrodes. *Journal of Power Sources* **1997**, *68*, 208–211.

(180) Mordkovich, V. Z. Synthesis and XPS investigation of superdense lithium-graphite intercalation compound, LiC2. *Synthetic Metals* **1996**, *80*, 243–247.

(181) Wertheim, G. K.; Van Attekum, P. M. T. M.; Basu, S. Electronic structure of lithium graphite. *Solid State Communications* **1980**, *33*, 1127–1130.

(182) da Silva Meirelles, L.; Caplan, A. I.; Nardi, N. B. In search of the in vivo identity of mesenchymal stem cells. *Stem cells* **2008**, *26*, 2287–2299.

(183) Nauta, A. J.; Fibbe, W. E. Immunomodulatory properties of mesenchymal stromal cells. *Blood* **2007**, *110*, 3499–3506.

(184) Tai, B. C. U.; Du, C.; Gao, S.; Wan, A. C. a; Ying, J. Y. The use of a polyelectrolyte fibrous scaffold to deliver differentiated hMSCs to the liver. *Biomaterials* **2010**, *31*, 48–57.

(185) Kang, Y.; Kim, S.; Khademhosseini, A.; Yang, Y. Creation of bony microenvironment with CaP and cell-derived ECM to enhance human bone-marrow MSC behavior and delivery of BMP-2. *Biomaterials* **2011**, *32*, 6119–6130.

(186) Yang, W.; Thordarson, P.; Gooding, J. J.; Ringer, S. P.; Braet, F. Carbon nanotubes for biological and biomedical applications. *Nanotechnology* **2007**, *18*, 412001.

(187) Saito, N.; Usui, Y.; Aoki, K.; Narita, N.; Shimizu, M.; Hara, K.; Ogiwara, N.; Nakamura, K.; Ishigaki, N.; Kato, H.; Taruta, S.; Endo, M. Carbon nanotubes: biomaterial applications. *Chemical Society reviews* **2009**, *38*, 1897–903.

(188) Chen, R. J.; Bangsaruntip, S.; Drouvalakis, K. a; Kam, N. W. S.; Shim, M.; Li, Y.; Kim, W.; Utz, P. J.; Dai, H. Noncovalent functionalization of carbon nanotubes for highly specific electronic biosensors. *Proceedings of the National Academy of Sciences of the United States of America* **2003**, *100*, 4984–9.

(189) Tay, C. Y.; Gu, H.; Leong, W. S.; Yu, H.; Li, H. Q.; Heng, B. C.; Tantang, H.; Loo, S. C. J.; Li, L. J.; Tan, L. P. Cellular behavior of human mesenchymal stem cells cultured on single-walled carbon nanotube film. *Carbon* **2010**, *48*, 1095–1104.

(190) Park, S. Y.; Namgung, S.; Kim, B.; Im, J.; Kim, J. Y.; Sun, K.; Lee, K. B.; Nam, J.-M.; Park, Y.; Hong, S. Carbon nanotube monolayer patterns for directed growth of mesenchymal stem cells. *Advanced Materials* **2007**, *19*, 2530–2534.

(191) Dalby, M.; Yarwood, S.; Riehle, M.; Johnstone, H.; Affrossman, S.; Curtis, A. Increasing fibroblast response to materials using nanotopography: morphological and genetic measurements of cell response to 13-nm-high polymer demixed islands. *Experimental Cell Research* **2002**, *276*, 1–9.

(192) Gentile, F.; Tirinato, L.; Battista, E.; Causa, F.; Liberale, C.; di Fabrizio, E. M.; Decuzzi, P. Cells preferentially grow on rough substrates. *Biomaterials* **2010**, *31*, 7205–7212.

(193) Kunzler, T. P.; Huwiler, C.; Drobek, T.; Vörös, J.; Spencer, N. D. Systematic study of osteoblast response to nanotopography by means of nanoparticle-density gradients. *Biomaterials* **2007**, *28*, 5000–5006.

(194) Bitirim, C. V.; Kucukayan-Dogu, G.; Bengu, E.; Akcali, K. C. Patterned carbon nanotubes as a new three-dimensional scaffold for mesenchymal stem cells. *Materials Science and Engineering C* **2012**, *submitted*.

(195) Dalby, M. J.; Gadegaard, N.; Tare, R.; Andar, A.; Riehle, M. O.; Herzyk, P.; Wilkinson, C. D. W.; Oreffo, R. O. C. The control of human

mesenchymal cell differentiation using nanoscale symmetry and disorder. *Nature materials* **2007**, *6*, 997–1003.

(196) Wirth, C. T.; Hofmann, S.; Robertson, J. Surface properties of vertically aligned carbon nanotube arrays. *Diamond and Related Materials* **2008**, *17*, 1518–1524.

(197) Cho, Y.; Borgens, R. B. The effect of an electrically conductive carbon nanotube/collagen composite on neurite outgrowth of PC12 cells. *Journal of biomedical materials research. Part A* **2010**, *95*, 510–517.

(198) Hirata, E.; Uo, M.; Takita, H.; Akasaka, T.; Watari, F.; Yokoyama, A. Development of a 3D collagen scaffold coated with multiwalled carbon nanotubes. *Journal of biomedical materials research. Part B, Applied biomaterials* **2009**, *90*, 629–634.

(199) Silva, E. E.; Colleta, H. H. M.; Ferlauto, A. S.; Moreira, R. L.; Resende, R. R.; Oliveira, S.; Kitten, G. T.; Lacerda, R. G.; Ladeira, L. O. Nanostructured 3-D collagen/nanotube biocomposites for future bone regeneration scaffolds. *Nano Research* **2010**, *2*, 462–473.

(200) MacDonald, R. a; Laurenzi, B. F.; Viswanathan, G.; Ajayan, P. M.; Stegemann, J. P. Collagen-carbon nanotube composite materials as scaffolds in tissue engineering. *Journal of biomedical materials research. Part A* **2005**, *74*, 489–496.

(201) Sridharan, I.; Kim, T.; Wang, R. Adapting collagen/CNT matrix in directing hESC differentiation. *Biochemical and biophysical research communications* **2009**, *381*, 508–512.

(202) Supronowicz, P. R.; Ajayan, P. M.; Ullmann, K. R.; Arulanandam, B. P.; Metzger, D. W.; Bizios, R. Novel current-conducting composite substrates for exposing osteoblasts to alternating current stimulation. *Journal of biomedical materials research* **2002**, *59*, 499–506.

(203) Gruber, H.; Somayaji, S.; Riley, F.; Hoelscher, G.; Norton, H.; Ingram, J.; Hanley, E. N. Human adipose-derived mesenchymal stem cells: serial passaging, doubling time and cell senescence. *Biotechnic and Histochemistyr* **2012**, *87*, 303–311.

(204) Crisostomo, P. R.; Wang, M.; Wairiuko, G. M.; Morrell, E. D.; Terrell, A. M.; Seshadri, P.; Nam, U. H.; Meldrum, D. R. High passage number of stem cells adversely affects stem cell activation and myocardial protection. *Shock* **2006**, *26*, 575–580.

(205) Smart, S. K.; Cassady, a. I.; Lu, G. Q.; Martin, D. J. The biocompatibility of carbon nanotubes. *Carbon* **2006**, *44*, 1034–1047.

(206) Jia, G.; Wang, H.; Yan, L.; Wang, X.; Pei, R.; Yan, T.; Zhao, Y.; Guo, X. Cytotoxicity of carbon nanomaterials: single-wall nanotube, multi-wall nanotube, and fullerene. *Environmental science & technology* **2005**, *39*, 1378–1383.

(207) Liu, D.; Yi, C.; Zhang, D.; Zhang, J.; Yang, M. Inhibition of proliferation and differentiation of mesenchymal stem cells by carboxylated carbon nanotubes. *ACS Nano* **2010**, *4*, 2185–2195.

(208) Blochl, P. E. Projector augmented-wave method. *Physical Review B* **1994**, *50*, 17953–17979.

List of Publications

1. Rana, K.; Kucukayan-Dogu, G.; Sen S. H.; Boothroyd C.; Gulseren O.; Bengu E. Analysis of charge transfer for in Situ Li intercalated carbon nanotubes. *The Journal of Physical Chemistry C* **2012** *116*, 11364−11369.
2. Sam, E. D.; Kucukayan-Dogu, G.; Baykal, B.; Dalkilic Z.; Rana K.; Bengu E. Simultaneous growth of self-patterned carbon nanotube forests with dual height scales. *Nanoscale* **2012** *4*, 3746 – 3753.
3. Rana, K.; Kucukayan-Dogu, G.; Bengu, E. Growth of vertically aligned carbon nanotubes over self-ordered nano-porous alumina films and their surface properties. *Applied Surface Science* **2012** *258*, 7112-7117.
4. Bitirim, V. C.; Kucukayan-Dogu, G.; Bengu, E.; Akcali, K. C. Patterned carbon nanotubes as a new three-dimensional scaffold for mesenchymal stem cells. *submitted to Materials Science and Engineering C* **2012**.
5. Kucukayan, G.; Ovalı, R.; Ilday, S.; Baykal, B.; Yurdakul, H.; Turan, S.; Gülseren, O.; Bengu, E. An experimental and theoretical study of the sulfur effect on the pyrolytically grown carbon nanotubes using sucrose based solid state precursors. *Carbon* **2011** *49*, 508 – 517.
6. Kucukayan-Dogu, G.; Bitirim, V. C.; Gozen, D.; Bengu, E.; Akcali, K. C. Preferential attachment of metastatic cancer cells to patterned carbon nanotubes. *In prepration*.

7. Kucukayan-Dogu, G.; Sen, H. S.; Yurdakul, H.; Turan, S.; Gulseren, O.; Bengu, E. The doping of phosphorous on the pyrolytically grown carbon nanotubes using sucrose based solid state precursors. *In prepration*.

Proceedings

1. Kucukayan, G.; Kayacan, S.; Baykal, B.; Bengu, E. Use of saccharides as solid-state precursors for the synthesis of carbon nanotubes. *MRS Proceedings* **2008** *1081*, P05-14.

Copyright Licences

NATURE PUBLISHING GROUP LICENSE
TERMS AND CONDITIONS

This is a License Agreement between Gokce Dogu ("You") and Nature Publishing Group ("Nature Publishing Group") provided by Copyright Clearance Center ("CCC"). The license consists of your order details, the terms and conditions provided by Nature Publishing Group, and the payment terms and conditions.

All payments must be made in full to CCC. For payment instructions, please see information listed at the bottom of this form.

License Number	3065211121554
License date	Jan 10, 2013
Licensed content publisher	Nature Publishing Group
Licensed content publication	Nature
Licensed content title	Helical microtubules of graphitic carbon
Licensed content author	Sumio Iijima
Licensed content date	Nov 7, 1991
Volume number	354
Issue number	6348
Type of Use	reuse in a thesis/dissertation
Requestor type	academic/educational
Format	print and electronic
Portion	figures/tables/illustrations
Number of figures/tables/illustrations	1
Figures	1
Author of this NPG article	no
Your reference number	
Title of your thesis / dissertation	Synthesis, Characterization and Functionalization of Vertically Aligned Carbon Nanotube Arrays
Expected completion date	Jan 2013
Estimated size (number of pages)	200
Total	0.00 USD

ELSEVIER LICENSE
TERMS AND CONDITIONS

This is a License Agreement between Gokce Dogu ("You") and Elsevier ("Elsevier") provided by Copyright Clearance Center ("CCC"). The license consists of your order details, the terms and conditions provided by Elsevier, and the payment terms and conditions.

All payments must be made in full to CCC. For payment instructions, please see information listed at the bottom of this form.

Supplier	Elsevier Limited The Boulevard,Langford Lane Kidlington,Oxford,OX5 1GB,UK
Registered Company Number	1982084
Customer name	Gokce Dogu
Customer address	Bilkent University Ankara , 06800
License number	3065391036099
License date	Jan 10, 2013
Licensed content publisher	Elsevier
Licensed content publication	Journal of Crystal Growth
Licensed content title	Why are carbon filaments tubular?
Licensed content author	Gary G. Tibbetts
Licensed content date	May 1984
Licensed content volume number	66
Licensed content issue number	3
Number of pages	7
Start Page	632
End Page	638
Type of Use	reuse in a thesis/dissertation
Portion	figures/tables/illustrations
Number of figures/tables/illustrations	1
Format	both print and electronic
Are you the author of this Elsevier article?	No
Will you be translating?	No
Order reference number	

Title of your thesis/dissertation	Synthesis, Characterization and Functionalization of Vertically Aligned Carbon Nanotube Arrays
Expected completion date	Jan 2013
Estimated size (number of pages)	200
Elsevier VAT number	GB 494 6272 12
Permissions price	0.00 USD
VAT/Local Sales Tax	0.0 USD / 0.0 GBP
Total	0.00 USD

NATURE PUBLISHING GROUP LICENSE
TERMS AND CONDITIONS

This is a License Agreement between Gokce Dogu ("You") and Nature Publishing Group ("Nature Publishing Group") provided by Copyright Clearance Center ("CCC"). The license consists of your order details, the terms and conditions provided by Nature Publishing Group, and the payment terms and conditions.

All payments must be made in full to CCC. For payment instructions, please see information listed at the bottom of this form.

License Number	3065850543447
License date	Jan 11, 2013
Licensed content publisher	Nature Publishing Group
Licensed content publication	Nature
Licensed content title	Large-scale synthesis of carbon nanotubes
Licensed content author	T. W. Ebbesen, P. M. Ajayan
Licensed content date	Jul 16, 1992
Volume number	358
Issue number	6383
Type of Use	reuse in a thesis/dissertation
Requestor type	academic/educational
Format	print and electronic
Portion	figures/tables/illustrations
Number of figures/tables/illustrations	3
Figures	3
Author of this NPG article	no
Your reference number	
Title of your thesis / dissertation	Synthesis, Characterization and Functionalization of Vertically Aligned Carbon Nanotube Arrays
Expected completion date	Jan 2013
Estimated size (number of pages)	200
Total	0.00 USD

NATURE PUBLISHING GROUP LICENSE
TERMS AND CONDITIONS

This is a License Agreement between Gokce Dogu ("You") and Nature Publishing Group ("Nature Publishing Group") provided by Copyright Clearance Center ("CCC"). The license consists of your order details, the terms and conditions provided by Nature Publishing Group, and the payment terms and conditions.

All payments must be made in full to CCC. For payment instructions, please see information listed at the bottom of this form.

License Number	3065860004055
License date	Jan 11, 2013
Licensed content publisher	Nature Publishing Group
Licensed content publication	Nature
Licensed content title	Atomic structure and electronic properties of single-walled carbon nanotubes
Licensed content author	Teri Wang Odom, Jin-Lin Huang, Philip Kim, Charles M. Lieber
Licensed content date	Jan 1, 1998
Volume number	391
Issue number	6662
Type of Use	reuse in a thesis/dissertation
Requestor type	academic/educational
Format	print and electronic
Portion	figures/tables/illustrations
Number of figures/tables/illustrations	1
Figures	2
Author of this NPG article	no
Your reference number	
Title of your thesis / dissertation	Synthesis, Characterization and Functionalization of Vertically Aligned Carbon Nanotube Arrays
Expected completion date	Jan 2013
Estimated size (number of pages)	200
Total	0.00 USD

THE AMERICAN ASSOCIATION FOR THE ADVANCEMENT OF SCIENCE LICENSE
TERMS AND CONDITIONS

This is a License Agreement between Gokce Dogu ("You") and The American Association for the Advancement of Science ("The American Association for the Advancement of Science") provided by Copyright Clearance Center ("CCC"). The license consists of your order details, the terms and conditions provided by The American Association for the Advancement of Science, and the payment terms and conditions.

All payments must be made in full to CCC. For payment instructions, please see information listed at the bottom of this form.

License Number	3065401123468
License date	Jan 10, 2013
Licensed content publisher	The American Association for the Advancement of Science
Licensed content publication	Science
Licensed content title	Water-Assisted Highly Efficient Synthesis of Impurity-Free Single-Walled Carbon Nanotubes
Licensed content author	Kenji Hata, Don N. Futaba, Kohei Mizuno, Tatsunori Namai, Motoo Yumura, Sumio Iijima
Licensed content date	Nov 19, 2004
Volume number	306
Issue number	5700
Type of Use	Thesis / Dissertation
Requestor type	Scientist/individual at a research institution
Format	Print and electronic
Portion	Figure
Number of figures/tables	1
Order reference number	
Title of your thesis / dissertation	Synthesis, Characterization and Functionalization of Vertically Aligned Carbon Nanotube Arrays
Expected completion date	Jan 2013
Estimated size(pages)	200
Total	0.00 USD

ELSEVIER LICENSE
TERMS AND CONDITIONS

This is a License Agreement between Gokce Dogu ("You") and Elsevier ("Elsevier") provided by Copyright Clearance Center ("CCC"). The license consists of your order details, the terms and conditions provided by Elsevier, and the payment terms and conditions.

All payments must be made in full to CCC. For payment instructions, please see information listed at the bottom of this form.

Supplier	Elsevier Limited The Boulevard,Langford Lane Kidlington,Oxford,OX5 1GB,UK
Registered Company Number	1982084
Customer name	Gokce Dogu
Customer address	Bilkent University Ankara , 06800
License number	3065391432974
License date	Jan 10, 2013
Licensed content publisher	Elsevier
Licensed content publication	Materials Science and Engineering: R: Reports
Licensed content title	Diamond-like amorphous carbon
Licensed content author	J. Robertson
Licensed content date	24 May 2002
Licensed content volume number	37
Licensed content issue number	4–6
Number of pages	153
Start Page	129
End Page	281
Type of Use	reuse in a thesis/dissertation
Intended publisher of new work	other
Portion	figures/tables/illustrations
Number of figures/tables/illustrations	1
Format	both print and electronic
Are you the author of this Elsevier article?	No
Will you be translating?	No

Order reference number	
Title of your thesis/dissertation	Synthesis, Characterization and Functionalization of Vertically Aligned Carbon Nanotube Arrays
Expected completion date	Jan 2013
Estimated size (number of pages)	200
Elsevier VAT number	GB 494 6272 12
Permissions price	0.00 USD
VAT/Local Sales Tax	0.0 USD / 0.0 GBP
Total	0.00 USD

THE AMERICAN ASSOCIATION FOR THE ADVANCEMENT OF SCIENCE LICENSE
TERMS AND CONDITIONS

This is a License Agreement between Gokce Dogu ("You") and The American Association for the Advancement of Science ("The American Association for the Advancement of Science") provided by Copyright Clearance Center ("CCC"). The license consists of your order details, the terms and conditions provided by The American Association for the Advancement of Science, and the payment terms and conditions.

All payments must be made in full to CCC. For payment instructions, please see information listed at the bottom of this form.

License Number	3065401303203
License date	Jan 10, 2013
Licensed content publisher	The American Association for the Advancement of Science
Licensed content publication	Science
Licensed content title	Large-Scale Synthesis of Aligned Carbon Nanotubes
Licensed content author	W. Z. Li, S. S. Xie, L. X. Qian, B. H. Chang, B. S. Zou, W. Y. Zhou, R. A. Zhao, G. Wang
Licensed content date	Dec 6, 1996
Volume number	274
Issue number	5293
Type of Use	Thesis / Dissertation
Requestor type	Scientist/individual at a research institution
Format	Print and electronic
Portion	Figure
Number of figures/tables	1
Order reference number	
Title of your thesis / dissertation	Synthesis, Characterization and Functionalization of Vertically Aligned Carbon Nanotube Arrays
Expected completion date	Jan 2013
Estimated size(pages)	200
Total	0.0 USD

ELSEVIER LICENSE
TERMS AND CONDITIONS

This is a License Agreement between Gokce Dogu ("You") and Elsevier ("Elsevier") provided by Copyright Clearance Center ("CCC"). The license consists of your order details, the terms and conditions provided by Elsevier, and the payment terms and conditions.

All payments must be made in full to CCC. For payment instructions, please see information listed at the bottom of this form.

Supplier	Elsevier Limited The Boulevard,Langford Lane Kidlington,Oxford,OX5 1GB,UK
Registered Company Number	1982084
Customer name	Gokce Dogu
Customer address	Bilkent University
	Ankara , 06800
License number	3065400256610
License date	Jan 10, 2013
Licensed content publisher	Elsevier
Licensed content publication	Current Applied Physics
Licensed content title	Effect of thin aluminum interlayer on growth and microstructure of carbon nanotubes
Licensed content author	A. Mathur,S.S. Roy,C. Dickinson,J.A. McLaughlin
Licensed content date	March 2010
Licensed content volume number	10
Licensed content issue number	2
Number of pages	4
Start Page	407
End Page	410
Type of Use	reuse in a thesis/dissertation
Portion	figures/tables/illustrations
Number of figures/tables/illustrations	1
Format	both print and electronic
Are you the author of this Elsevier article?	No

Will you be translating?	No
Order reference number	
Title of your thesis/dissertation	Synthesis, Characterization and Functionalization of Vertically Aligned Carbon Nanotube Arrays
Expected completion date	Jan 2013
Estimated size (number of pages)	200
Elsevier VAT number	GB 494 6272 12
Permissions price	0.00 USD
VAT/Local Sales Tax	0.0 USD / 0.0 GBP
Total	0.00 USD

ELSEVIER LICENSE
TERMS AND CONDITIONS

This is a License Agreement between Gokce Dogu ("You") and Elsevier ("Elsevier") provided by Copyright Clearance Center ("CCC"). The license consists of your order details, the terms and conditions provided by Elsevier, and the payment terms and conditions.

All payments must be made in full to CCC. For payment instructions, please see information listed at the bottom of this form.

Supplier	Elsevier Limited The Boulevard,Langford Lane Kidlington,Oxford,OX5 1GB,UK
Registered Company Number	1982084
Customer name	Gokce Dogu
Customer address	Bilkent University
	Ankara , 06800
License number	3065400582013
License date	Jan 10, 2013
Licensed content publisher	Elsevier
Licensed content publication	Carbon
Licensed content title	Strong influence of buffer layer type on carbon nanotube characteristics
Licensed content author	Teresa de los Arcos,M Gunnar Garnier,Peter Oelhafen,Daniel Mathys,Jin Won Seo,Concepción Domingo,José Vicente García-Ramos,Santiago Sánchez-Cortés
Licensed content date	2004
Licensed content volume number	42
Licensed content issue number	1
Number of pages	4
Start Page	187
End Page	190
Type of Use	reuse in a thesis/dissertation

Intended publisher of new work	other
Portion	figures/tables/illustrations
Number of figures/tables/illustrations	1
Format	both print and electronic
Are you the author of this Elsevier article?	No
Will you be translating?	No
Order reference number	
Title of your thesis/dissertation	Synthesis, Characterization and Functionalization of Vertically Aligned Carbon Nanotube Arrays
Expected completion date	Jan 2013
Estimated size (number of pages)	200
Elsevier VAT number	GB 494 6272 12
Permissions price	0.00 USD
VAT/Local Sales Tax	0.0 USD / 0.0 GBP
Total	0.00 USD